



**University of
Nottingham**
UK | CHINA | MALAYSIA

First-principles, tight-binding and atomic spin model study of two- dimensional magnets

Qirui Cui, BSc

Thesis submitted to the University of Nottingham
for the degree of Doctor of Philosophy

June, 2022

Abstract

The key ingredient for making better electronic devices is using materials with highly corresponding functional properties. The discovery of long-range magnetic order in two-dimensional (2D) van der Waals (vdW) materials paves a new avenue for spintronics research since these 2D magnets combines miniaturization (several angstrom), gate tunability, flexibility, high interface quality etc, and these advantages can be further inherited by electronics devices harnessing 2D magnets. However, there are some crucial problems still unsolved, which largely impedes practical applications of 2D magnets. For examples, most 2D magnets lack large perpendicular magnetic anisotropy (PMA) and high critical temperature. And inversion symmetry in 2D magnets could prohibits the emergence of topological magnetism. In this thesis, the first-principles calculations, tight-binding model and atomic spin model simulations are conducted to investigate the basic magnetic parameters, non-trivial transport phenomena of electrons and topological spin configurations in 2D magnets and their corresponding heterostructures (HSs), where spin-orbit coupling (SOC) plays crucial roles. The tight-binding model can give an accurate description of low-energy bands, thus helping us figure out crucial physical terms in materials; and the atomic spin model simulations can describe spin interaction in atomic level, thus helping us elucidate the spin configurations in 2D materials.

We first show that the PMA of NiI₂ monolayer increases significantly when vdW interlayer distance of graphene/NiI₂ (Gr/NiI₂) HS decreases. This enhancement arises from the electronic states change of *5p* orbitals of interfacial iodine. At the same time, the quantum anomalous Hall effect (QAHE) is realized in graphene layer. We second show that VSi₂N₄ is a ferromagnetic semiconductor harboring valley-contrasting physics. By tuning magnetization orientation from in-plane to out-of-plane, the valley polarization can be generated, resulting in the anomalous valley Hall effect (AVHE) in VSi₂N₄. We establish the mathematical relationship between valley splitting and magnetization orientation based on the model analysis. Moreover, via constructing Janus structures to break inversion symmetry, we achieve significant isotropic

Dzyaloshinskii–Moriya interaction (DMI) and topological spin textures with ultra-small size in 2D magnets including CrXTe ($X = \text{S}, \text{Se}$), MnBi₂Se₂Te₂ (MBST) and MBST/In₂Se₃ HS. Importantly, we demonstrate that strain and ferroelectric polarization are powerful tools for manipulating topological spin textures. The observed topological spin textures in 2D magnets have ultra-small size, high tunability and various morphology, which is hopefully considered as the ideal information carrier in electronic devices. We also find that critical temperature of strained CrXTe monolayer is even above the room temperature. This is a key factor required in realistic devices. Finally, we propose and demonstrate that a novel family of 2D magnets with $P\bar{4}m2$ crystal symmetry hold anisotropic DMI. This crystal symmetry-protected anisotropic DMI leads to various intriguing topological magnetism, including ferromagnetic chiral domain wall/antiskyrmion and antiferromagnetic chiral domain wall/antiskyrmion/vortex-antivortex pair in this family. These findings highlight potential applications of 2D magnets on the next-generation spintronic devices with high storage density, high speed and low energy consumption.

Acknowledgement

First and foremost, I want to thank my PhD advisor from CNIETCH, Prof. Hongxin Yang, for supporting me through the past three-year journey of scientific research. He not only guides me to learn lots of knowledge about physics but also teaches me to analyze specific physical problems from the high level and understand them detailly. When discussing with him about projects, I always feel his solid background on condensed matter physics and first-principles calculations. Yang is also a very humorous person, and our discussion is often full of laugh. I feel fortunate to have Yang as my PhD advisor, and without him, all works in this thesis would not be existed. I will forever be thankful for him.

I would like to thank another PhD advisor, Prof. Ping Cui. She gives me the chance to pursue PhD degree under joint cultivation of UNNC and CNITECH. Despite she has lots of administrative affairs, she always spares time to care about my life in Ningbo and gives me many encouragements and supports in scientific research. Her strong will, optimistic attitude for life and enthusiasm for work inspire me to try best to solve various problems and keep motion on everything. I feel very lucky to have a such great PhD advisor.

I would like to thank my friends that are bonded together because of physics. Dr. Baishun Yang teaches me lots of techniques on first-principles calculations. Dr. Jinghua Liang gives me many extremely useful lessons on tight-binding model and micromagnetic simulations. Without their selfless help, it will take several months and even longer before these papers are published. Special thanks to Miss Yingmei Zhu for her warm company in my life. I also want to thank my officemates: Dr. Tao Xu, Dr. Ziji Shao, Dr. Wei Liu, Liming Wang, Zhiwen Wang, Peng Li, Jiawei Jiang, Yaqin Guo, Wenhao Di and Xiufu Yang for their interesting and informative discussions.

Finally, I would like to thank my parents for their unconditional love and lighting up my life.

Contents

Abstract	i
Acknowledgement	iii
Chapter 1 General Overview	1
1.1 Background	1
1.1.1 Spintronics.....	1
1.1.2 Two-dimensional vdW Materials	5
1.2 Aim and objectives	8
1.3 Thesis structure	9
Chapter 2 Literature Review	11
2.1 Magnetic anisotropy of 2D magnets	11
2.2 Valley characters of 2D materials.....	13
2.3 Magnetic skyrmion.....	15
2.4 Density Functional Theory	17
2.5 Tight-binding and atomic spin model	21
2.6 Summary	23
Chapter 3 Proximity Effects in Gr/NiI₂ Heterostructure	25
3.1 Introduction	25
3.2 Methodology	26
3.3 Results and Discussion.....	27
3.3.1 Pristine NiI ₂ and Gr/NiI ₂ heterostructure	27
3.3.2 Interlayer spacing controlled magnetic anisotropy	30
3.3.3 QAHE in Gr/NiI ₂ heterostructure.....	34
3.4 Summary	38
Chapter 4 Spin-valley coupling in VSi₂N₄ monolayer	39
4.1 Introduction	39
4.2 Methodology	40
4.3 Results and discussion.....	41
4.3.1 Structural and magnetic properties of VSi ₂ N ₄	41

4.3.2 Spin-valley coupling	43
4.3.3 Strain-tunable valley properties	49
4.4 Summary	52
Chapter 5 Strain-tunable chiral magnetism in 2D Janus magnets.....	53
5.1 Introduction	53
5.2 Methodology	54
5.3 Results and discussion.....	57
5.3.1 Pristine CrXTe (X=S, Se) monolayer	57
5.3.2 Strain tunable magnetic parameters	58
5.3.3 Strain-tunable topological spin textures and Curie temperature	64
5.4 Summary	68
Chapter 6 Ferroelectrically controlled topological magnetism in Janus-magnet-	
based multiferroic heterostructure	69
6.1 Introduction	69
6.2 Methodology	70
6.3 Results and discussion.....	78
6.3.1 The crystal structure of MBST/In ₂ Se ₃ heterostructure.....	78
6.3.2 Ferroelectric polarization controlled magnetic parameters	80
6.3.3 Ferroelectric polarization controlled topological magnetism	82
6.3.4 The mechanism of magnetic anisotropy variation	85
6.3.5 Electronic band structures	87
6.4 Summary	88
Chapter 7 Anisotropic Dzyaloshinskii-Moriya interaction and anti-topological	
magnetism in two-dimensional magnets	89
7.1 Introduction	89
7.2 Methodology	90
7.3 Results and discussion.....	91
7.3.1 Anisotropic DMI and exchange coupling	91
7.3.2 Topological spin configurations	98

Chapter 8 Summary	104
8.1 Summary	104
8.2 Future works.....	106
Reference	108
Publication List	126

Chapter 1 General Overview

1.1 Background

1.1.1 Spintronics

Spin is the intrinsic angular momentum of elementary particles, and in the case of electron, the spin quantum number equals $+\frac{1}{2}$ or $-\frac{1}{2}$, which corresponds for spin-up and spin-down states. In 1988, the groups of A. Fert and P. Grünberg observe the significant variation of resistance in magnetic multilayers when the spin orientations of adjacent ferromagnetic (FM) layers separated by non-magnetic conductive layers are aligned by external magnetic field [1, 2]. This phenomenon is called as the giant magnetoresistance (GMR) effect, which opens a novel avenue for investigating magnetic properties of materials by spin-dependent transport and generates a novel research field named as spintronics. Following the GMR, tunneling magnetoresistance (TMR) is developed, where the spacer between adjacent FM layers is chosen to be insulator. The magnetoresistance is manipulated by tilting the spin orientation of FM layer in magnetic tunneling junction (MTJ). One mile stone in TMR development is the discovery of huge TMR ratio, which could reach to 600% at room temperature, in Fe/MgO/Fe based MTJ [3-8]. It is believed that significant TMR in MgO-based systems arises from the unique band structures which has spin-filtering effect [9, 10]. Initially, GMR and TMR have been used as sensing elements in the read heads of hard disk drives, which dramatically enhance the storage density. TMR then is applied in the magnetic random-access memory (MARM), where the MTJ is chosen as storage elements [11]. This TMR-based MARM is using magnetic field generated by “word” and “bit” lines to write information, which has high energy consumption. For overcoming this problem, spin-transfer torque (STT) is introduced into MARM. Instead of applying an external field, STT refers to manipulating magnetic moment by using the spin-polarized current to transfer spin angular momentum [12, 13]. Compared with charge-based memories such as static random-

access memory (SRAM) and dynamic random-access memory (DRAM), STT-MARM is a non-volatile memory and has much lower energy consumption. For guaranteeing the high stability and thin thickness of STT-MARM, it is normally required that the reference layer processes strong PMA and small intrinsic size.

A few years later than the first-demonstration of STT-MARM in 2000, the SOC effect, a relativistic interaction where the intrinsic spin moment of electron is coupled with atomic orbital moment, has been shown possibility to create spin-polarized current or pure spin current in non-magnetic materials, which avoids demagnetization effect in FM materials [14]. Notably, SOC effect gives rise to many non-trivial effects with potential for information processing and handling, and applications of SOC on spintronics lead to the spin-orbitronics [15, 16]. One interesting topic in this field is spin Hall effect (SHE). In SHE, a transverse pure spin current can be generated by an electrical current passing through a material. There is an accumulation of spins with opposite signs on the lateral boundaries of the sample, which is first time observed in GaAs by magneto-optical Kerr microscope in 2004 [17]. In inversion spin Hall effect (ISHE), a pure electrical current is generated when a pure spin current passes through materials. The SHE and ISHE are characterized by the spin Hall angle θ which is defined as the ratio of spin current density and charge current density. The larger magnitude of θ indicates the higher efficiency of spin-charge conversion. Strong SHE effects are achieved in compounds containing heavy elements with strong SOC, and the most used systems in spintronics are heavy metals such as paramagnetic Ta, Pt and W [18-22]. In these pure metals, the SHE dominantly arises from intrinsic mechanism where spin-orbit-coupled electronic band structures (momentum-space Berry phase) plays deterministic roles [23].

After 2005, the quantum spin Hall effect (QSHE) arises extensive interests. Kane and Mele first illustrate that symmetry allowed spin orbit potential could converts graphene from a 2D semimetal to QSH insulator when Fermi level coordinates in energy gap [24]. The electrons with opposite spin signs only transport along the boundaries of sample with opposite directions. However, the intrinsic SOC

strength of graphene is very tiny ($\sim\mu\text{eV}$), which largely impedes the experimental observation of QSHE in graphene. In 2006, Bernevig et al show that the general mechanism for QSHE is band inversion [25]. They propose that in CdTe-HgTe-CdTe quantum well, strong SOC-induced s - p band inversion in HgTe gives rise the quantized spin Hall conductance when thickness of HgTe is over the critical thickness. In 2007, the experimental group from Germany demonstrates this proposal. König et al find that when the thickness of HgTe is over 6.3 nm and temperature is lower than 10K, the nominally insulating regime of CdTe-HgTe-CdTe quantum well shows a plateau of residual conductance close to $2e^2/h$ [26]. These discoveries also lead to an important concept in condensed matter physics, topological insulator (TI), which has the insulating bulk state but conducting and quantized edge state [27]. The concept of TI can be generalized to three dimensions, which is a bulk insulator with metallic surface state protected by the time reversal symmetry (TRS). The thermoelectric materials $\text{Bi}_{1-x}\text{Sb}_x$ alloys and Bi_2Se_3 , Bi_2Te_3 and Sb_2Te_3 family compounds, that all possess strong SOC, are theoretically proposed and experimentally confirmed to be 3D TIs [28]. Moreover, by introducing long-range magnetic order to break TRS, the QSH system could be further converted to quantum anomalous Hall (QAH) system, where dissipation-less and single spin-polarized edge states are realized without the external magnetic field. This phenomenon is theoretically investigated and first experimentally demonstrated in thin films of Cr-doped $(\text{Bi,Sb})_2\text{Te}_3$ [29, 30]. For edge/surface states of quantum Hall systems, the electrons move with the extremely low energy consumption and electrical resistance since there is no back scattering from impurities, which makes TIs hold great potential for spintronic applications [31-33].

We now focus on another interesting topic in spin-orbitronics, Dzyaloshinskii–Moriya interaction (DMI), which is recognized as a crucial parameter in the generation, stabilization and manipulation of magnetic skyrmions and chiral domain walls in the system lacking of inversion symmetry. Skyrmions are ideal information carriers for next-generation memory or logic technologies, such as racetrack memory,

reconfigurable logic gates, artificial neuron devices, and quantum bit for quantum computing with ultra-high density and low-energy consumption, thanks to their stable configuration with unique helicity, tunable nano-scale size, and low drive current density [34-39]. The study of DMI originates from the investigation of weak ferromagnetism in some antiferromagnetic (AFM) materials in the 1960s. It is noted that some AFM materials, such as α -Fe₂O₃ and carbonates MnCO₃ and CoCO₃, exhibit spontaneous magnetization behavior [40, 41]. However, their spontaneous magnetic moments are much smaller compared with the magnetic atoms. Some explanations suggest that the system magnetism is extrinsic which is caused by impurities or AFM domains, but theoretical analysis showed that both of them are not conducive to reducing the system's free energy. In 1958, Dzyaloshinskii first give the correct theoretical explanation for this phenomenon [42, 43]. He proposes that the key reason for the existence of weak ferromagnetism in these AFM crystals is that they have the following antisymmetric terms in free energy expressions: $E_{DM} = \mathbf{D}_{ij} \cdot (\mathbf{S}_i \times \mathbf{S}_j)$. Here, \mathbf{D}_{ij} is the interaction vector and \mathbf{S}_i (\mathbf{S}_j) is the spin vector at position i (j). This item is later called as DMI. According to the above formula, one can find that DMI tends to align the adjacent spins perpendicular to each other unlike the Heisenberg exchange interactions ($E_{ex} = -J\mathbf{S}_i \cdot \mathbf{S}_j$) that make the spins parallel or anti-parallel. The competition between these two interactions eventually causes the magnetic moments of AFM materials such as α -Fe₂O₃ generating a small inclination angle from the collinear alignment direction, thereby inducing the weak ferromagnetism in these AFM materials. In 1960, by extending the theory of Anderson super-exchange interaction, Moriya proves that DMI is generated by the cooperation between the inter-spin superexchange and the SOC in the magnetic insulator without inversion symmetry [44, 45]. Moreover, Moriya gives specific relationships between crystal symmetry and DM vectors. In 1980, Fert and Levy propose that DMI between Mn atoms in *CuMn* spin-glass alloy could arise from the spin-orbit scattering of conduction electrons by non-magnetic impurities [46]. By first-principles calculations and experiments, the Fert-Levy DMI is further confirmed

at the FM metal/heavy metal interface, where large DMI is dominantly contributed by strong SOC of heavy metal, such as Pt and Ir [47]. In 2018, Yang et al further theoretically propose and experimentally demonstrate that Rashba-type DMI are achieved in Co/Graphene heterostructure, hence avoiding the applications of heavy metal and paving the way for two-dimensional-materials based spin-orbitronics [48].

1.1.2 Two-dimensional vdW Materials

The tremendous studies on 2D crystals starts from the initial discovery of graphene. In 2004, A. Geim and K. Novoselov extract graphene from the bulk graphite using scotch technique [49]. The graphene processes many appealing physical and chemical properties. For example, graphene has record thermal conductivity, flexibility and gas impermeability [50-54], and the charge carriers in graphene has extremely high intrinsic mobility and zero effective mass [55, 56]. Importantly, the electrons can be described by Dirac-like equations, and there are emerging two decoupled Dirac cones at K and K' Brillouin zone, hence making graphene a platform for theoretical investigation and experimental observation of various quantum relativistic phenomena. For example, in 2005, Zhang et al first realize the half-integer quantum Hall effect in graphene [57], and Kane and mele propose that QSHE can be achieved [24]; in 2010, Qiao et al further show that by introducing Rashba SOC and exchange field, QAHE can be realized in graphene [58]. However, the graphene is not the best 2D materials for every application, for example, the zero bandgap of graphene renders it useless in semiconductor.

The transition metal dichalcogenides (TMDCs) is a large family of layered materials with the formula MX_2 . Chalcogen atom X includes S, Se and Te, and transition metal M contains almost all metal elements ranging from IVB to VIII. By combining different elements to construct TMDC, various electronic states, including metal, semiconductor and insulator, all can be achieved, and by tuning the number of stacked TMDC semiconductor layers, the size of bandgap can be significantly manipulated which is accompanied with transition from direct to indirect bandgap

[59-63]. Moreover, TMDC semiconductors possess intrinsic miniaturization, relatively high carrier mobility and air stability, which makes field-effect transistors process sub-10-nm gate length and meanwhile maintain small subthreshold swing and low leakage current [64]. One interesting topic of TMDC semiconductors is valleytronics. The Valley that means the local maximum of valence bands or minimum of conduction bands is another freedom of electrons besides spin and charge. The attempts of using valley freedom to encode, transform and handle information, which is similar to electronic or spintronic applications, leads to the concept valleytronics [65-70]. In 2007, Xiao et al first illustrate that valley-dependent Berry phase can result in electrons from different valley achieve opposite velocity transverse to in-plane electric field, which is called as valley Hall effect [65]. Contrary to graphene, MoS₂ and other group-VI dichalcogenides with explicit inversion symmetry and strong SOC arising from *d* orbitals provide a better platform for investigating coupled spin and valley physics. In 2012, Xiao et al propose that in this system, valley and spin Hall effect can be achieved, and the carriers from different valley can be selectively excited by optical field with opposite circular polarization [67]. These phenomena are further confirmed by Mak et al and Zeng et al in experiments [71-73].

In 1966, via applying Bogoliubov's inequality, Mermin and Wanger demonstrate that long-range FM order can't survive in isotropic 2D systems due to thermal fluctuation [74]. The exciting breakthrough happens in 2017 that Zhang et al and Xu et al experimentally observe the long-range ferromagnetism exists in CrI₃ monolayer and CrGeTe₃ bilayer respectively [75, 76]. They probe the long-range magnetism using magneto-optic Kerr microscopy and determine the Curie temperature T_c of CrI₃ monolayer and CrGeTe₃ bilayers reaching to 45 and 30K respectively. It is believed that magnetic anisotropy results in gapped magnon dispersions which allows the existence of long-range FM order at finite temperature. After that, more and more 2D magnets with relatively high T_c , such as MnSe₂ ($T_c \sim 300\text{K}$), VSe₂ ($T_c \sim 330\text{K}$) and Fe₃GeTe₂ ($T_c \sim 120\text{K}$) are reported [77-80]. Recently, Bedoya-Pinto et al show that a

single CrCl_3 monolayer on graphene/6H-SiC (0001) is a 2D-XY magnetic system without out-of-plane magnetic anisotropy [81]. These intrinsic 2D magnets provide a novel platform for spintronic applications due to their unique and intriguing physical properties. In 2018, Song et al utilize CrI_3 multilayers to construct spin-filter magnetic tunnel junction, where significant TMR ratio amounting to 19000% is achieved [82]; furthermore, Cardoso et al propose the concept of van der Waals (vdW) spin valve that graphene bilayers are sandwiched by two CrI_3 monolayers, and band structures of bilayer graphene can be directly controlled by magnetic coupling behavior of CrI_3 monolayers [83]. In 2018, Deng et al raise the T_c of Fe_3GeTe_2 up to room temperature by applying an ionic gate [80], and in 2019, Wang et al realize spin-orbit torque (SOT)-driven magnetization switching of few-layered Fe_3GeTe_2 in $\text{Fe}_3\text{GeTe}_2/\text{Pt}$ heterostructure, where SOT arises from spin current in Pt layers [84].

1.2 Aim and objectives

The discovery of 2D magnets provides a novel platform for spintronic research. However, lots of fundamental problems, including small PMA, weak valley polarization, low Curie temperature and crystal symmetry prohibited DMI, have not been ideally resolved, which largely impedes the practical applications of 2D magnets. The aim of this thesis is to propose effective and general approaches for solving these fundamental problems and give appropriate material candidates that could be applied in the next-generation spintronic devices.

Following the aim of thesis, we give the specific research objectives:

1. Elucidate the energy source and configure out the physical origin of PMA in 2D magnets. Based on the physical picture, we will propose the novel approach that could effectively enhance the PMA, and design 2D material systems with large PMA.

2. Elucidate the relationship between spin and valley freedom of electrons in ferrovalley materials. We will investigate the influence of spin orientation on the valley polarization. Based on the physical picture of spin-valley coupling, we will give some material candidates with intrinsic large valley polarization.

3. Construct 2D magnets without inversion symmetry for achieving large DMI. By calculating all magnetic interaction parameters, we will determine what 2D magnets could hold topological magnetism.

4. Reveal physical characters, such as mechanical and electronic properties, of 2D magnets that hold topological magnetism. According to these characters, we will design some methods for effective controlling crucial features of topological spin textures including morphology, density, creation or annihilation.

5. Discuss about the possible applications of investigated 2D magnets in practical spintronic devices.

1.3 Thesis structure

The thesis contains 8 chapters. In the chapter 1, we give a brief introduction of spintronics and 2D vdW materials and show the aim and objectives of this thesis.

In chapter 2, we summarize that works have been done in the field of 2D magnets and reveal what challenges are urgent to be resolved. We also give a detailed introduction of methods that are chosen for solving challenges.

In chapter 3, we show and illustrate that the interlayer distance decreasing of Gr/NiI₂ HS significantly enhances the PMA of NiI₂. We also find that at the same time, QAHE is realized in graphene due to the proximity effects-induced perpendicular ferromagnetism and Rashba SOC. In chapter 4, we further demonstrate that intrinsic PMA in 2D magnets can give rise large valley polarization, which is crucial for realizing practical applications of valley freedom. We find that sizable valley splitting (~60 meV) could be achieved in a recently discovered 2D magnet, VSi₂N₄, when spin orientation is perpendicular to the sample plane.

In chapter 5, we construct 2D Janus magnets, CrXTe ($X=S, Se$), with breaking inversion symmetry. The large DMI is achieved in CrSeTe monolayer resulting in chiral magnetism. And these chiral spin textures can be effectively manipulated via applying strain. Moreover, the T_c of CrXTe system is significantly enhanced over room temperature under tiny tensile strain.

In chapter 6, we further demonstrate that electric control of topological magnetic phases can be realized in Janus magnet-based multiferroic heterostructure, i.e., MBST/In₂Se₃. The loops of vortex and antivortex are transformed into skyrmion particles when ferroelectric polarization of In₂Se₃ is switched.

In chapter 7, we propose and demonstrate that a family of 2D magnets with $P\bar{4}m2$ symmetry hold anisotropic DMI, which is obviously different from isotropic DMI in Janus magnets. The cooperation between this crystal symmetry-protected DMI and other magnetic parameters results in lots of non-trivial FM/AFM topological spin configurations in this family.

Finally, in chapter 8, we summarize the results and findings of this thesis and

give some comments about what the future possibly hosts in 2D magnets.

Chapter 2 Literature Review

2.1 Magnetic anisotropy of 2D magnets

MTJ, as the key component in STT-MARM, consist of two FM electrodes separated by an insulating barrier. The stability factor of MTJ is read as: $\Delta = K_u V / 2k_b T$, where K_u , V , k_b and T represents PMA of FM electrode, volume of FM electrode, Boltzmann constant and temperature respectively [85]. One can see that for guaranteeing high stability and small size of MTJ, it is naturally required that FM electrode processes strong PMA. In 2018, Song et al first realize vdW MTJ consisted of CrI₃ multilayer [82]. Although they observe recorded TMR ratio reaching to 19000%, the device only works at extremely low temperature around 2K. Notably, the strong PMA opens a large magnon excitation gap, which further stabilizes long-range magnetic order at finite temperature [86].

For a 2D system without magnetic anisotropy, there is no spin wave excitation gap [see Fig. 2.1(a)]. Based on spin-wave theory, the gapless magnon will cause magnetic order collapsed in one- and two-dimensional systems. However, the magnetic anisotropy gives rise the non-zero excitation gap [see Fig. 2.1(b)-(d)], which results in stability of long-range magnetic order at finite temperature. For multilayer system, magnon density of states (DOS) exhibit the stage function of energy, and for bulk system, magnon DOS is proportional to the root of energy. Therefore, when thickness of the material keeps increasing, higher temperature is required to ensure enough excitation for destroying magnetic order.

Lots of efforts have been devoted to enhancing the magnetic anisotropy of 2D magnets. Yang et al theoretically propose that large compressive strain (~10%) can increase PMA of CrI₃ monolayer from 1.6 meV/atom to 3.0 meV/atom [87]. However, such large compressive strain is very hard to apply on 2D materials. Furthermore, both hole doping and alloying methods are predicted to be able to enhance the PMA [88, 89]. Unfortunately, the magnitude of PMA enhancement is also limited in these

approaches. Therefore, we propose and demonstrate a novel method for effective tuning magnetic anisotropy of 2D magnets in chapter 3.

Moreover, lacking of PMA does not definitely indicate that the long-range magnetic order cannot exist in two-dimensional limit. Mermin-Wanger rules only describe the situation of isotropic Heisenberg model where the orientation of spin vector has no constraints in a 3D sphere [see Fig. 2.2(c)]. There are two other models for describing the 2D magnetism, which are Ising model and XY model. In Ising model, the spin only has two possible states which are “up” and “down” as shown in Fig. 2.2(a) [90]. Onsager first demonstrate the second-order phase transition of Ising model in 2D case, which is further confirmed by experimental observations [91]. In XY model, spin rotates in the materials plane [see Fig. 2.2(b)], and lacking of PMA indicates that there is no excitation gap of magnon spectrum [92, 93]. However, the finite-size Berezinskii-Kosterlitz-Thouless (BKT) phase transition could emerge in 2D XY systems. This feature has been observed in CrCl_3 monolayer grown on Graphene/6H-SiC (0001) [81].

PMA is not only closely related to magnetic order of 2D magnets but also has strong impacts on electronic band structures [94]. For example, the perpendicular ferromagnetism component could turn quantum spin Hall state to quantum anomalous Hall state [29]. We indeed observe that QAHE is realized in graphene layer when PMA of NiI_2 enhances [see detailed discussion in chapter 3].

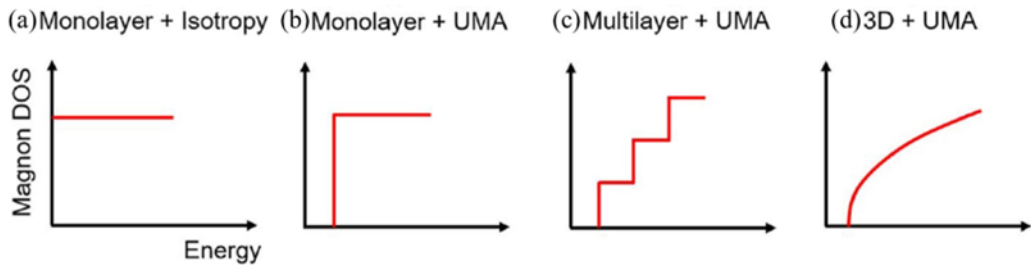


Fig. 2.1 The magnon dos schematics of four states which are (a) monolayer magnet without magnetic anisotropy, (b) monolayer magnet with uniaxial magnetic anisotropy, (c) multilayer magnet with uniaxial magnetic anisotropy, and (b) bulk magnet with uniaxial magnetic anisotropy. This figure is adopted from Ref. 86.

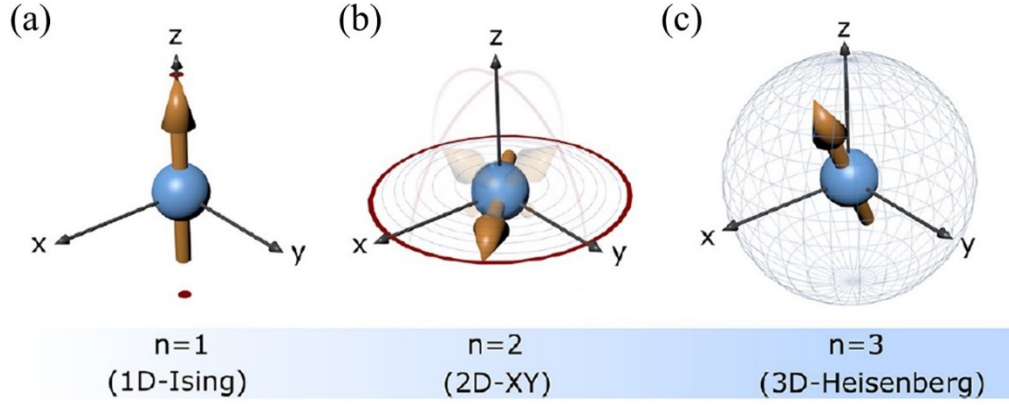


Fig. 2.2 The spin vector in (a) 1D-Ising model, (b) 2D-XY model and (c) 3D-Heisenberg model. In Ising model, the spin only has two possible states (“up” and “down” states); In XY model, the spin is constrained in the material plane; and In Heisenberg model, the spin vector could align in any orientation of a 3D sphere. This figure is adopted from Ref. 93

2.2 Valley characters of 2D materials

Valley represents the minimum/maximum points of electronic band structures in reciprocal space. In graphene or group-VI transition metal dichalcogenides (TMD) such as MoS₂ and WSe₂ [see Fig. 2.3(a)], two inequivalent valley appears at -K and +K points in Brillouin zone [see Fig. 2.3(b)]. One important and interesting feature of valleys is that the electrons can be excited optionally by circularly polarized light, which is called as optional selection rules [65-70].

Selection rules at $\pm K$ points are the natural consequence of C_3 rotation symmetry. Elements of optical transition matrix can be written as:

$$\langle \psi_{vk} | \widehat{P}_{\pm} | \psi_{ck} \rangle = \langle C_3 \psi_{vk} | C_3 \widehat{P}_{\pm} C_3^{-1} | C_3 \psi_{ck} \rangle = e^{i\frac{2}{3}\pi(l_c - l_v \mp 1)} \langle \psi_{vk} | \widehat{P}_{\pm} | \psi_{ck} \rangle$$

where \widehat{P}_{\pm} represents momentum operator, and $l_c(l_v)$ represents the azimuthal quantum number. For MoS₂, the conduction band minimum at $\pm K$ points are dominated by d_{z^2} states, and the valence band maximum at $\pm K$ points are dominated by $d_{x^2-y^2}$ and d_{xy} states. The azimuthal quantum number $l_c(l_v)$ for $\pm K$ points equals $\pm 1(0)$.

Therefore, we have $P_+ = P_+$ and $P_- = e^{i\frac{4}{3}\pi} P_-$ at +K point. The later equation

indicates $P_- = 0$. Similarly, we have $P_+ = 0$ and $P_- = P_-$ at $-K$ point. According to degree of circular polarization $\eta(\mathbf{k}) = \frac{|P_+|^2 - |P_-|^2}{|P_+|^2 + |P_-|^2}$, the optical absorption at $+K$ ($-K$) can only be excited by left-hand (right-hand) light.

When valleys do not degenerate in energy level, the hole doping or electron doping can give rise carriers from just one valley. And the carriers excited from different valleys process the opposite transverse velocity due to the different sign of Berry curvature as shown in Fig. 2.3(c) [65]. Using Hall bar geometry [see Fig. 2.3(d)], the valley Hall effects and the transverse motion of excited electrons are detected by the nonlocal resistance. When electrical field is applied on MoS₂ bilayer, the inversion symmetry breaking of systems results in the valley polarization. Therefore, the valley Hall effect is observed by magneto-optical Kerr effect [72]. The electrons with opposite spin polarization accumulate at two edges of sample as shown in Fig. 2.3(e).

Also, it is well known that the key of practically applying valley freedom in electronic devices is inducing the large valley polarization. Since valley and spin are coupled with each other, the magnetism freedom, such as external magnetic field [95, 96], magnetic doping [97, 98] and magnetic proximity effects [99, 100], is used to break valley degeneracy. However, the band splitting induced by an external magnetic field is very small, about 0.1 meV/T [101]; magnetic dopants tend to form clusters limiting the quality of the systems [102]; and for magnetic proximity effects, the substrate usually deforms electronic states of the host. For overcoming these shortcomings, materials are required to combine intrinsic long-range magnetism and valley characters at the same time. That system is called as “ferrovalley” materials [103]. We further notice that despite perpendicular magnetism component is normally applied to induce valley polarization, the specific relationship between valley polarization and spin direction is unclear. Therefore, in chapter 4, we elucidate the mathematic relationship between valley and spin orientation in “ferrovalley” materials and demonstrate that the anomalous valley Hall effect can be induced when materials process PMA.

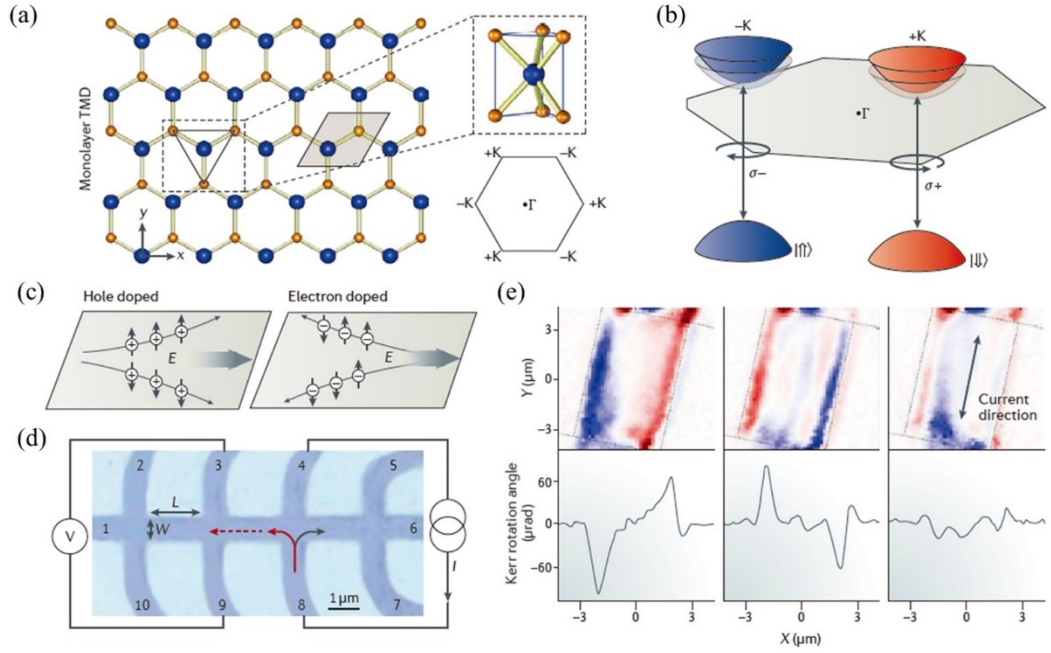


Fig. 2.3 (a) Crystal structure and Brillouin zone of TMD monolayer. (b) Two inequivalent valleys of MoS_2 monolayer. (c) Schematics of the valley Hall effect. Excited carriers process a transverse velocity under in-plane electric field. (d) Hall bar geometry for detecting valley Hall effect. (e) The accumulation of spin-polarized electrons at the sample edge of MoS_2 monolayer. This figure is adopted from Ref. 70.

2.3 Magnetic skyrmion

The magnetic skyrmion is a swirling spin configuration in magnetic materials. For skyrmion, the topological number is defined as: $Q = \frac{1}{4\pi} \int \mathbf{S} \cdot (\partial_x \mathbf{S} \times \partial_y \mathbf{S}) d^2r$. Due to topological protection, the skyrmion cannot be twisted into other magnetism with different Q . Based on the configurations of spin propagation between uniform magnetic states, there are two types of skyrmion are defined, Bloch- and Neel-type skyrmion [see Fig. 2.4(a) and (b)]. The earliest discovery of skyrmion is in the non-centrosymmetric B_{20} bulk materials such as MnSi [104], FeCoSi [105] and FeGe [106]. The skyrmion particles discovered in B_{20} are Bloch-type skyrmion. In the past decades, lots of efforts have been devoted to achieving strong DMI in ferromagnetic metal/heavy metal multilayers, resulting in formation of topological magnetism [107-

110]. As shown in Fig. 2.4(c) and (d), skyrmion lattice and solitons are observed by spin-polarize scanning tunneling microscopy in Fe/Ir(111) and PdFe/Ir(111) HSs respectively. The interfacial DMI results in these skyrmion particles are Neel-type. Due to small size, stable configuration, and electrical current-controlled motion, skyrmion is considered as ideal information carrier in the next-generation spintronic devices with high density and low energy consumption. However, there are two crucial problems unsolved: (i) heavy metal cannot be ideally compatible with modern complementary metal–oxide–semiconductor (CMOS) technology, largely impeding practical applications of ferromagnetic metal/heavy metal multilayers in memory chips and (ii) heavy metal processes large Gilbert damping constant, thus indicating that large current density is necessary for manipulating magnetism [111, 112]. The emergence of 2D magnets provides a new platform for achieving topological magnetism in several atom thickness and avoids the applications of heavy metals. Unfortunately, most discovered 2D magnets process inversion symmetry. Therefore, DMI is prohibited by symmetry requirements, which means that topological magnetism is hard to be realized. In chapter 5~6, we show that inversion symmetry of 2D magnets can be broken by constructing Janus magnets. The significant DMI induce various chiral spin configurations in these Janus magnets. Moreover, we first demonstrate that strain and electric field are effective methods for tuning topological magnetism. Although ferromagnetic topological magnetism stabilized by isotropic DMI has been observed in 2D magnets, anisotropic DMI and antiferromagnetic topological remain elusive. Therefore, in chapter 7, we propose and demonstrate crystal symmetry-protected anisotropic DMI in AX_2 monolayer with $P\bar{4}m2$ layer group. We further observe various AFM topological magnetism in AX_2 monolayer.

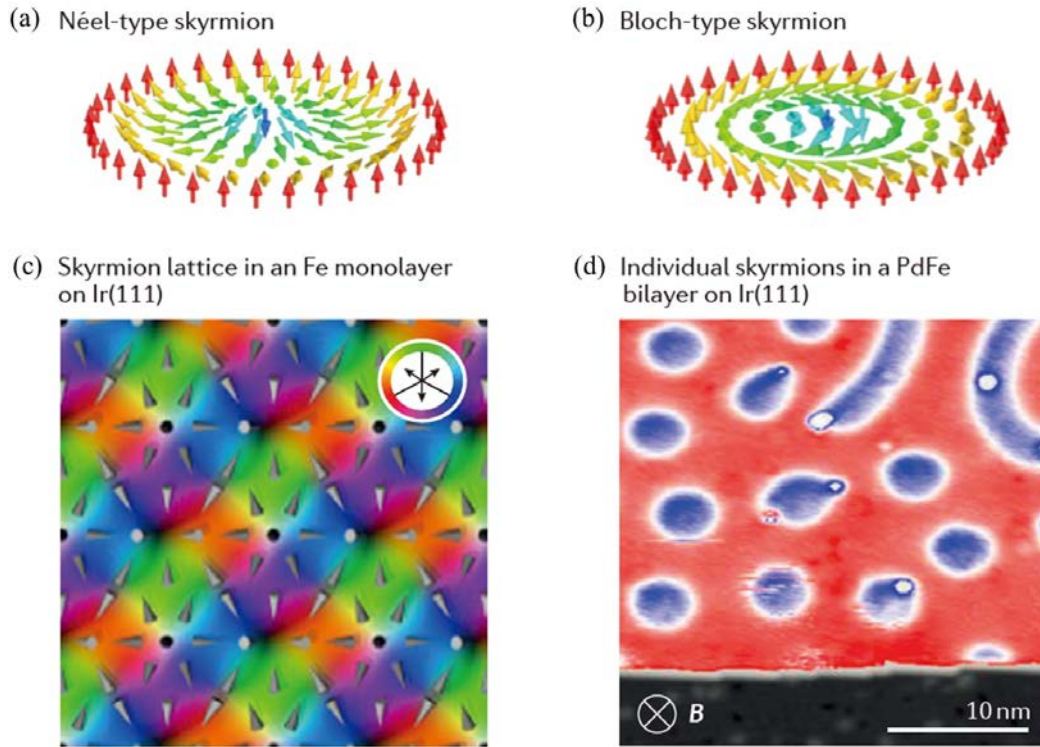


Fig. 2.3 Spin configurations of (a) Néel-type skyrmion and (b) Bloch-type skyrmion. (c) Skyrmion lattice observed by spin-polarized scanning tunneling microscopy in Fe/Ir(111) interface. (d) Skyrmion solitons observed by the same technique in PdFe/Ir(111) interface. This figure is adopted from Ref. 39.

2.4 Density Functional Theory

Schrödinger equation is the basic equation for describing the condensed matter systems. Based on materials properties, such as crystal structure and atomic type, one can construct the corresponding Hamiltonian and then apply Schrödinger equation to strictly describe physical properties such as lattice constant, electronic band structures and energy eigenvalue etc. However, excepts for hydrogen-like systems, a realistic system normally contains huge numbers of interacted particles ($\sim 10^{23}$), which indicates that obtaining the analytical results of Schrödinger equation is extremely hard. Therefore, some approximated methods are developed for calculating numerical results. And for this propose, that density functional theory (DFT) is one of the most versatile and widely used tool. In the case of DFT, the spatially dependent charge density rather than wave function is chosen to construct energy functionals.

For a multi-electrons system, the time independent Schrödinger equation is written as:

$$\hat{H}\psi = E\psi \quad (1.1)$$

where \hat{H} and E represents the Hamiltonian and energy of system respectively. \hat{H} is written as:

$$\hat{H} = \hat{T}_N + \hat{T}_e + \hat{V}_{ee} + \hat{V}_N + \hat{V}_{e-N} \quad (1.2)$$

where \hat{T}_N , \hat{T}_e , V_{ee} , V_N and V_{e-N} represents kinetic energy of the nuclei (N), kinetic energy of the electrons (e), coulomb interaction potential of electrons, coulomb interaction potential of nuclei and coulomb interaction potential of the electrons-nuclei respectively. These terms are explicitly written as: $\hat{T}_N = -\sum_i \frac{\hbar^2}{2M_i} \nabla_{\mathbf{R}_i}^2$; $\hat{T}_e = -\sum_j \frac{\hbar^2}{2m_j} \nabla_{\mathbf{r}_j}^2$; $\hat{V}_{ee} = \sum_{i<j}^{N_e} \sum_j^{N_e} \frac{e^2}{|\mathbf{r}_i - \mathbf{r}_j|}$; $\hat{V}_{eN} = -\sum_i^N \sum_j^{N_e} \frac{Z_i e^2}{|\mathbf{R}_i - \mathbf{r}_j|}$; $\hat{V}_{NN} = -\sum_{i<j}^N \sum_j^N \frac{Z_i Z_j e^2}{|\mathbf{R}_i - \mathbf{R}_j|}$. Here, $\nabla_{\mathbf{R}_i}^2$ represents the Laplacian operator on the i^{th} position of nuclei (electron) with mass M_i (m_i) and charge $Z_i e$ (e). In 1927, the Born-Oppenheimer (BO) approximation points out that since mass of nuclei is much larger than that of electron, and velocity of nuclei is much smaller than electron in a solid system, the motion of nuclei and electrons can be separated from each other [113]. The wave function ψ are further written as $\psi = \psi_N(\mathbf{R})\psi_e(\mathbf{r}, \mathbf{R})$, where $\psi_N(\mathbf{R})$ and $\psi_e(\mathbf{r}, \mathbf{R})$ represents the wave function of nuclei and electron part respectively [114]. \hat{H} of multi-electrons system are rewritten as:

$$\hat{H} = \hat{T}_e + \hat{V}_{ee} + \hat{V}_{e-N} \quad (1.3)$$

where \hat{V}_{e-N} is treated as the external potential \hat{V}_{ext} . Notably, it is still hard to resolve coulomb interaction between electrons.

In 1964, Hohenberg and Kohn propose that a universal functional of electronic density $\rho(\mathbf{r})$ can be used to determine the ground state of interacting electron gas, which is later considered as the basic framework of DFT [115]. Specifically, there are two theorems:

Theorem 1: for a multi-electron system, the external potential $V_{ext}(\mathbf{r})$ is the unique functional of $\rho(\mathbf{r})$. Since the \hat{H} is determined by $V_{ext}(\mathbf{r})$, \hat{H} is also the unique

functional of $\rho(\mathbf{r})$. In principle, all the properties of system can be determined by $\rho(\mathbf{r})$.

Proof: It is assumed that there are two different external potential V_{ext}^1 and V_{ext}^2 with the same ground state electronic states $\rho(\mathbf{r})$, which leads to two different Hamiltonian $\hat{H}^1 = \hat{T}_e + \hat{V}_{ee} + \hat{V}_{ext}^1$ and $\hat{H}^2 = \hat{T}_e + \hat{V}_{ee} + \hat{V}_{ext}^2$, ground state wavefunction ψ_0^1 and ψ_0^2 , ground state energy E_0^1 and E_0^2 . Choosing ψ_0^2 and ψ_0^1 as the variational function of \hat{H}^1 and \hat{H}^2 respectively, one can obtain:

$$E_0^1 < \langle \psi_0^2 | \hat{H}^1 | \psi_0^2 \rangle = E_0^2 + \int \rho(\mathbf{r}) (V_{ext}^1 - V_{ext}^2) d\mathbf{r}. \quad (1.4)$$

$$E_0^2 < \langle \psi_0^1 | \hat{H}^2 | \psi_0^1 \rangle = E_0^1 - \int \rho(\mathbf{r}) (V_{ext}^1 - V_{ext}^2) d\mathbf{r}. \quad (1.5)$$

By adding Eq 1.4 and 1.5, one can obtain: $E_0^1 + E_0^2 < E_0^2 + E_0^1$, which is a contradictory result. Therefore, when the electronic density is precisely given, ground state wavefunction and energy can't be degenerated.

Theorem 2: One can define the universal energy functional $E(\rho)$ of electronic density $\rho(\mathbf{r})$. For any specific V_{ext} , the $\rho(\mathbf{r})$ that globally maximizes $E(\rho)$ is the ground state electronic density of the system.

Proof: the ground state energy E_0 can be written as:

$$E_0 = \min_{\rho \rightarrow N} (\min_{\psi \rightarrow \rho} \langle \psi | \hat{T}_e + \hat{V}_{ee} + \hat{V}_{ext} | \psi \rangle) \quad (1.6)$$

where $\psi \rightarrow \rho$ represents the set of all wavefunctions for a certain electronic density ρ , and $\rho \rightarrow N$ represents the set of all electronic densities for a certain system with N electrons. The external potential operator can be replaced by the integral of ρ , and Eq 1.6 is rewritten as:

$$E_0 = \min_{\rho \rightarrow N} (F_{intr}[\rho(\mathbf{r})] + \int \rho(\mathbf{r}) (V_{ext}) d\mathbf{r}) = \min_{\rho \rightarrow N} E[\rho(\mathbf{r})] \quad (1.7)$$

where $F_{intr}[\rho(\mathbf{r})] = \min_{\psi \rightarrow \rho} \langle \psi | \hat{T}_e + \hat{V}_{ee} | \psi \rangle$ called as the Hohenberg-Kohn functional.

From Eq 1.7, one can see that as long as $F_{intr}[\rho(\mathbf{r})]$ is determined, the energy minimized by a certain electronic density is just the ground state energy of the system.

In Kohn–Sham density functional theory, the total energy of a multi-electron system is expressed as the functional of $\rho(\mathbf{r})$:

$$E[\rho(\mathbf{r})] = T[\rho(\mathbf{r})] + \frac{e^2}{2} \iint \frac{\rho(\mathbf{r})\rho(\mathbf{r}')}{|\mathbf{r}-\mathbf{r}'|} d\mathbf{r}d\mathbf{r}' - \int \rho(\mathbf{r}) (V_{ext}(\mathbf{r}))d\mathbf{r} + E_{xc}[\rho(\mathbf{r})] \quad (1.8)$$

where $\rho(\mathbf{r}) = \sum_i \varphi_i^*(\mathbf{r}) \varphi_i(\mathbf{r})$ represents the electronic density, the second term represents the coulomb interaction, and $V_{ext}(\mathbf{r})$ represents external potential. Despite the specific forms of kinetic energy $T[\rho(\mathbf{r})]$ and exchange-correlation energy $E_{xc}[\rho(\mathbf{r})]$ are unknown, Eq 1.8 can be variationally calculated as:

$$\frac{\delta T[\rho(\mathbf{r})]}{\delta \rho(\mathbf{r})} + V_{ext}(\mathbf{r}) + e^2 \int \frac{\rho(\mathbf{r}')}{|\mathbf{r}-\mathbf{r}'|} d\mathbf{r}' + \frac{\delta E_{xc}[\rho(\mathbf{r})]}{\delta \rho(\mathbf{r})} = \varepsilon. \quad (1.9)$$

then, one can define an effective potential as:

$$V_{eff}(\mathbf{r}) = V_{ext}(\mathbf{r}) + e^2 \int \frac{\rho(\mathbf{r}')}{|\mathbf{r}-\mathbf{r}'|} d\mathbf{r}' + V_{xc}(\mathbf{r}) \quad (1.10)$$

where $V_{xc}(\mathbf{r}) = \frac{\delta E_{xc}[\rho(\mathbf{r})]}{\delta \rho(\mathbf{r})}$ represents the exchange-correlation potential. Although the kinetic energy functional of interacted multi electrons $T[\rho(\mathbf{r})]$ is unclear, one can explicitly give the functional of system without considering electrons interacting, $T_s[\rho(\mathbf{r})] = \frac{\hbar^2}{2m} \sum_i \int \varphi_i^*(\mathbf{r}) \cdot (-\nabla^2) \varphi_i(\mathbf{r}) d\mathbf{r}$, to replace $T[\rho(\mathbf{r})]$, and include the different part between $T[\rho(\mathbf{r})]$ and $T_s[\rho(\mathbf{r})]$ in $E_{xc}[\rho(\mathbf{r})]$. Therefore, one can obtain the Schrödinger equation of a single electron which is called as Kohn-Sham (KS) equation [116]:

$$\left[-\frac{\hbar^2}{2m} \nabla^2 + V_{eff}(\mathbf{r}) \right] \varphi_i(\mathbf{r}) = \varepsilon_i \varphi_i(\mathbf{r}). \quad (1.11)$$

If the $V_{xc}(\mathbf{r})$ are known, one can obtain the exact ground state energy of multi-electrons system. Above results also mean that the effectiveness of DFT fully depends on the accuracy and simplicity of $E_{xc}[\rho(\mathbf{r})]$.

$E_{xc}[\rho(\mathbf{r})]$ has to be simplified in solving practical problems. One commonly applied approximation is the local density approximation (LDA) [116]. For homogeneous electron gas, $E_{xc}[\rho(\mathbf{r})]$ depend on $\rho(\mathbf{r})$ locally, which indicates that except for \mathbf{r} , small variation of $\rho(\mathbf{r})$ will not induce the variation of energy density at the other places. Therefore, $E_{xc}[\rho(\mathbf{r})]$ can be written as:

$$E_{xc}^{LDA}[\rho(\mathbf{r})] = \int \rho(\mathbf{r}) \varepsilon_{xc}(\rho(\mathbf{r})) d\mathbf{r} \quad (1.12)$$

where $\varepsilon_{xc}(\rho(\mathbf{r}))$ represents exchange-correlation energy of single electron in homogeneous electron gas with density $\rho(\mathbf{r})$. $\varepsilon_{xc}(\rho(\mathbf{r}))$ can be further distributed to contributions from exchange energy ε_x and correlation energy ε_c :

$$\varepsilon_{xc}(\rho(\mathbf{r})) = \varepsilon_x(\rho(\mathbf{r})) + \varepsilon_c(\rho(\mathbf{r})) \quad (1.13)$$

where $\varepsilon_x(\rho(\mathbf{r}))$ is analytically written as $\varepsilon_x = -\frac{3}{4}(3\rho(\mathbf{r})/\pi)^{1/3}$. The next logical step after LDA is gradient expansion approximation (GEA) where a weak and slowly-varying potential is introduced for describing the inhomogeneous electron gas [117]. However, GEA turns out to be even worse than LDA, since the sum rule $\int h_{xc}(\boldsymbol{\tau}_1, \boldsymbol{\tau}_2) d\boldsymbol{\tau}_2 = -1$ and $h_x \leq 0$ are violated. The failure of GEA leads to the development of generalized gradient approximation (GGA) [118]. $E_{xc}[\rho(\mathbf{r})]$ is written as:

$$E_{xc}^{GGA}[\rho(\mathbf{r})] = \int \rho(\mathbf{r}) \varepsilon_{xc}(\rho(\mathbf{r}), |\nabla\rho(\mathbf{r})|) d\mathbf{r} \quad (1.14)$$

where $\nabla\rho(\mathbf{r})$ represents the electronic density gradient. $E_{xc}^{GGA}[\rho(\mathbf{r})]$ can also be written as the sum of exchange energy and correlation energy: $E_{xc}^{GGA}[\rho(\mathbf{r})] = E_x^{GGA}[\rho(\mathbf{r})] + E_c^{GGA}[\rho(\mathbf{r})]$. In order to solve problems in GEA, some limited conditions that hole must obey are added. For example, the h_x will be set to 0 mandatorily if $h_x > 0$ emerges. For satisfying the sum rule, GGA is built with real-space cutoffs of h_x and h_c , and only h_x contains one electron charge. It is believed that the GGA gives more accurate DFT results for systems with obvious inhomogeneous electron density. There are various types of GGA functionals proposed. The most popular one is the Perdew-Burke-Ernzerhof (PBE) functional which is only determined by the physical nature of solid system [119].

2.5 Tight-binding and atomic spin model

We adopt the tight-binding model for describing low-energy bands in materials with non-trivial electronic structures, thus helping us determine the important physical terms in studied systems. The tight-binding model use an approximate set of wave functions based on superposition of wave functions for isolated atoms located at each atomic site [120]. Since this method is based on the crystal symmetry and

wave function of specific atom orbitals that can be explicitly determined by first-principles calculations, it is expected that an accurate description of solid systems is given [120].

We next show how a simple tight-binding model gives the electronic band structures of graphene. When only considering the nearest-neighboring hopping terms, the tight-binding Hamiltonian is written as: $\hat{H} = -t \sum_{\langle i,j \rangle} (\hat{a}_i^* \hat{b}_j + \hat{b}_i^* \hat{a}_j)$, where i (j) represents the site in A (B) sublattice, and \hat{a}_j (\hat{a}_j^*) represents the creation (annihilation) operator of electrons. The Hamiltonian can be rewritten as the sum over the nearest-neighboring sites as: $\hat{H} = -\sum_{i \in A} \sum_{\delta} (\hat{a}_i^* \hat{b}_{i+\delta} + \hat{b}_i^* \hat{a}_{i+\delta})$, where δ are vectors between different sites. By performing Fourier transformation, the Hamiltonian is expanded as:

$$\hat{H} = \Psi^* h(\mathbf{k}) \Psi,$$

where $\Psi^* = \begin{pmatrix} \hat{a}_k \\ \hat{b}_k \end{pmatrix}$, $\Psi = \begin{pmatrix} \hat{a}_k \\ \hat{b}_k \end{pmatrix}$, $h(\mathbf{k}) = -t \begin{pmatrix} 0 & \sum_{\delta} e^{i\mathbf{k} \cdot \mathbf{r}} \\ \sum_{\delta} e^{-i\mathbf{k} \cdot \mathbf{r}} & 0 \end{pmatrix}$.

The band structures can be directly obtained by solving the eigenvalue of $h(\mathbf{k})$.

Atomic spin model simulations are performed for describing spin dynamics in 2D magnets. In traditional micromagnetic simulations, the thickness of magnetic layer is a necessary parameter for transferring DFT-obtained exchange couplings into corresponding micromagnetic parameters [121]. However, since the magnetic layer of 2D magnets consists of one atom layer of magnetic elements, the thickness cannot be defined. Interestingly, DFT-obtained exchange couplings are directly considered in simulations for atomic spin model, which thus gives a better description of spin configurations. Based on DFT results, the spin Hamiltonian of 2D magnets is defined. The effect field in Landau–Lifshitz–Gilbert (LLG) equation is then defined as the partial derivative of Hamiltonian with respect to spin vector. Therefore, the LLG equation can be numerically resolved just based on the spin Hamiltonian and crystal lattice of magnetic atom. Normally, the LLG equation describes well the metastable spin configurations such as skyrmion and bimeron while fails to give the ground states. Using atomic spin model, one can obtain the explicit energy of a 2D magnet

with any determined spin configurations. Furthermore, one can perform Monte Carlo simulations to search the ground spin states.

2.6 Summary

PMA plays the crucial role in stabilizing magnetic order of Heisenberg model-described 2D magnetism. By opening magnon excitation gap, the magnetism could survive at the finite temperature. Interestingly, for XY model-described 2D magnetism, the long-range magnetism is expected to emerge as the format of vortex-antivortex pairs. PMA also plays crucial role in the performance of spintronic devices. Therefore, lots of efforts have been devoted to enhancing magnetic anisotropy of 2D magnets. However, the enhancement amplitude of PMA in most methods is quite limited. On the other hand, magnetization orientation is closely hinged on spin-polarized band structures. For example, the PMA can give rise QAHE and AVHE. Also, the critical temperature of most discovered 2D magnets is far below the room temperature, which largely impedes practical applications.

Besides charge and spin, valley is another freedom of electrons. The excited carriers could process the transverse velocity due to the Berry curvature and accumulate at the sample edges. For obtaining the net charge/spin Hall signal, valley polarization is necessary for materials. However, it is hard to achieve large valley polarization in experiments.

Magnetic skyrmion, a swirling spin configuration which topological protection, is considered as the ideal information carrier in the next-generation spintronic devices. One key parameter in skyrmion formation is DMI that requires inversion symmetry breaking of systems. Despite 2D magnets provide a novel platform for spintronic research, the inversion symmetry preserves in most 2D magnets, which thus prohibit the DMI. Since topological magnetism is considered as the information carrier, it is necessary to realizing effective control of physical properties of these spin textures including morphology, density, creation or annihilation.

Using first-principles calculations within DFT theory, tight-binding model and atomic spin model, we conduct the research as detailedly introduced in the later chapters for solving above challenges in the field of 2D magnets. In these works, we provide novel approaches and corresponding material systems for realizing strong PMA, large valley polarization (over room temperature), high Curie temperature, inversion symmetry breaking and strong DMI, and effective manipulation of topological magnetism in 2D magnets. These findings hopefully answer the question that what 2D magnets can be practically applied in the next-generation spintronic devices with low-energy consumption and high-storage density.

Chapter 3 Proximity Effects in Gr/NiI₂

Heterostructure

3.1 Introduction

The 2D FM semiconductors, which integrate the magnetism, semiconductivity and miniaturization, is very promising for spintronic applications, such as the magnetic tunnel junction, spin valve and spin-field-effect transistor [122-125]. Tremendous effort has been devoted to inducing ferromagnetism in 2D semiconductors, such as magnetic elements doping [123, 124], atom adsorption [58, 126-129] and defects (or boundary) engineering [130-133]. Recently, the experimental progress has led to a breakthrough in the synthesis of 2D vdW semiconductors with intrinsic ferromagnetism, which are first realized in Cr₂GeTe₃ bilayers [76], then in CrX₃ (X=Cl, Br, I) monolayers [75, 134]. In these materials, the uniaxial magnetic anisotropy plays an important role in suppressing the spin excitation and protecting the long-range magnetic order in finite temperature [74, 135, 136]. Compared with in-plane magnetic anisotropy (IMA), the large PMA is more beneficial for realizing the high-density information storage devices with low energy consumption and high thermal stability [7, 84, 137-139]. Graphene coating has been proved to be able to significantly enhance the PMA of Co films by tuning electronic states of Co 3*d* orbitals [140]. It is also noticeable that the physical properties of vdW structures are very sensitive to the interlayer spacing [141-148]. The interlayer magnetic order of CrI₃ can be tuned via applying a hydrostatic pressure [144], the correlated electronic states and interlayer coupling of twisted bilayer graphene can be effectively tuned by varying interlayer spacing [145, 146], and the power conversion efficiency of SbI₃/BiI₃ heterostructure can be enhanced by decreasing interlayer distance [148]. Above results indicate that it should be possible to tune magnetic anisotropy of 2D FM semiconductors via changing the interlayer distance of graphene-based vdW heterostructure. In addition, the FM substrate can also induce

proximity effects in graphene [149-153]. By introducing the ferromagnetism and enhancing the SOC through proximity with FM semiconductor substrates, graphene can become an ideal platform to realize QAHE. In the heterostructures of graphene/CrI₃ and graphene/CrBr₃, QAHE have been reported theoretically via decreasing the interlayer distance to enhance the proximity effect [154-156]. Thus, besides the control of PMA, graphene-based vdW heterostructures also provide an opportunity to realize QAHE.

In this chapter, using first-principles calculations and low-energy effective model, we systematically investigate the magnetic anisotropy and QAHE by varying the interlayer distance of Gr/NiI₂ heterostructure. The bulk NiI₂ is a layered antiferromagnetic insulator with Néel temperature $T_N=75$ K [157]. Recently, NiI₂ monolayer is reported to be a 2D FM semiconductor [158-160] with sizable band gap and high Curie temperature T_c (above 120K), plus that it has small lattice mismatch with graphene, which makes Gr/NiI₂ a promising vdW system for investigating both magnetic and topological properties. We find that the PMA of NiI₂ monolayer can be effectively enhanced by decreasing the interlayer distance of Gr/NiI₂. By analyzing atomic-resolved magnetic anisotropy energy (MAE), orbital-hybridization-resolved MAE and density of states (DOS), we find that the magnetic anisotropy enhancement in NiI₂ mainly originates from the electronic states variation of I atoms influenced by the vicinity to graphene. More interestingly, by decreasing interlayer distance, a large exchange splitting and an enhanced Rashba SOC can be induced simultaneously in graphene, which can lead to the QAHE.

3.2 Methodology

We performed first-principles calculations using density functional theory (DFT) as implemented in the Vienna *ab initio* simulation package (VASP) [161-163]. The exchange correlation energy is calculated within the generalized gradient approximation (GGA) of Perdew-Burke-Ernzerhof (PBE) form. Considering the strongly correlated Ni 3*d* electrons in NiI₂, the GGA+U [164] method is adopted

($U_{eff} = 2-5$ eV). The atom coordinates are fully relaxed until the Hellmann-Feynman force is less than 10^{-2} eV/Å, and the cutoff energy is set to 520 eV. The Γ -centered k -point grids of $18 \times 18 \times 1$ and $6 \times 6 \times 1$ is good enough to sample the first Brillouin zones of NiI₂ and Gr/NiI₂, respectively. The DFT-D3 method [165] is applied in the calculations to correct the van der Waals interaction. A vacuum space of at least 15 Å in the direction normal to the layers is used to avoid interactions between periodic replicas. The MAE is defined as the energy difference between in-plane [100] and out-of-plane [001] magnetizations. All parameters are carefully tested and make the MAE to converge within 10^{-6} eV. To obtain the orbital-hybridization-resolved and layer-resolved MAE, the spin-orbit coupling is calculated for each orbital angular momentum, and one can get all the elements of spin-orbit coupling matrix. By comparing the SOC matrix between out-of-plane and in-plane magnetization, one can get orbital-hybridization-resolved MAE. The layer-resolved is the integration of MAE of all orbits for each atom. The transferred charge between graphene and NiI₂ layers is calculated based on the Bader charge analysis [166] as performed using program of Henkelman's Group [167-170]. The positive (negative) value of transferred charge represents the electron accumulation (depletion). The work function of graphene W_{Gr} is defined as the energy difference between vacuum level and Fermi level ($E_{vac} - E_F$), and the electron affinity of NiI₂ χ_{NiI_2} is calculated by the energy difference between vacuum level and conduction band minimum ($E_{vac} - E_C$).

3.3 Results and Discussion

3.3.1 Pristine NiI₂ and Gr/NiI₂ heterostructure

In a single layer of NiI₂ as shown in Fig. 3.1(a), Ni atoms form a hexagonal network sandwiched by two atomic planes of I atoms, with point group D_{3d} . The calculated parameters of NiI₂ including the optimized lattice constant a , magnetic moments of Ni (μ_{Ni}) and I (μ_I) atoms, band gap E_{gap} and nearest-neighboring exchange coupling J , are listed in Table 3.1. In the range of U_{eff} from 2 to 5 eV, the

lattice constants yield good comparison with the experimental value of bulk NiI₂, 3.90 Å [171]. When U_{eff} increasing, due to the stronger repulsion of localized electronic states, the μ_{Ni} and E_{gap} both increases. Notably, the I atoms is spin-polarized due to the magnetic proximity of Ni atoms. The value of J is positive regardless of U_{eff} , which means the ground magnetic state for NiI₂ is ferromagnetic. These basic properties of NiI₂ monolayer in previous works [158-160] are also provided in Table 3.1. One can see that the results show good agreements with previous researches. Although the specific value of band gap is not given in Ref. 159, this research reports that NiI₂ monolayer is a ferromagnetic semiconductor. Notably, a , μ_{Ni} , E_{gap} and J in our work when $U_{eff} = 4$ eV is very similar with the results in Ref. 159.

Table 3.1 The optimized lattice constants a , magnetic moments of Ni μ_{Ni} and I μ_I atoms, band gap energy E_{gap} , and nearest-neighboring exchange coupling J .

	a (Å)	μ_{Ni} (μ_B)	μ_I (μ_B)	E_{gap} (eV)	J (meV)
$U_{eff} = 2$ eV	3.97	1.33	0.23	0.74	6.42
$U_{eff} = 3$ eV	3.97	1.38	0.21	0.95	5.27
$U_{eff} = 4$ eV	3.98	1.44	0.19	1.16	4.30
$U_{eff} = 5$ eV	3.99	1.51	0.17	1.39	3.44
Ref [155]	3.88	2.00	—	—	3.02
Ref [156]	3.92	1.53	—	—	~4.22
Ref [157]	3.983	1.46	—	1.24	3.90

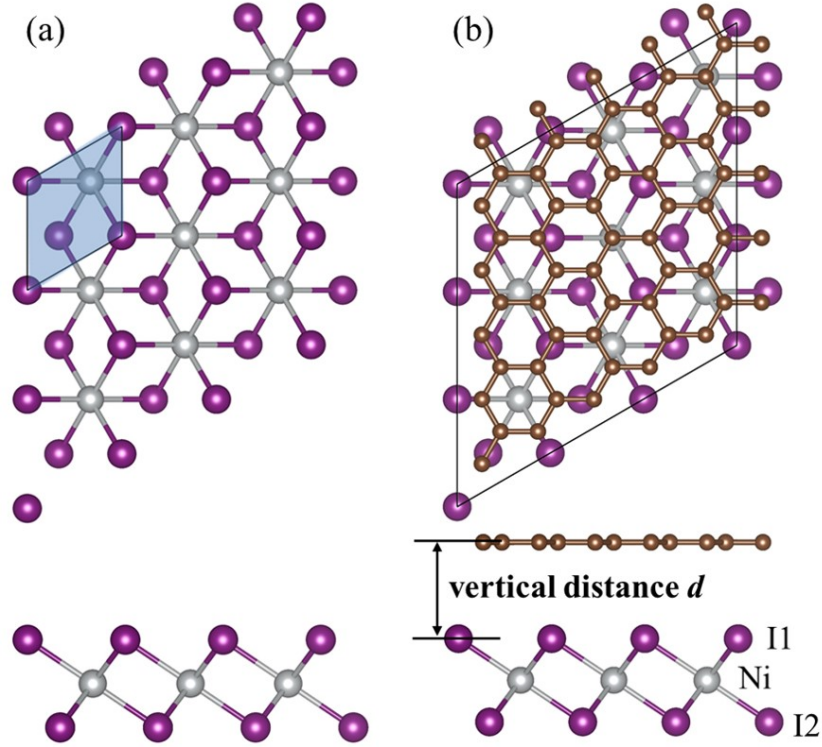


Fig. 3.1 (a) Top view and side view of pristine NiI_2 monolayer. (b) Top view and side view of Gr/NiI_2 heterostructure. Purple, grey and brown balls represent I, Ni and C atoms, respectively. The interfacial I atoms are labeled by I1 and the other side I atoms are labeled by I2.

Here, Gr/NiI_2 heterostructures are constructed by depositing a 5×5 supercell of graphene on a 3×3 supercell NiI_2 substrate with a small lattice mismatch of 2.86%. For these heterostructures, the interfacial I atoms are labeled by I1 and the other side I atoms by I2. We consider three most possible stacking arrangement of Gr/NiI_2 , which are two C atoms in graphene layer coordinates directly atop on (i) two Ni atoms, (ii) two I1 atoms and (iii) two I2 atoms, respectively. We find that the most stable configuration is (i), as shown in Fig. 3.1(b). The average equilibrium interlayer distance is about 3.61 \AA for U_{eff} from 2 to 5 eV, which indicates that the coupling of the heterostructure is a typical van der Waals interaction.

3.3.2 Interlayer spacing controlled magnetic anisotropy

Fig. 3.2 shows the MAE of pristine NiI₂ and Gr/NiI₂ as a function of the interlayer distance decreasing (Δd). Although the pristine MAE of NiI₂ is influenced by U_{eff} , graphene coating and Δd both enhances PMA of NiI₂. Graphene coating slightly enhance the PMA of NiI₂ from 0.071 mJ/m² to 0.102 mJ/m² when $U_{eff} = 3$ eV. If keep decreasing Δd from 0 to -1 Å, the PMA of Gr/NiI₂ is effectively enhanced from 0.102 to 0.730 mJ/m² (red line in Fig. 3.2). The amplitude of this PMA enhancement increasing from 0.405 to 0.767 mJ/m² when U_{eff} decreasing from 5 to 2 eV.

By analyzing the layer-resolved MAE, the orbital-hybridization-resolved MAE, and the DOS, we find that the physical mechanism behind the PMA enhancement is similar for different U_{eff} values. In the following discussion, we choose $U_{eff} = 3$ eV as an example to detailly show how the graphene tunes the PMA of NiI₂. From the layer-resolved MAE (Fig. 3.3), one can see that the PMA of I1 increase when contacted with graphene and keeps increasing with the interlayer distance decreasing, which results in the PMA enhancement of Gr/NiI₂. To further elucidate the mechanism of MAE change, we performed a comparison analysis of MAE from orbital hybridization between I1 in pristine NiI₂ and in Gr/NiI₂ heterostructure as shown in Fig. 3.4(a), (b), (c) and (d). For I1 in pristine NiI₂, the hybridization between p_y and p_x (labeled by 1 with green bar in Fig. 3.4(a)) gives rise an IMA contribution, however the hybridization between p_y and p_z (labeled by 2 with red bar in Fig. 3.4(a)) constitutes a strong PMA. The small amplitude of anisotropy of I1 in NiI₂ arises from the competition of these two hybridizations. When the I1 atom interacts with graphene, the amplitude of MAE from hybridizations 1 and 2 decrease simultaneously but hybridization 1 reduces more strongly (Fig. 3.4(b)), which results the PMA enhancement of I1 in NiI₂. Moreover, when decreasing the interlayer distance, it is found that IMA from hybridization 1 keeps reducing while the PMA from hybridization 2 increases (Fig. 3.4(c) and (d)), giving rise to PMA enhancement in I1 atom.

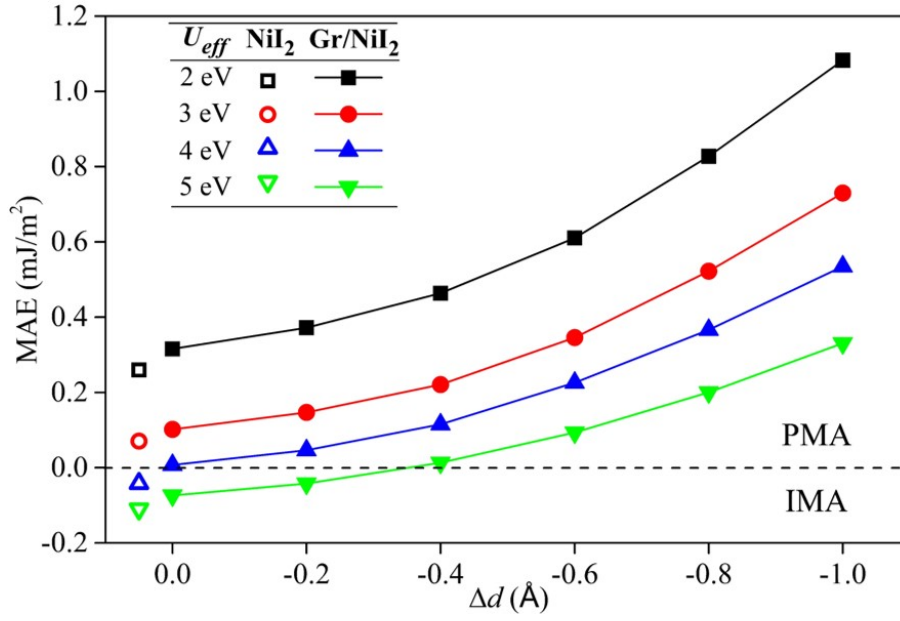


Fig. 3.2 MAE of NiI₂ and Gr/NiI₂ as a function of the interlayer distance decreasing (Δd).

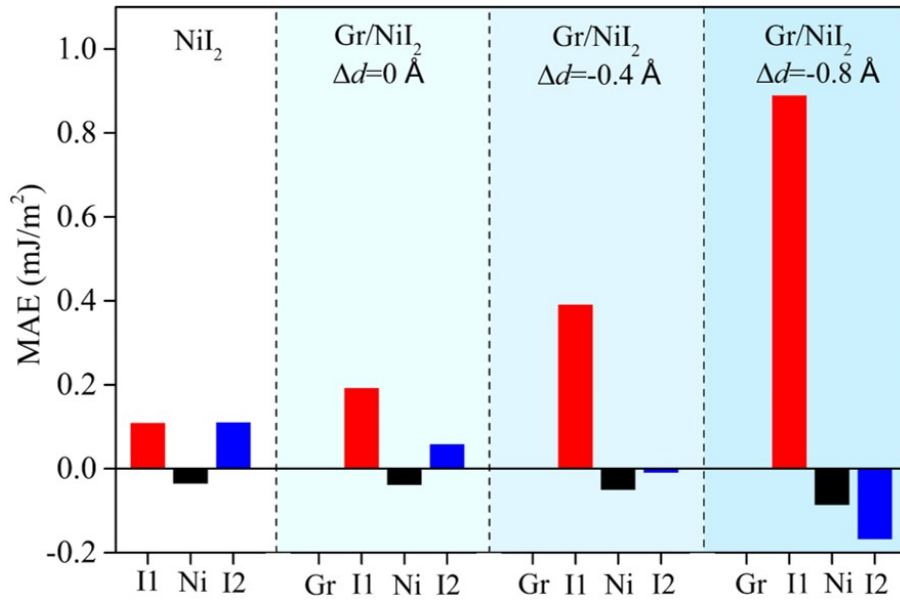


Fig. 3.3 The layer-resolved MAE of NiI₂ and Gr/NiI₂ with $\Delta d = 0, -0.4$ and -0.8 Å.

Next, we investigate how the electronic states of I 5*p* orbitals influence the MAE. According to the second-order perturbation theory [172, 173], MAE can be expressed as:

$$MAE = \xi^2 \sum_{\sigma\sigma'} \sum_{o^\sigma, u^{\sigma'}} \frac{(2\delta_{\sigma\sigma'} - 1)(|\langle o^\sigma | L_z | u^{\sigma'} \rangle|^2 - |\langle o^\sigma | L_x | u^{\sigma'} \rangle|^2)}{E_u^{\sigma'} - E_o^\sigma}. \quad (3.1)$$

Here, $E_u^{\sigma'}$ and E_o^σ are the energy levels corresponding to unoccupied states with spin σ' and occupied states with spin σ , respectively. MAE is determined by the $(E_u^{\sigma'} - E_o^\sigma)$ and the difference of spin-orbital angular momentum matrix element $(2\delta_{\sigma\sigma'} - 1)(|\langle o^\sigma | L_z | u^{\sigma'} \rangle|^2 - |\langle o^\sigma | L_x | u^{\sigma'} \rangle|^2)$ shown in Table II. Due to the symmetry of orbitals, only a few components in Table 3.2 are non-zero. The detailed deduction is given in Ref. 169. Specific values are also closely related with the magnetization orientation. The matrix elements between p_y and p_z , and p_x and p_z can be written as $-\cos\theta^2$ and $\sin\theta^2$ respectively, where θ represents the angle between magnetization orientation and [100] direction. From Eq. 2.1 and Table 3.2, one can see that (i) MAE comes only from hybridization between occupied and unoccupied electronic states via SOC, (ii) the electronic states around Fermi level (E_F) gives rise the dominant contribution to the MAE due to the small $(E_u^{\sigma'} - E_o^\sigma)$ in denominator, (iii) the total MAE also be influenced by the intensity of DOS because it is the integral of all occupied and unoccupied states. In Fig. 3.4(e), (f), (g) and (h), we plot the projected density of states (pDOS) for I1 atoms in pristine NiI₂ and Gr/NiI₂ heterostructures with different Δd . It is found that the occupied electronic states of I1 5p orbitals around E_F are mainly spin-up while the unoccupied electronic states are mainly spin-down. The element between spin-up occupied $p_{y(x)}$ states ($p_{y(x)}^{o+}$) and spin-down unoccupied $p_{x(y)}$ states ($p_{x(y)}^{u-}$) is -1, which is responsible for the negative MAE from hybridization 1 (green bar in Fig. 3.4(a)-(d)). However, the element between spin-up occupied p_z states (p_z^{o+}) and spin-down unoccupied p_y states (p_y^{u-}) in Table 3.2 is 1, which induces the positive MAE contribution from hybridization 2 in I1 atoms (red bar in Fig. 3.4(a)-(d)). Next, we focus on the change of electronic states induced by the presence of graphene and the vertical distance change, Δd . It can be seen from Fig. 3.4(e) and (f) that the peak of p_y^{o+} states near the E_F decrease,

which means the $p_{y(x)}^{o^+}$ states in deeper energy level with larger $(E_u^- - E_o^+)$ give more contribution to MAE. Therefore, the amplitude of IMA from hybridization 1 decrease when NiI₂ contacted with graphene. When compressing the heterostructure, the density of $p_{y(x)}^{o^+}$ states become more delocalized (black and red lines in Fig. 3.4(g) and (h)). Thus, the amplitude of IMA from hybridization 1 keeps reducing. However, the $p_z^{o^+}$ states of I1 move closer to the E_F and becomes more localized (blue lines in Fig. 3.4(g) and (h)), resulting the stronger enhancement of PMA contribution from hybridization 2. In summary, graphene can tune the electronic states of vicinity I1 atoms, resulting the PMA of NiI₂ effectively enhanced.

Table 3.2 The matrix differences between magnetization along z [001] and x [100] in Eq. 3.1. u^- , o^+ and o^- represent unoccupied spin-down states, occupied spin-up and spin-down states respectively.

u^-	o^+			o^-		
	p_y	p_z	p_x	p_y	p_z	p_x
p_y	0	1	-1	0	-1	1
p_z	1	0	0	-1	0	0
p_x	-1	0	0	1	0	0

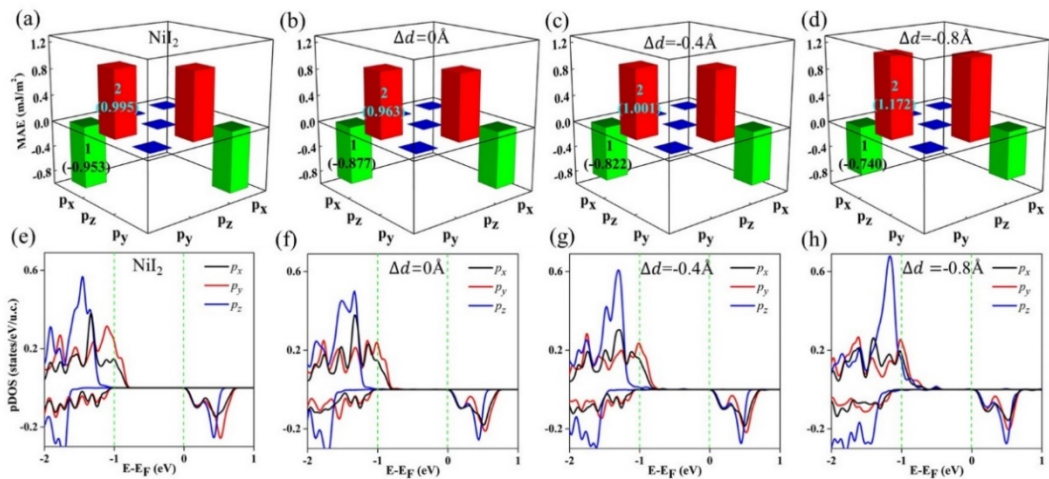


Fig. 3.4 MAE contributions from 5p orbitals hybridization of I1 in (a) prinstine NiI₂, Gr/NiI₂ heterostructure with (b) $\Delta d = 0 \text{ \AA}$, (c) $\Delta d = -0.4 \text{ \AA}$, and (d) $\Delta d = -0.8 \text{ \AA}$. The projected density of states of I1 in (e) prinstine NiI₂, Gr/NiI₂ heterostructure with (f)

$\Delta d = 0 \text{ \AA}$, (g) $\Delta d = -0.4 \text{ \AA}$ and (h) $\Delta d = -0.8 \text{ \AA}$. The green dot lines in (e-h) indicates the energy level at 0 and -1 eV.

3.3.3 QAHE in Gr/NiI₂ heterostructure

The QAHE can be induced in Gr/NiI₂ via decreasing the interlayer distance in the range of U_{eff} from 2 to 5 eV. We find that the physical pictures for different U_{eff} are similar, hence here, we also choose $U_{eff} = 3 \text{ eV}$ as an example to show the electronic states change and topological properties of Gr/NiI₂. Pristine NiI₂ monolayer is a semiconductor with an indirect band gap of 1.18 eV as shown in Fig. 3.5(a). For Gr/NiI₂ heterostructure with the equilibrium interlayer distance, 3.59 \AA , the band structure shows that the system is metallic (Fig. 3.5(b)). We notice that the Dirac cones of the spin-polarized graphene are well preserved but are buried in the conduction band of NiI₂, which indicates that the QAHE cannot be observed in the system. However, it has been proved that the Dirac cones of graphene in van der Waals heterostructures can be effectively tuned by decreasing the interlayer distance. Fig. 3.5(c) plots the spin-polarized band structure when decreasing the interlayer distance 0.7 \AA . We find that the Dirac cones are tuned to lie inside the band gap of NiI₂. Moreover, the decreasing of interlayer distance enhances proximity effect significantly, which induces a large exchange splitting (about 87 meV) in graphene (Fig. 3.5(d)). To elucidate the mechanism responsible for the shift of Dirac cones, the transferred charge between graphene and NiI₂ layer is analyzed as shown in Fig. 3.6. When contact with NiI₂, graphene layer donates electrons to NiI₂ layer since W_{Gr} (4.21 eV) is smaller than χ_{NiI_2} (4.72 eV). Therefore, the Dirac cones of graphene are shifted above the E_F in Gr/NiI₂ (Fig. 3.6 left inset). As decreasing the interlayer distance, the transferred electrons from graphene to NiI₂ begin to decrease gradually, and when $\Delta d < -0.55 \text{ \AA}$, the electrons flow from NiI₂ to graphene. Thus, the Dirac cones of graphene shifted back to the E_F (Fig. 3.6 right inset).

Finally, we focus on the topological properties of Gr/NiI₂ heterostructure with $\Delta d = -0.7 \text{ \AA}$. When SOC is included, a small band gap opens at the crossing point of

two bands with opposite spin orientation and the E_F is right inside the SOC-induced band gap as shown in Fig. 3.7(a) and (b). Due to different sublattice A and B of graphene, the SOC-induced band gap around K (4.42 meV) and K' (2.19 meV) are not equal. To elucidate the mechanism of the band gap opening induced by SOC, we adopt the low-energy effective model of graphene [154]:

$$H(k) = -v_f(\eta\sigma_x k_x + \sigma_y k_y)\mathbf{I}_s + M\mathbf{I}_\sigma S_z + \frac{\lambda_R}{2}(\eta\sigma_x S_y - \sigma_y S_x) + U\sigma_z \mathbf{I}_s \quad (3.2)$$

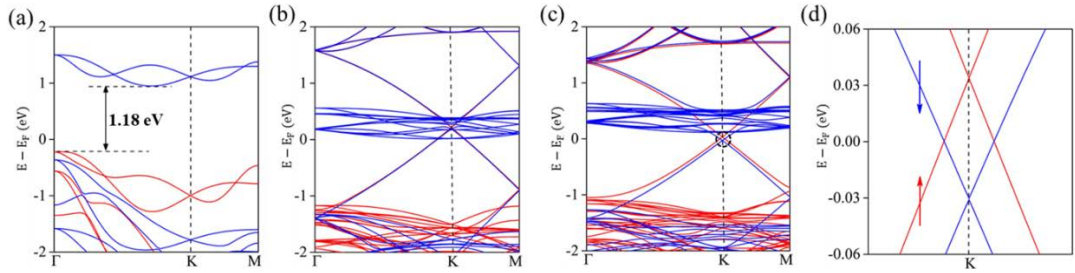


Fig. 3.5 The band structure of (a) pristine NiI_2 , (b) Gr/NiI_2 with $\Delta d = 0 \text{ \AA}$ and (c) $\Delta d = -0.7 \text{ \AA}$. (d) Zoom in the black dashed circle of panel (c). Red and blue lines presents the spin-up and spin-down bands, respectively.

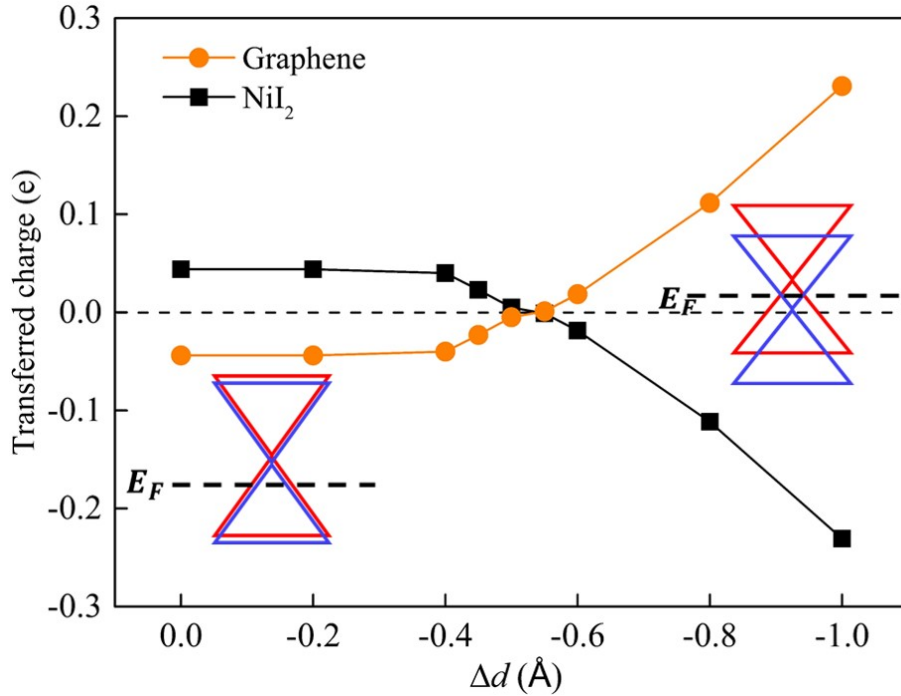


Fig. 3.6 The transferred charge between graphene and NiI_2 layer as a function of the interlayer distance decreasing (Δd). The positive (negative) value of transferred

charge represents the electron accumulation (depletion). Insets: The schematic of energy levels nearby E_F for Gr/NiI₂.

where the v_f is the fermi velocity, $\eta = \pm 1$ for K and K' respectively. σ and s are Pauli matrices which act on sublattices and spin respectively. In Eq. 2.2, the first term is the Hamiltonian of pristine graphene, the second term is magnetic exchange field, the third term is Rashba SOC and the last term represents staggered sublattice potential. For pure graphene, there are linear Dirac bands at both K and K' points. When decreasing the interlayer distance between graphene and NiI₂, a large magnetic exchange field is induced, which makes spin-up and spin-down Dirac bands cross each other. When the Rashba SOC is included, the band gaps open at the crossing points of Dirac bands with opposite spin orientations at both K and K' points. By fitting the band structures with DFT calculations as shown in Fig. 3.7 (c) and (d), the parameters for K and K' in low-energy effective model can be obtained. For K point, $v_f \approx 2.5$ eV, $M \approx 40.0$ meV, $\lambda_R \approx 4.0$ meV and $U \approx 0$ meV, and for K' point, $v_f \approx 2.5$ eV, $M \approx 41.5$ meV, $\lambda_R \approx 2.0$ meV and $U \approx 0$ meV. To determine the existence of QAHE in compressed Gr/NiI₂, we integrate the Berry curvature $\Omega(\mathbf{k})$ over the first Brillouin zone by [174]

$$\Omega(\mathbf{k}) = -\sum_n f_n \sum_{n' \neq n} 2\text{Im} \frac{\langle \psi_{n\mathbf{k}} | v_x | \psi_{n'\mathbf{k}} \rangle \langle \psi_{n'\mathbf{k}} | v_y | \psi_{n\mathbf{k}} \rangle}{(E_{n'} - E_n)^2} \quad (3.3)$$

where f_n is the Fermi-Dirac distribution function, $v_{x(y)}$ are the velocity operators and E_n is the eigenvalue of the $\psi_{n\mathbf{k}}$. From Figs. 3.7(c) and (d), one can see that the calculated Berry curvatures have the same sign around K and K' points. By integrating the Berry curvatures over the Brillouin zone, we obtain the Chern number $C = -2$, which confirms the QAHE existence in compressed Gr/NiI₂. Moreover, the intrinsic hall conductivity is determined by the Berry curvatures [175], as:

$$\sigma = \frac{e^2}{h} \frac{1}{2\pi} \int_{BZ} d\mathbf{k}^2 \Omega(\mathbf{k}) \quad (3.4)$$

where e is the elementary charge and h is the Planck constant. With the parameters obtained from fitting low-energy effective model to DFT results, the anomalous Hall

conductivity σ_{xy} is obtained as shown in Fig. 3.8. As expected, σ_{xy} is quantized ($2e^2/h$) when the Fermi level is in band gap of the system. As Fermi level moving away from band gap, the σ_{xy} rapidly reaches to zero. Notably, the exchange field and Rashba SOC can be induced simultaneously by the proximity of the NiI₂ substrate and will be enhanced if interlayer distance decreasing. As an example, we show that for $\Delta d = -1.1 \text{ \AA}$, the magnetic exchange splitting is enlarged to 253 meV and global band gap of the system is increased to 4.82 meV.

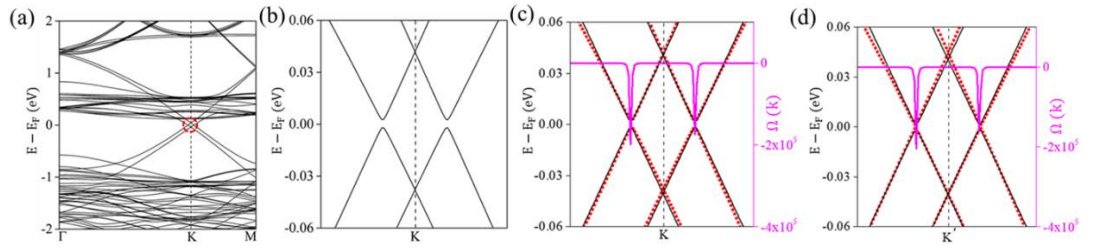


Fig. 3.7 (a) The band structure of Gr/NiI₂ with $\Delta d = -0.7 \text{ \AA}$ when SOC is included. (b) Zoom in the red dashed circle of panel (a). (c) The black lines and red dots represent band structure obtained from the low-energy effective model and DFT calculations respectively. The purple lines represent the calculated Berry curvature. (d) The same as (c), except around the K' point.

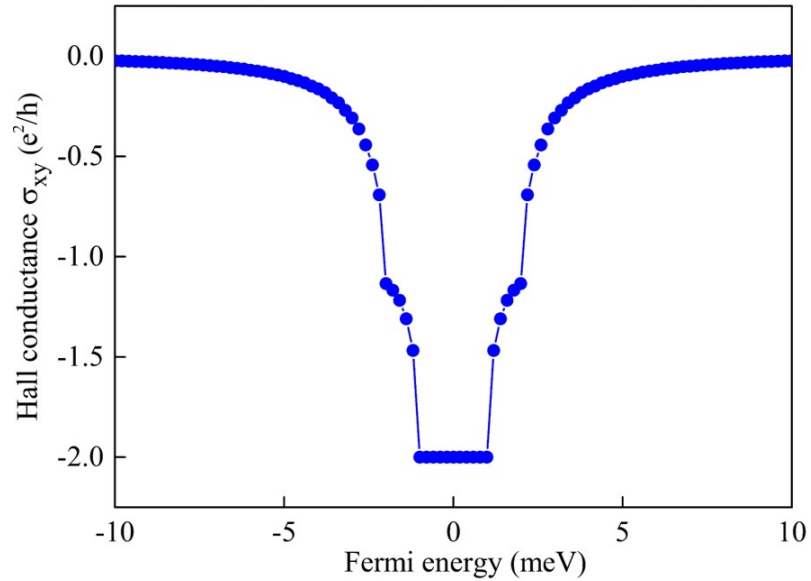


FIG. 3.8 Anomalous Hall conductance as a function of Fermi level calculated from the low-energy effective model.

3.4 Summary

In this chapter, we systematically investigate the magnetic anisotropy and topological properties of Gr/NiI₂ heterostructures. We find that PMA of NiI₂ can be effectively enhanced thanks to the graphene proximity. This PMA enhancement is caused by competition between MAE arising from p_y, p_x hybridization and p_y, p_z hybridization in I1 atoms. Furthermore, by second-order perturbation theory, we elucidate that the MAE arising from hybridization is originated from the electronic states of I1 atoms. Moreover, by decreasing the interlayer distance, the Dirac cones of graphene can be shifted into the band gap of NiI₂, which together with an enhanced Rashba SOC, can lead to QAHE. Our findings demonstrate the enhancement of PMA in NiI₂ by tuning the vdW interlayer distance, which provides a novel approach for controlling the magnetic anisotropy of 2D FM semiconductor, and reveal a possible van der Waals system to realize QAHE.

Chapter 4 Spin-valley coupling in VSi_2N_4 monolayer

4.1 Introduction

The valley, which indicates the maximum of valence bands or minimum of conduction bands, is a new degree of freedom of carriers besides the charge and spin. The valley degree of freedom can be used to encode, store and transmit information, and due to large valley separation in reciprocal space, the valley index is robust against the scatterings of smooth deformations and phonons [65-70]. Therefore, materials with valley characters are very promising in the next-generation electronic devices with high-storage density and low-energy consumption. Because of the inversion symmetry breaking (ISB) of structures and strong SOC from d orbitals in transition metal atoms, 2H-phase Transition-metal dichalcogenides (2H-TMDCs), such as MoS_2 , MoSe_2 , WS_2 and WSe_2 monolayers, have been demonstrated to be able to harbor valley physics, and some interesting phenomena including valley Hall effect, valley polarization, and the control of valley pseudospin have been realized in these systems [71-73, 176-179]. The key for developing the practical valleytronic devices is inducing the large valley polarization. The optical pumping with circularly polarized light can realize the valley polarization, but optical pumping is a dynamic process and require complicated equipment, which is inconvenient for practical devices. Another approach is using magnetism to break valley degeneracy since the valley are directly coupled with spin. However, the valley polarization induced by an external magnetic field is very small, about 0.1 meV/T; magnetic dopants tend to form clusters limiting the quality of the systems; and for magnetic proximity effects, the substrate usually deforms electronic states of the host, and the interlayer interaction is easily influenced by inevitable surface defects. For overcoming above shortages, materials are naturally required to process intrinsic long-range

ferromagnetism or antiferromagnetism, miniaturization, and valley characters simultaneously.

Recently, MoSi_2N_4 and WSi_2N_4 , which are a new type of two-dimensional (2D) layered materials, were synthesized by chemical vapor deposition (CVD) method; moreover, it has been theoretically reported that VSi_2N_4 monolayer is a half-metallic ferromagnet and possess the same crystal structure with MoSi_2N_4 and WSi_2N_4 [180]. In this chapter, we unveil that VSi_2N_4 monolayer is a ferromagnetic (FM) semiconductor with valley properties. By tuning the magnetization orientation from in-plane (IP) to out-of-plane (OOP), a large valley polarization of 63.11 meV can be achieved. Furthermore, we obtain a formula of energy splitting under SOC and adopt a tight-binding model, which elucidates the physical picture of spin-valley coupling in VSi_2N_4 . The valley polarization and opposite Berry curvatures at $-K$ and $+K$ result in the AVHE in VSi_2N_4 when magnetization orientation is OOP. More interestingly, under 4% tensile strain, the VSi_2N_4 monolayer can be tuned to a “ferrovalley” material with a spontaneous valley polarization of 71.71 meV. These results demonstrate that VSi_2N_4 monolayer can be a good candidate for spintronic and valleytronic applications.

4.2 Methodology

The first-principles calculations within density functional theory (DFT) are implemented in the Vienna *ab initio* simulation package (VASP). The exchange-correlation interaction is treated by the generalized gradient approximation (GGA) based on the Perdew-Burke-Ernzerhof (PBE) function. The cutoff energies for expanding plane wave basis are 520 eV, and the convergence criteria of electronic iteration is set to 10^{-7} eV. All structures are relaxed until Hellmann-Feynman force on each atom is less than $0.001 \text{ eV}/\text{\AA}$. To describe strongly correlated $3d$ electrons of V [181], the GGA+U method is applied ($U_{eff} = 3 \text{ eV}$). Moreover, we compare band structures of VSi_2N_4 obtained from GGA+U with that from the hybrid functional HSE06 [182], since the later usually gives more accurate electronic states. The

Brillouin zone is sampled using $17 \times 17 \times 1$ and $13 \times 13 \times 1$ Γ -center \mathbf{k} -point grids for GGA+U and HSE06, respectively. The phonon dispersions are calculated by PHONOPY code [183] with a $4 \times 4 \times 1$ supercell. The maximally-localized Wannier functions (MLWFs) calculated by the WANNIER90 package [184] are applied for obtaining the Berry curvature and anomalous hall conductivity.

4.3 Results and discussion

4.3.1 Structural and magnetic properties of VSi_2N_4

The crystal structure of VSi_2N_4 monolayer is shown in Fig. 4.1(a). VSi_2N_4 consists of septuple layers of N-Si-N-V-N-Si-N, with atoms in each layer forming a 2D hexagonal lattice. The central V atom is coordinated by six neighboring N atoms in a trigonal prismatic geometry, and then this VN_2 layer is sandwiched by two Si-N bilayers. The optimized lattice constant is 2.88 Å which is consistent with the previous theoretical result [180]. The crystal symmetry of VSi_2N_4 is D_{3h} , and the inversion symmetry is broken like 2H-TMDCs. We also find that the VSi_2N_4 has different formula and structure compared with MXene. The later has specific formula $M_{n+1}X_nT_x$, where M (early transition metal) layers are interleaved by X (carbon/nitrogen) layers, and the surface is terminated by T (oxygen/hydroxyl/fluorine) [185, 186]. Furthermore, we calculate the electron localization function [see Fig. 4.1(b)] to elucidate bonding types in VSi_2N_4 . For the nearest-neighboring (NN) V and N atoms, electrons are mainly localized around N, which indicates an ionic bonding; and highly localized electrons between the NN Si and N atoms suggests that there is a covalent bonding between them. The phonon spectrums [see Fig. 4.1(c)] demonstrate that VSi_2N_4 is dynamically stable.

Next, we focus on the magnetic properties of VSi_2N_4 . According to Goodenough-Kanamori-Anderson rules [187-189], the super-exchange coupling between two V atoms through intervening N atom is FM since the bonding angle of V-N-V (90.26°) is very close to 90.00° . By comparing the energy difference of FM and AFM states of a $2 \times 1 \times 1$ supercell, we confirm that the NN exchange coupling J

of two V is FM with magnitude of 29.70 meV. To determine the MAE of VSi_2N_4 , we calculate the energy difference between different spin directions of V atoms when SOC effect is considered. Here, we choose the energy when the magnetization orientation is parallel to the positive x-axis (+x) as a reference, and the corresponding coordinate is shown in Fig. 4.1(a). It can be seen in Fig. 4.1(d) that VSi_2N_4 has an easy magnetization plane, i.e., there is no energy consumption when magnetization rotates in the plane of 2D layer. The coexistence of local magnetic moments ($1.2 \mu_B$ in V-3d orbitals) and easy magnetization plane indicates that VSi_2N_4 belongs to the family of 2D XY magnets. For a 2D XY magnet, the magnetic order can be stabilized under a finite-size limit, and the Berezinsky-Kosterlitz-Thouless transition [190] could occur at a critical temperature (T_{BKT}) which can be estimated as $T_{BKT} = 0.89J/k_B$ [191, 192], where the k_B is the Boltzmann constant. With $J = 29.70$ meV, we obtain that the T_{BKT} for VSi_2N_4 is around 307 K, which is over room temperature.

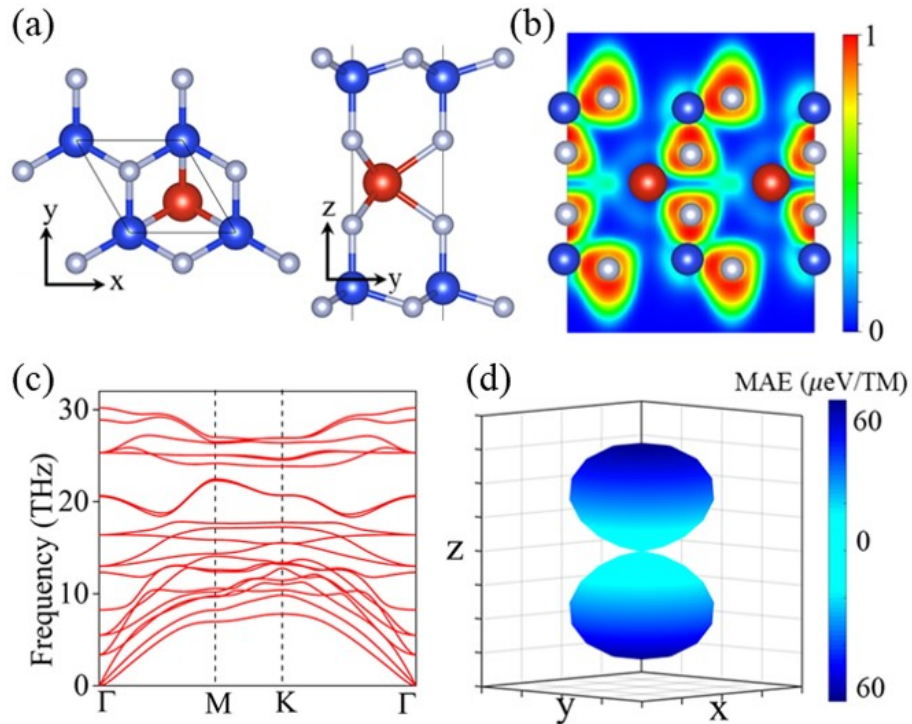


Fig. 4.1 (a) The top and side views of the crystal structure, (b) electron localization function, (c) phonon dispersions and (d) magnetic anisotropy of VSi_2N_4 monolayer. In (a) and (b), the red, grey and blue balls represent V, N and Si elements, respectively.

4.3.2 Spin-valley coupling

For obtaining the accurate electronic states, we test the influence of U_{eff} on band structures of VSi_2N_4 monolayer as shown in Fig. 4.2. One can see that the VSi_2N_4 is half-metallic when $U_{eff} = 0$ eV, and as U_{eff} increasing, VSi_2N_4 becomes to an indirect bandgap semiconductor with appearing valleys at $-K$ and $+K$ points. When U_{eff} increases to 3 eV, VSi_2N_4 becomes a direct bandgap semiconductor [see $U_{eff} = 3$ eV of Fig. 4.2], and the valence band maximum (VBM) and conduction band minimum (CBM) consisting of electrons with same spin just locates at $-K$ and $+K$ points, which is very consistent with the band structure obtained from HSE06. These results indicate that the VSi_2N_4 is a material with valley properties.

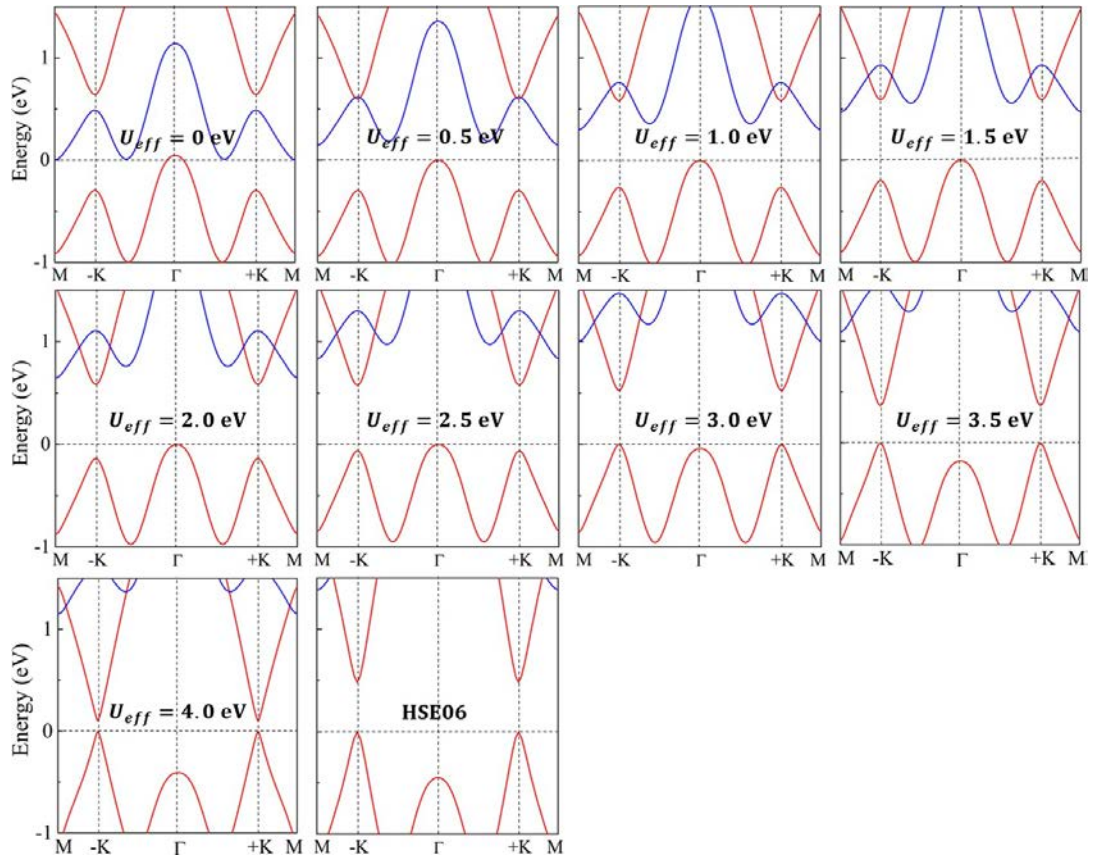


Fig. 4.2 Spin-polarized band structures of VSi_2N_4 obtained from GGA+U (U_{eff} varies from 0 to 4 eV) and HSE06 without considering SOC effects. The red (blue) represents spin-up (spin-down).

Notably, the bandgap is continuously decreasing when the U_{eff} (the correlation strength of $3d$ electrons of V) keeps increasing, which implies that valley-polarized QAHE, arising from band inversion of VBM and CBM at $-K/+K$ point, is hopefully realized in this system by artificially setting appropriate U_{eff} [193]. The correlation effects of $3d$ electrons of V becomes stronger when the U_{eff} increases, thus resulting in that the $3d$ orbital splitting in octahedral crystal field decreases. In the following discussion, we choose $U_{eff} = 3$ eV to show in detail how spin and valley are coupled with each other. Since the magnetic anisotropy of VSi_2N_4 is IP, we calculate the band structure when SOC is included with the magnetization along $+x$, as shown in Fig. 4.3(a). One can see that the valley degeneracy is still preserved. By overcoming an energy barrier of $63.99 \mu\text{eV}$, the magnetization orientation can be tuned from IP to OOP, and a relatively large valley polarization of 63.11 meV is induced [see Fig. 4.3(b)]. The valley polarization is quantitatively defined as the energy difference between VBM at $-K$ and $+K$, $\Delta E = E_{VBM,+K} - E_{VBM,-K}$. One can see that this valley polarization only appears at valence bands while it is degenerate at conduction bands. Notably, these results yield good comparison with the band structures obtained from HSE06+SOC as illustrated in Fig. 4.4, and an even larger polarization of 93.51 meV is achieved via HSE06+SOC calculations. In Fig. 4.3(c), we show the valley polarization as a function of magnetization orientation. The value of valley polarization varies from 63.11 to -63.11 meV continuously when the magnetization rotates from $+z$ to $-z$.

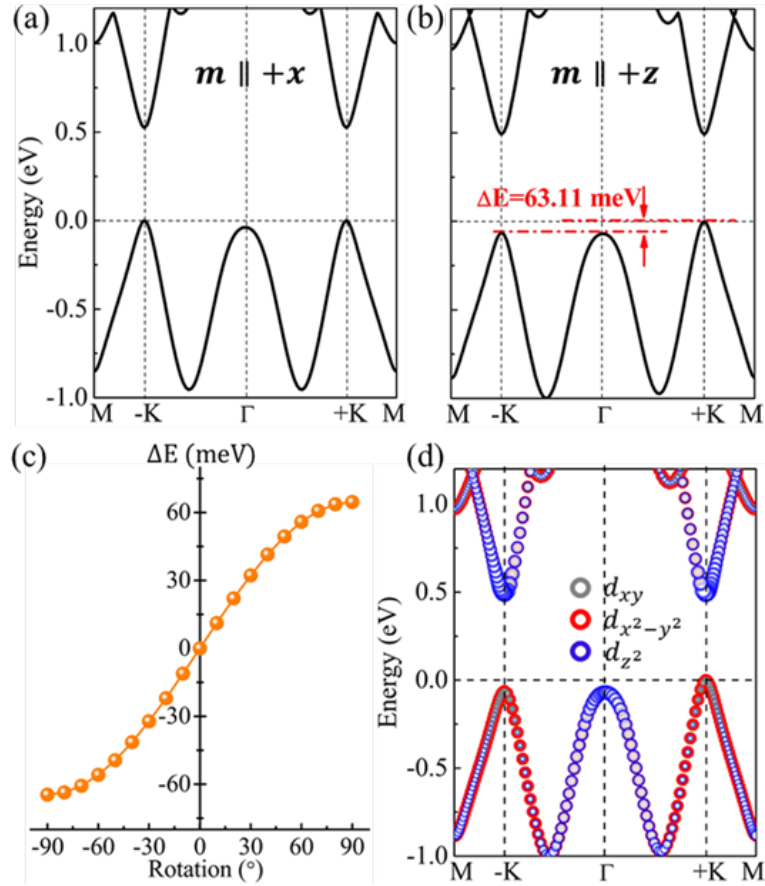


Fig. 4.3 The band structure of VSi₂N₄ monolayer with SOC when the magnetization along (a) +x and (b) +z. (c) The valley polarization ΔE as a function of magnetization orientation. The magnetization rotates from $-z$ to $+z$. (d) The orbital-resolved band structure of VSi₂N₄ monolayer with SOC when the magnetization along +z.

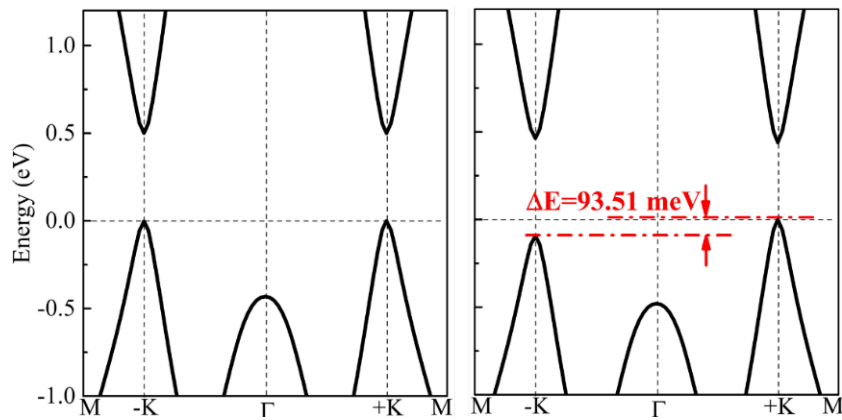


Fig. 4.4 Band structures of VSi₂N₄ obtained from HSE06+SOC with the magnetization along +x (left panel) and +z (right panel).

Next, we derive the formula for describing the quantitative relationship between magnetization orientation and valley polarization. Since the VBM and CBM of VSi_2N_4 are both occupied by electrons with identical spin, we can ignore the interaction between spin-up and spin-down states. The SOC Hamiltonian can be written as [194, 195]:

$$\hat{H}_{\text{SOC}} \approx \hat{H}_{\text{SOC}}^0 = \lambda \hat{S}_{z'} (\hat{L}_z \cos\theta + \frac{1}{2} \hat{L}_+ e^{-i\phi} \sin\theta + \frac{1}{2} \hat{L}_- e^{+i\phi} \sin\theta) \quad (4.1)$$

where \hat{L} and \hat{S} represents the operator of orbital angular momentum and spin angular momentum, and (x, y, z) and (x', y', z') are the coordinate systems for \hat{L} and \hat{S} , respectively. $\hat{L}_+ = \hat{L}_x + i\hat{L}_y$, and $\hat{L}_- = \hat{L}_x - i\hat{L}_y$. θ and ϕ are polar angles which define the spin orientation as shown in Fig. 4.5. The VBM and CBM are dominated by d_{xy} , $d_{x^2-y^2}$ and d_{z^2} orbitals of V atoms, respectively [see Fig. 4.3(d)]. The group symmetry of $-K$ and $+K$ points is C_{3h} . Accordingly, the basis functions are chosen as $|\psi_c\rangle = |d_{z^2}\rangle$ and $|\psi_v^\tau\rangle = \sqrt{\frac{1}{2}}(|d_{x^2-y^2}\rangle + i\tau|d_{xy}\rangle)$, where $\tau = \pm 1$ represents the valley index. The energy levels for valleys at valence and conduction bands can be defined as $E_v^\tau = \langle \psi_v^\tau | \hat{H}_{\text{SOC}}^0 | \psi_v^\tau \rangle$ and $E_c = \langle \psi_c | \hat{H}_{\text{SOC}}^0 | \psi_c \rangle$, respectively. Consequently, the energy difference between valleys at $-K$ and $+K$ points is given by:

$$E_v^+ - E_v^- = i \langle d_{x^2-y^2} | \hat{H}_{\text{SOC}}^0 | d_{xy} \rangle - i \langle d_{xy} | \hat{H}_{\text{SOC}}^0 | d_{x^2-y^2} \rangle. \quad (4.2a)$$

$$E_c^+ - E_c^- = 0. \quad (4.2b)$$

Obviously, when SOC effect is considered, the valley degeneracy at valence bands is broken while it still keeps degenerate for conduction bands, which is consistent with the calculated band structure of VSi_2N_4 . The basis functions $|d_{x^2-y^2}\rangle$ and $|d_{xy}\rangle$ has the form:

$$|d_{x^2-y^2}\rangle = \frac{1}{\sqrt{2}}(|d_{+2}\rangle + |d_{-2}\rangle) \quad (4.3a)$$

$$|d_{xy}\rangle = \frac{1}{\sqrt{2}}[-i(|d_{+2}\rangle - |d_{-2}\rangle)] \quad (4.3b)$$

which results in $\hat{H}_{soc}^0 |d_{xy}\rangle \propto -2i\cos\theta |d_{x^2-y^2}\rangle + \frac{isin\theta}{\sqrt{2}} (e^{-i\phi} |d_{-1}\rangle - e^{+i\phi} |d_{+1}\rangle)$ and $\hat{H}_{soc}^0 |d_{x^2-y^2}\rangle \propto 2i\cos\theta |d_{xy}\rangle + \frac{sin\theta}{\sqrt{2}} (e^{-i\phi} |d_{-1}\rangle + e^{+i\phi} |d_{+1}\rangle)$. Inserting this relationship to Eq. (3.2a), we obtain $E_v^+ - E_v^- \propto 4\cos\theta$ which means that the valley splitting will gradually disappear when spin rotates from OOP to IP. This result is just responsible for the variation of valley splitting as magnetization rotating which is obtained from first-principles calculations [see Fig. 4.3(c)]. Notably, the similar behavior of valley polarization has also been reported in the Mn/WS₂ [98] and Nb₃I₈ monolayer [195]

In addition, we construct an effective Hamiltonian for VSi₂N₄ as the spin orientation along OOP:

$$H(k) = I_s \otimes \left[v_f (\tau \sigma_x k_x + \sigma_y k_y) + \frac{\Delta}{2} \sigma_z \right] + \tau S_z (\lambda_u \sigma_+ + \lambda_l \sigma_-) - S_z (B_u \sigma_+ + B_l \sigma_-) \quad (4.4)$$

where the v_f is the Fermi velocity, Δ is the gap and λ_u (λ_l) is the SOC parameter for the upper (lower) band. B_u (B_l) is the effective exchange splitting for the upper (lower) band, which originates from the intrinsic ferromagnetism of V atoms. In this model, we choose upper (lower) band instead of the valence (conduction) band. The S_α and σ_α ($\alpha = x, y, z$) represent Pauli matrices for real spin and valley pseudospin, respectively. σ_\pm is defined as $\frac{1}{2}(\sigma_0 \pm \sigma_z)$. As shown in Fig. 4.6, the band structures obtained from the model agrees with DFT results very well, with the fitting parameters in units of eV: $v_f = 2.15$, $\Delta = 0.64$, $\lambda_u = -0.0026$, $\lambda_l = 0.042$, $B_u = 1.49$, and $B_l = 0.73$. One can see that the value of effective exchange splitting B_u (B_l) is large, reflecting the strong internal ferromagnetic field of VSi₂N₄ which splits the spin-down and spin-up states. The combination of intrinsic FM coupling and SOC effect of localized 3d electrons of V generates the valley polarization in VSi₂N₄ when the magnetization is OOP.

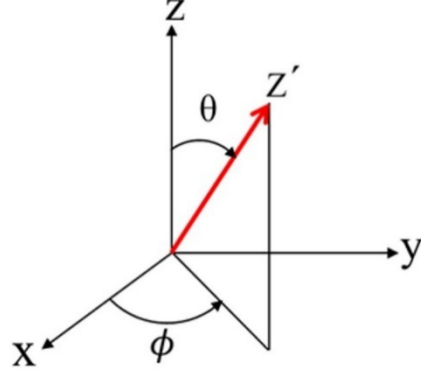


Fig. 4.5 The (x, y, z) coordinate is used for describing the orbital, and polar angles θ and ϕ defines the orientation of spin.

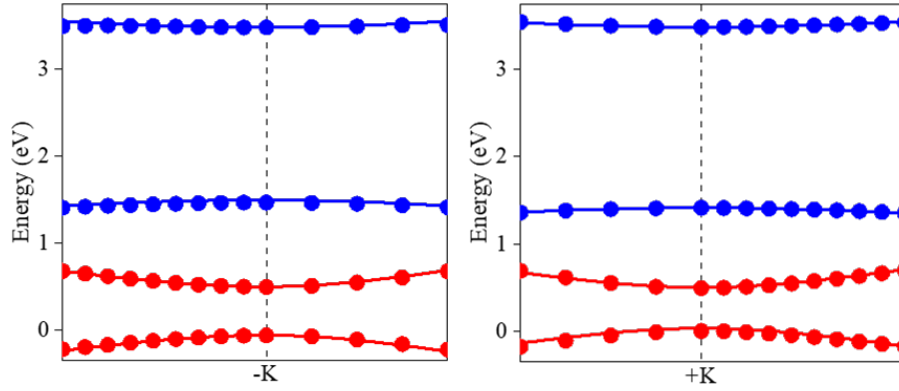


Fig. 4.6 Comparison between the band structures calculated from DFT results (dots) and low-energy effective model (lines). The red (blue) color represents spin-up (spin-down).

The valley polarization can give rise to AVHE in VSi_2N_4 . To demonstrate this, we calculate the Berry curvature of VSi_2N_4 based on Eq 3.3. Figs. 4.7(a) and (b) show the calculated Berry curvatures as a contour map in the whole 2D Brillouin zone and as a curve along high-symmetry path. The Berry curvatures have opposite signs and different absolute values at $-K$ and $+K$ points while it closes to zero at other points in reciprocal space. Under an IP electrical field, the electrons or holes will acquire an anomalous velocity $v \sim \mathbf{E} \times \boldsymbol{\Omega}(\mathbf{k})$. For VSi_2N_4 , by shifting the Fermi level (E_F) between $-K$ and $+K$ valleys in valence bands, the spin-up holes from $+K$ valley move to one side of sample under an IP electrical field [see left panel in Fig. 4.7(d)],

resulting in the net Hall current. Based on the Eq 3.4, we calculated the anomalous Hall conductivity σ_{xy} . As shown in the shadow area of Fig. 4.7(c), valley-polarized σ_{xy} is achieved when the E_F falls between the VBM of $-K$ and $+K$ valleys, confirming the existence of AVHE. Moreover, by the excitation of linearly polarized light with frequency satisfying $\Delta_{+K}/\hbar \leq \omega \leq \Delta_{-K}/\hbar$, the spin-up electrons and spin-down holes from $+K$ valley will be generated and accumulate on the opposite boundary of sample under an IP electrical field as shown in right panel of Fig. 4.7(d). Here, the Δ_{+K} and Δ_{-K} represent the band gaps of $+K$ and $-K$ valleys respectively.

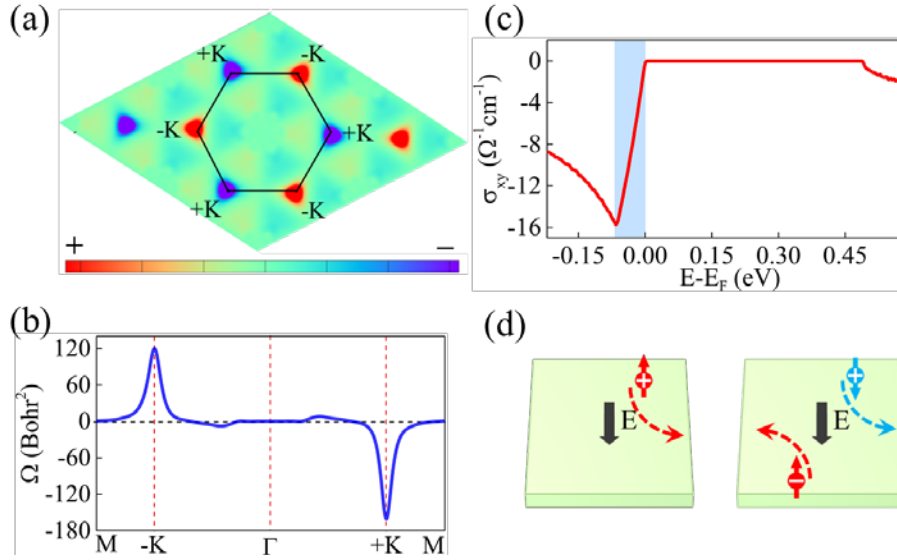


Fig. 4.7 For the VSi_2N_4 monolayer: The distributions of Berry curvature (a) in the whole Brillouin zone and (b) along the high-symmetry points. (c) The anomalous hall conductivity as a function of E_F . (d) The schematics of the anomalous valley Hall effect under hole doping (left panel) and light-irradiation (right panel). The magnetization is along $+z$. The electrons and holes in valley $+K$ are denoted by white ‘-’, ‘+’ in the dark circles, and the red and blue arrows represent spin-up and spin-down states.

4.3.3 Strain-tunable valley properties

To obtain valley polarization in VSi_2N_4 , the spin orientation is required to be OOP. However, the magnetic anisotropy of pristine VSi_2N_4 is IP. We already know

that MAE is normally dominated by electronic states nearby the E_F and the elements with relatively strong SOC [196, 197]. Therefore, the d_{xy} , $d_{x^2-y^2}$ and d_{z^2} orbitals of V atoms possibly play crucial roles in determining MAE of VSi_2N_4 . Since d_{xy} and $d_{x^2-y^2}$ are both IP orbitals, the MAE of VSi_2N_4 will be effectively tuned by biaxial strain as indicated by the blue line in Fig. 4(a). Notably, the magnetic anisotropy of VSi_2N_4 is tuned from IP to OOP when tensile strain reaches to 4%. Moreover, as strain is in the range of 4% - 8%, valley properties are still preserved as shown in Fig. 4.9. Due to the PMA, the spontaneous valley polarization around 70 meV [see the orange line in Fig. 4.8(a)] has been generated in VSi_2N_4 under strain. Next, we choose the VSi_2N_4 under 6% strain as an example to exhibit valley-dependent transport properties. Fig. 4.10 shows the band structures when SOC effect is considered, and one can see that the valley polarization appears at CBM resulting from the occupation of d_{xy} and $d_{x^2-y^2}$ states according to previous model analysis. Similar to the pristine VSi_2N_4 , Berry curvatures have the opposite signs and different absolute values at $-K$ and $+K$ points as shown in Figs. 4.8(b) and (c). When the E_F is shifted between $-K$ and $+K$ valleys in conduction bands, spin-up electrons from $-K$ valley will acquire the anomalous velocity ($v \sim \mathbf{E} \times \boldsymbol{\Omega}(\mathbf{k})$) and accumulate at one boundary of sample under an IP electrical field as illustrated in the left panel

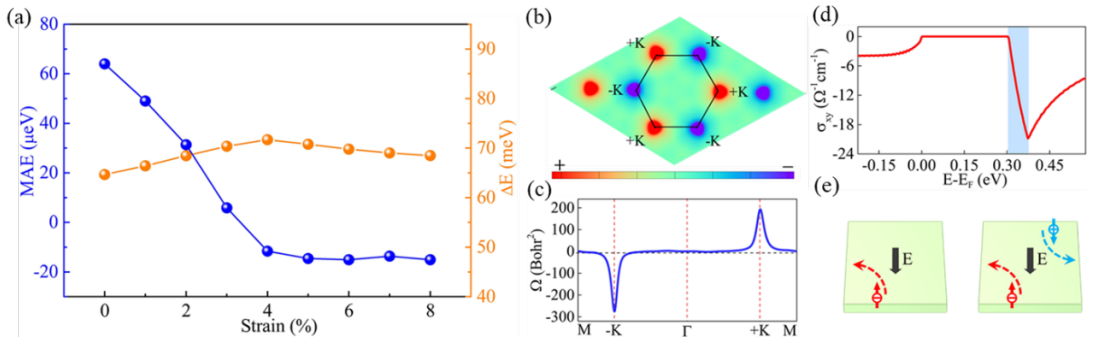


Fig. 4.8 (a) The magnetic anisotropy (blue line) and valley polarization (orange line) as functions of strain. For the VSi_2N_4 monolayer under 6% tensile strain: The distributions of Berry curvature (b) in the whole Brillouin zone and (c) along the high-

symmetry points. (d) The anomalous hall conductivity as a function of E_F . (e) The schematics of the anomalous valley Hall effect under electron doping (left panel) and light-irradiation (right panel). The magnetization is along $+z$. The electrons and holes in valley $-K$ are denoted by dark ‘-’, ‘+’ in the hollow circles, and the red and blue arrows represent spin-up and spin-down states.

of Fig. 4.8(e). Naturally, the valley-polarized σ_{xy} is generated [see the shadow area of Fig. 4.8(d)], which demonstrates the existence of AVHE in VSi_2N_4 under strain. The spin-up electrons and spin-down holes from $-K$ valley can also be excited by the linearly polarized light of the frequency satisfying $\Delta_{-K}/\hbar \leq \omega \leq \Delta_{+K}/\hbar$ and move to the opposite sides of sample under an IP electrical field as shown in the right panel of Fig. 4.8(e). Notably, the size of bandgap is not only sensitive to U_{eff} but also to tensile strain [see Fig. 4.9]. When the tensile strain increases from 1% to 4%, the bandgap is tuned from 364 to 26 meV. Unexpectedly, the size of bandgap is enhanced as strain keeps increasing from 4% to 8%. This variation implies that valley-polarized QAHE, arising from band inversion of VBM and CBM at $-K/+K$ point, can also be achieved in this system by applying appropriate strain [198].

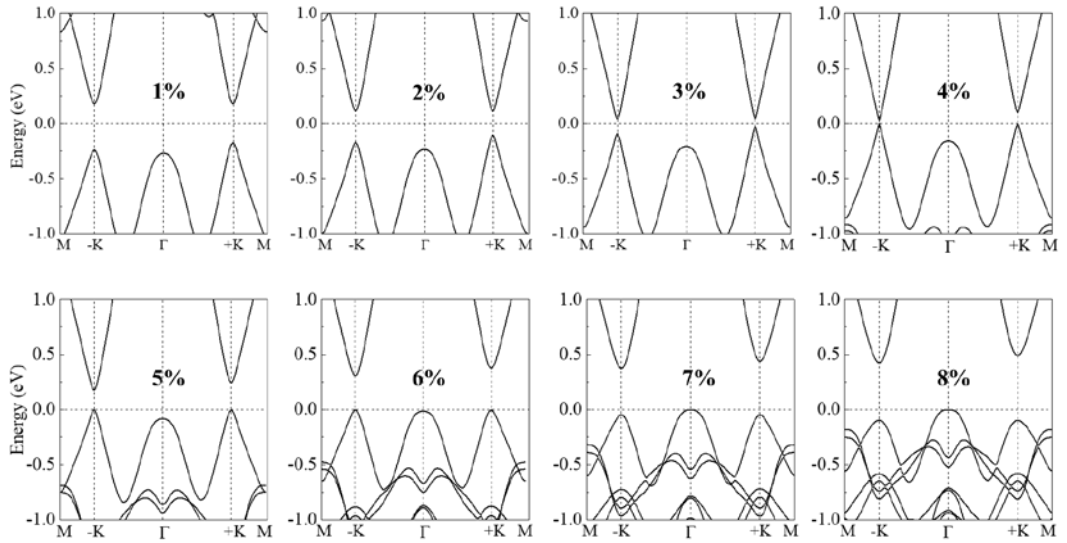


Fig. 4.9 Band structures of VSi_2N_4 under the 1%-8% tensile strains with considering SOC effect.

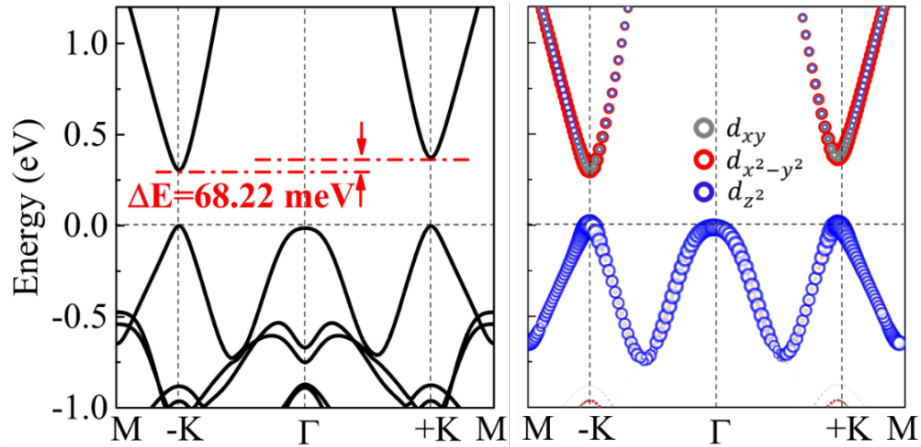


Fig. 4.10 Orbital-resolved band structures of VSi_2N_4 under 6% tensile strain when SOC is included.

4.4 Summary

In summary, via first-principles calculations, we find that the VSi_2N_4 monolayer is a ferromagnetic semiconductor with valley-contrasting physics. The intrinsic VSi_2N_4 is a XY magnet with a magnetic critical temperature over 300 K. By rotating the magnetization orientation from IP to OOP, the valley polarization of 63.11 meV can be achieved on the valence bands of VSi_2N_4 , which results in the AVHE. Moreover, based on model analysis, we unveil that valley splitting is proportional to the cosine function of polar angle θ of spin, and the combination of intrinsic FM exchange coupling and SOC of localized $3d$ electrons of V gives rise the valley depolarization in VSi_2N_4 when spin is OOP. More interestingly, under 4% tensile strain, the magnetic anisotropy of VSi_2N_4 can be tuned from IP to OOP, and spontaneous valley polarization is generated, indicating that the AVHE can be realized in VSi_2N_4 without manipulating the magnetization orientation. Our work unveils the spin-valley coupling in VSi_2N_4 , which makes VSi_2N_4 hopefully applicable in the valleytronic and spintronic nanodevices.

Chapter 5 Strain-tunable chiral magnetism in 2D Janus magnets

5.1 Introduction

2D magnets, which integrates the ideal interface, miniaturization, and long-sought magnetism, provide a fascinating platform for the spintronic research. Some exciting phenomenon, such as huge tunneling magnetoresistance, long-distance magnon transports and magnetization switching driven by spin-orbital torque (SOT) [82, 84, 199, 200], have been realized in the 2D magnets-based device. However, most of these 2D magnets lack high T_c or large PMA which are two key parameters in realizing the practical spintronic device with low-energy consumption, high-thermal stability and high-storage density [7, 84, 201, 202]. Therefore, tremendous efforts have been devoted to searching intrinsic 2D magnets with high T_c and large PMA, or effective method which can enhance these properties. For example, Huang et al propose that isovalent alloying can obviously enhance FM exchange coupling. Compared with CrI_3 , T_c of semiconducting alloy compounds CrWI_6 is enhanced from ~ 50 K to ~ 180 K, and PMA is also enhanced from 1.5 meV/u.c. to 5.4 meV/u.c. [124]. Moreover, through breaking the inversion symmetry of 2D magnets, especially constructing the Janus structure [203, 204], the sizable DMI can be obtained. As an asymmetric exchange interaction induced by SOC, the DMI favors the formation of chiral magnetic structures, such as chiral domain walls and skyrmions, which can be manipulated by small electrical currents and are promising for spintronic applications in mid-term future [39, 205-208]. Furthermore, since the 2D magnets can be integrated into various heterostructures, the chiral spin textures are hopefully tuned by various proximity effects. For example, using the Edelstein effect [15], the spin current that arises from adjacent graphene layer could be injected in 2D magnets to control the motion of chiral spin textures.

Magnetic properties are closely related with the structural parameters of materials, and strain can directly influence the structures of materials. Therefore, strain engineering has been shown as effective method for tuning different magnetic properties [209-211]. In FeRh/BaTiO₃ heterostructure, the FeRh films can be transferred from AFM order to FM order by voltage-induced strain [212] and in Fe₃GeTe₂ monolayer, the strain-controlled PMA enhancement has been theoretically predicted [213]. For 2D materials, the lattice strain can be modified through interfacing with various substrates or fabricating stretchable heterostructures [214]. These results highlight possibility that tuning basic magnetic parameters and even inducing distinct spin textures in 2D Janus magnets through strain engineering.

Above results highlight possibility that tuning basic magnetic parameters and even inducing distinct spin textures in 2D Janus magnets through strain engineering. Here, via first-principles calculations and Monte Carlo simulations (atomic spin model simulations), we systematically investigate the structural and magnetic properties of 2D Janus chromium dichalcogenides CrXTe ($X=S, Se$) under strain. 1T-CrTe₂ bulk is a layered compound and has high T_c around 310 K [215]. Recently, few-layer 1T-CrTe₂ has been exfoliated from the bulk phase and proved to be able to retain high T_c [216], which makes Janus CrXTe monolayers hopefully fabricated. We find that the CrSTe monolayer has high T_c of 295K and an out-of-plane magnetic anisotropy. In CrSeTe monolayer, the DMI is comparable to that in state-of-the-art FM/heavy metal (HM) heterostructures, which can favor the formation of chiral DW and skyrmions. As tensile strain increasing, the FM exchange coupling and PMA of Janus CrXTe monolayers both increase significantly, and the magnitude of DMI is reduced. Therefore, the ferromagnetism of Janus CrXTe monolayers is obviously enhanced, specially, distinct spin textures are induced in CrSeTe monolayer.

5.2 Methodology

We have performed first-principles calculations within density functional theory (DFT) as implemented in the Vienna *ab initio* simulation package (VASP). The

exchange correlation effects are calculated within the generalized gradient approximation (GGA) of Perdew-Burke-Ernzerhof (PBE) form. In order to describe the strongly correlated $3d$ electrons of Cr, the GGA+U method is applied ($U_{eff} = 2$ eV) [217, 218]. The atom positions are fully relaxed until the Hellmann-Feynman force is less than 10^{-3} eV/Å. The cutoff energy is set to 400 eV, and Γ -centered $24 \times 24 \times 1$ \mathbf{k} -point grids are good enough for sample the Brillouin zone. Phonon dispersions are calculated by the PHONOPY code. To investigate the magnetic properties of CrXTe, we adopt the following model Hamiltonian:

$$H = -J \sum_{\langle i,j \rangle} \mathbf{S}_i \cdot \mathbf{S}_j - K \sum_i (S_i^z)^2 - \sum_{\langle i,j \rangle} \mathbf{D}_{ij} \cdot (\mathbf{S}_i \times \mathbf{S}_j) - \mu_{Cr} B \sum_i S_i^z \quad (5.1)$$

In this equation, \mathbf{S}_i is a unit vector representing the orientation of the spin of the i th Cr atom, and $\langle i, j \rangle$ represents the nearest-neighbor Cr atom pairs. J , K , and \mathbf{D}_{ij} represent the Heisenberg exchange coupling, single ion anisotropy and DMI respectively. To obtain the J , we build a $2 \times 1 \times 1$ supercell and calculate the energies of two collinear spin configurations shown in Fig. 5.1. The total energies for these spin configurations are:

$$E_{FM} = E_0 - 6J \quad (5.2a)$$

$$E_{AFM} = E_0 + 2J \quad (5.2b)$$

Therefore, J equals $(E_{AFM} - E_{FM})/8$. The K is defined as the energy difference between in-plane and out-of-plane magnetizations of a 1×1 unit cell of CrXTe. For obtaining the orbital-hybridization-resolved and atom-resolved MAE, the spin-orbit coupling is calculated for each orbital angular momentum, and all elements in spin-orbit coupling matrix are obtained. By comparing the SOC matrix between out-of-plane and in-plane magnetization, one can get orbital-resolved MAE. The atom-resolved MAE is just the integration of MAE of each specific atom. The DMI vector \mathbf{D}_{ij} can be expressed as:

$$\mathbf{D}_{ij} = d_{\parallel} (\hat{\mathbf{z}} \times \hat{\mathbf{u}}_{ij}) + d_{ij,z} \hat{\mathbf{z}} \quad (5.3)$$

Here, d_{\parallel} and $d_{ij,z}$ are in-plane and out-of-plane component of \mathbf{D}_{ij} respectively. To obtain d_{\parallel} , we calculate the energies of clockwise (CW) and anticlockwise (ACW)

spin configurations as shown in Fig. 5.2, and d_{\parallel} equals $(E_{ACW} - E_{CW})/12$ [47]. Due to the sign variation of $d_{ij,z}$ for the six nearest neighbors of the Cr atom, the contribution to total DMI from $d_{ij,z}$ vanishes in average. To obtain the atom-resolved localization of the SOC energy difference ΔE_{soc} , the SOC is calculated for each atom layer in Janus structures. By comparing the atom-layer SOC energy between the opposite chiral spin configurations, one can obtain the ΔE_{soc} .

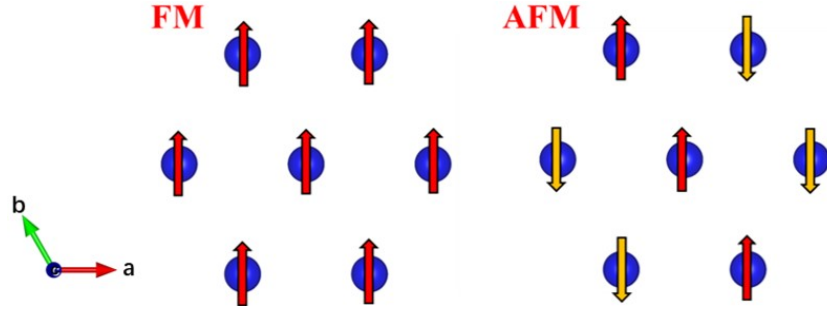


Fig. 5.1 Spin configurations for the calculations of J .

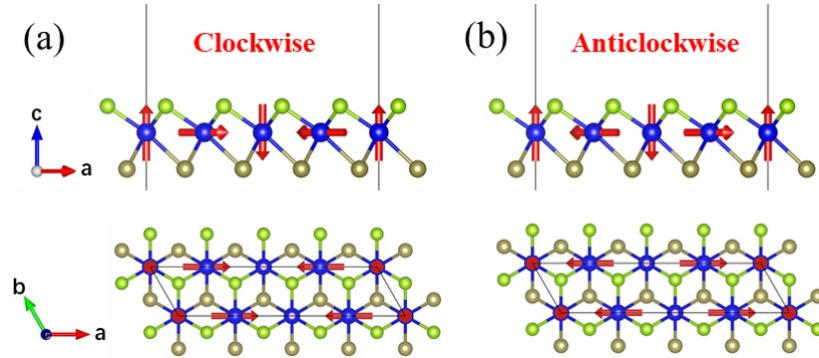


Fig. 5.2 Top view and side view of CW (left panel) and ACW (right panel) spin configurations implemented to calculate the DMI.

The SOC is included in the calculation of the K and \mathbf{D}_{ij} except the J . The SOC effect on J is also tested. We find that for the pristine CrS(Se)Te monolayer, $J = 23.94$ (15.22) meV when SOC is considered, which is very close to $J = 24.00$ (15.11) meV without SOC. The sign convention is that $J > 0$ represents FM coupling, $K > 0$ refers to PMA and in-plane DMI component $d_{\parallel} > 0$ favors CW spin configurations. Based on calculated magnetic parameters and spin Hamiltonian Eq. 5.1, the Monte Carlo

(MC) simulations with Metropolis algorithm are applied to explore the spin textures and estimate T_c of CrXTe. The specific process of MC simulations with Metropolis algorithm can be understood as: (1) an initial state is given. (2) change the spin of site i from \mathbf{S}_i to \mathbf{S}'_i randomly. (3) Calculate the energy change $\Delta E = E(\mathbf{S}_i) - E(\mathbf{S}'_i)$ and probability $P = \exp(-\frac{\Delta E}{k_B T})$. (4) Generate a random number r , which is between 0 and 1. (5) if $P > r$, accept the spin variation. (6) Go to the next site and start from step (3) until covering all the spins in system. (7) Keep running the whole process until the total energy of the system reaches equilibrium.

In all MC simulations, a $160 \times 160 \times 1$ supercell with periodic boundary is adopted and for making the system reaches thermal stability, 2×10^5 MC steps are employed for each temperature point. All MC simulations are performed with JuMag package [219].

5.3 Results and discussion

5.3.1 Pristine CrXTe ($X=S, Se$) monolayer

The crystal structure of CrXTe monolayers is shown in the Fig. 5.3(a). The Cr atoms in central layer forms a triangular lattice with C_{6v} symmetry, and after sandwiched by two atomic layers of different chalcogen atoms represented by light-green (X) and dark-green (Te) balls, the overall symmetry reduces to C_{3v} . The optimized structural parameters of CrXTe monolayers and magnetic moments of Cr, X and Te atoms are listed in Table 5.1. The optimized lattice constant of CrSTe is smaller than CrSeTe, due to the smaller atomic radii of S compared with that of Se. With the same computational method and accuracy, we also obtain the lattice constant of CrTe₂ monolayer, 3.70 Å, which yields good comparison with the experimental value of CrTe₂ bulk, 3.79 Å [216]. One can see that the lattice constant of CrSTe and CrSeTe is smaller than CrTe₂ due to the largest radii of Te among the S, Se and Te. For a specific CrXTe monolayer, the atomic radii of Te is larger than that of X . Therefore, d_1 and θ_2 is always smaller than d_2 and θ_1 respectively. The difference of top and bottom atom layer induces ISB in CrXTe monolayer, which is essential for

DMI. The main contribution to magnetism of CrXTe comes from the Cr atoms, meanwhile, X and Te are both effectively spin-polarized due to proximity effects. To confirm the structural stability of CrXTe monolayers, we calculate phonon spectrums as shown in Fig. 5.3(b) and (c). One can see that there is no imaginary frequency in Brillouin zone, which suggests that CrXTe monolayers are dynamically stable. Furthermore, to investigate electronic states of CrXTe monolayers, we calculate the orbital and spin projected band structures as shown in Fig. 5.4. The band structures show that CrXTe monolayers are metallic. For spin-up channel, the occupied states are dominated by $3d$ electrons of Cr. However, for spin-down channel, the occupied states mainly come from p states of X and Te. These results are consistent with the opposite spin orientations between Cr and X, Te as shown in Table 5.1.

Table 5.1 The optimized lattice constants a , bond length of Cr-X d_1 and Cr-Te d_2 , bonding angle of Cr-X-Cr θ_1 and Cr-Te-Cr θ_2 , and magnetic moments of Cr μ_{Cr} , S μ_S , Se μ_{Se} and Te μ_{Te} of Janus CrXTe monolayer. The unit of a , d_1 , and d_2 is Å. The unit of θ_1 and θ_2 is deg. The unit of μ_{Cr} , μ_S , μ_{Se} , and μ_{Te} is μ_B . The opposite sign of magnetic moment between S, Se, Te and Cr atoms reveals that the exchange coupling between them is AFM.

	a	d_1	d_2	θ_1	θ_2	μ_{Cr}	μ_S	μ_{Se}	μ_{Te}
CrSTe	3.47	2.34	2.84	95.66	75.22	3.13	-0.20	--	-0.15
CrSeTe	3.56	2.48	2.82	91.67	78.26	3.20	--	-0.25	-0.18

5.3.2 Strain tunable magnetic parameters

Now we focus on the magnetic interaction parameters including J , K , and d_{\parallel} , and their change under strain. The value of strain is defined as the $(a - a_0)/a_0$, where a and a_0 are the lattice constants of strained and unstrained CrXTe monolayers. As shown in Fig. 5.3(c), the nearest-exchange coupling of CrS(Se)Te monolayer is FM and when the tensile strain increases from 0% to 5%, the magnitude of this FM coupling can be effectively enhanced from 24.00 (15.11) to 32.19 (28.78) meV. Fig. 5.3(d) shows K of CrXTe as a function of strain. One can see that pristine CrSTe has

PMA of 0.29 meV, and CrSeTe has IMA of 0.07 meV. Interestingly, by just 5% tensile strain, the PMA of CrS(Se)Te can be significantly enhanced to 1.51 (2.35) meV, which is much larger than that of CrI₃, 0.80 meV [217]. We find that CrXTe monolayers have sizable DMI as shown in Fig. 5.3(e). Especially, the d_{\parallel} of pristine CrSeTe monolayer reaches to 2.01 meV, which is comparable to state-of-the-art FM/HM heterostructures, such as Pt/Co (~ 3.0 meV) [220] and Fe/Ir(111) (~ 1.7 meV) [221], thin films that has been demonstrated to be able to host chiral spin textures. One also can see that the tensile strain reduces the magnitude of d_{\parallel} of both CrSTe and CrSeTe monolayers. For the CrTe₂ monolayer, $J = 2.16$ meV, $K = -2.14$ meV, and $d_{\parallel} = 0$ meV. One can see that, compared with the CrTe₂ monolayer, the FM coupling and IMA is obviously increased and decreased respectively in Janus structures, which is more beneficial for the formation of long-range magnetic order under finite temperature.

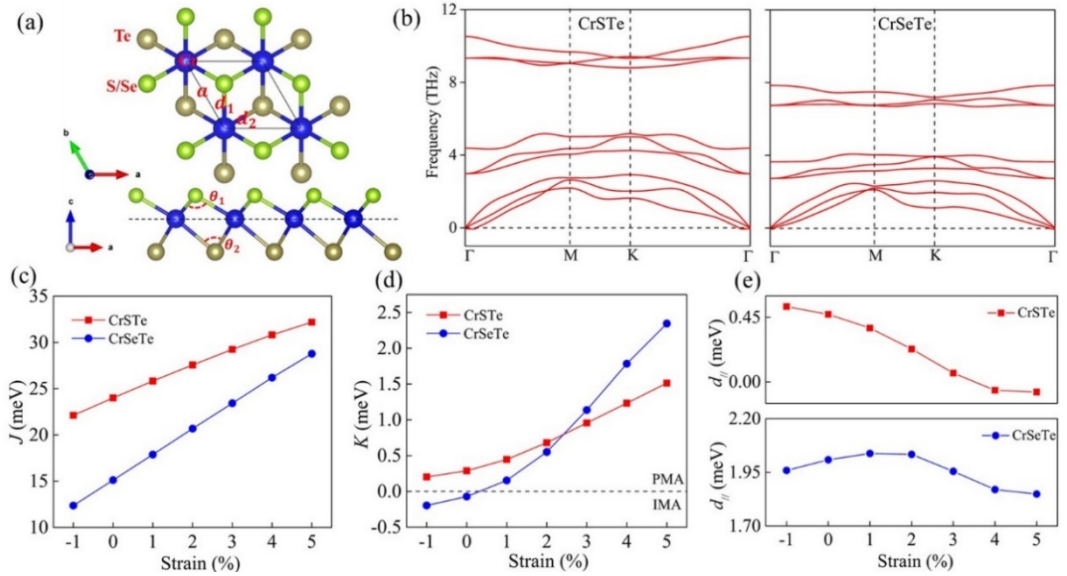


Fig. 5.3 Top view and side view of crystal structures and (b) Phono dispersions of Janus CrXTe monolayers. (c) The nearest-neighboring exchange coupling J , (d) single ion anisotropy K and (e) in-plane DMI component d_{\parallel} as functions of strain in Janus CrXTe monolayers.

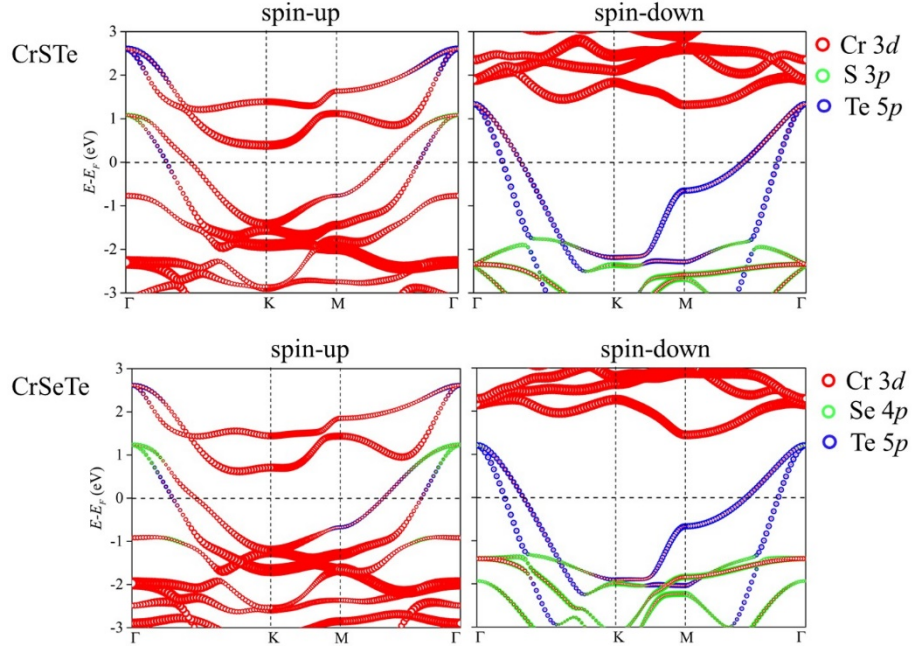


Fig. 5.4 Orbital-resolved spin-up (left panel) and spin-down (right panel) band structures of CrSTe and CrSeTe. Red, green and blue hollow circles represent the contribution from $3d$ orbitals of Cr, $4p$ orbitals of Se, and $5p$ orbitals of Te respectively.

The physical mechanisms of the change of J and K under strain are similar for CrSTe and CrSeTe. Therefore, in the following discussion, we choose CrSeTe as an example to detailly show how tensile strain enhances the FM coupling and PMA. Since the bonding angle of Cr-Se/Te-Cr is close to 90° , according to the Goodenough-Kanamori-Anderson (GKA) rules, the indirect exchange coupling between two nearest-neighboring Cr cations through intervening Se/Te anion is FM (up panel of Fig. 5.5(a)). On the contrary, the direct exchange coupling between two nearest-neighboring Cr cation is AFM (down panel of Fig. 5.5(a)). The competition between indirect FM and direct AFM couplings decides the final magnetic arrangement of Cr atoms. When tensile strain is applied, the Cr-Te and Cr-Se distances hardly change (blue and black line in Fig. 5.5(b)), whereas, the Cr-Cr distance obviously increases (red line in Fig. 5.5(b)). Therefore, compared with indirect FM coupling, the direct AFM coupling decreases more strongly, which results the effective enhancement of J [222].

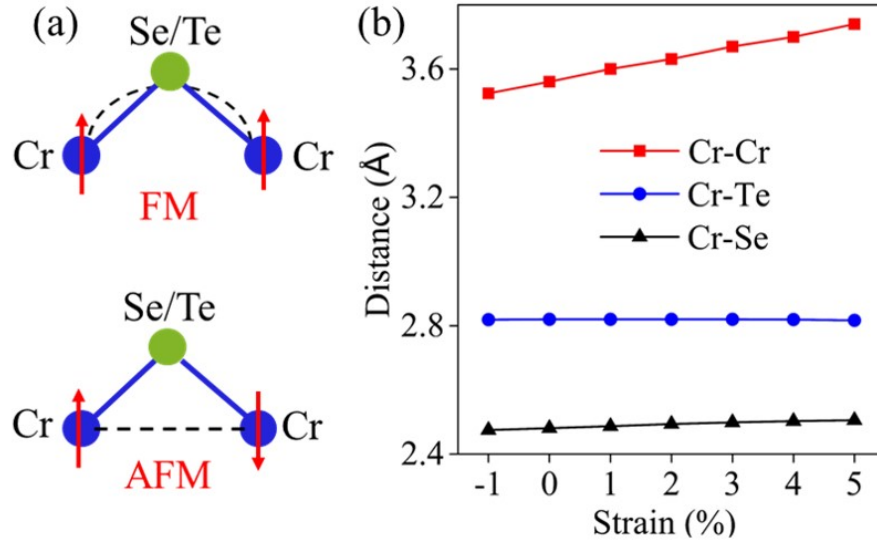


Fig. 5.5 (a) Schematic diagrams of Cr-Se/Te-Cr superexchange and Cr-Cr direct exchange couplings in Janus CrSeTe monolayer. (b) Bond lengths of Cr-Cr, Cr-Te and Cr-Se as functions of the strain.

From the atom-resolved MAE of the CrSeTe monolayer [Fig. 5.6(a)], one can see that the PMA of Te atom is enhanced significantly by tensile strain, which is responsible for the K increasing. To further elucidate mechanisms of MAE change of Te atom, we perform a comparative analysis of MAE from orbital hybridization between the CrSeTe monolayer under 0% and 5% tensile strain as shown in Fig. 5.6(b) and (c). For Te in pristine CrSeTe, the hybridization between p_y and p_x gives rise to IMA, however the hybridization between p_y and p_z constitutes PMA. The small magnitude of anisotropy of Te in pristine CrSeTe arises from the competition of these two hybridizations. When the strain is applied on the CrSeTe, the PMA contribution comes from the p_y and p_z hybridization significantly increases and the IMA contribution arisen from p_y and p_x hybridization hardly change, which results the giant PMA enhancement of the CrSeTe monolayer. Furthermore, we investigate the origin behind the change of MAE arising from $5p$ orbital hybridization of the Te atom. According to the second-order perturbation theory, the MAE can be expressed as Eq. 2.1 where the difference of spin-orbital angular momentum matrix elements are

shown in Table 5.2. In Fig. 5.6(d) and (e), we plot the projected density of states (pDOS) for Te atoms of CrSeTe monolayers under 0% and 5% tensile strain. One can see that the spin-down occupied p_z states ($p_z^{o^-}$) is shifted to the Fermi level E_F (indicated by the dashed blue arrow in Fig. 5.6(e)) when tensile strain is enhanced. The matrix elements difference between $p_z^{o^-}$ and spin-up unoccupied p_y states ($p_y^{u^+}$) is 1 as shown in Table 5.2, which is responsible for PMA contribution from p_y and p_z hybridization. Due to the shift of $p_z^{o^-}$ states, the value of $E_u^{\sigma'} - E_o^{\sigma}$ obviously decreases. Therefore, the positive MAE from p_y and p_z hybridization is enhanced. Compared with p_z states, the p_x and p_y states barely change, which is responsible for the much smaller variation of MAE from p_x and p_y hybridization.

Table 5.2 The matrix differences between magnetization along z [001] and x [100] in Eq. 2.1. u^+ , o^- and o^+ represent unoccupied spin-up states, occupied spin-down and spin-up states respectively.

u^+	o^-			o^+		
	p_y	p_z	p_x	p_y	p_z	p_x
p_y	0	1	-1	0	-1	1
p_z	1	0	0	-1	0	0
p_x	-1	0	0	1	0	0

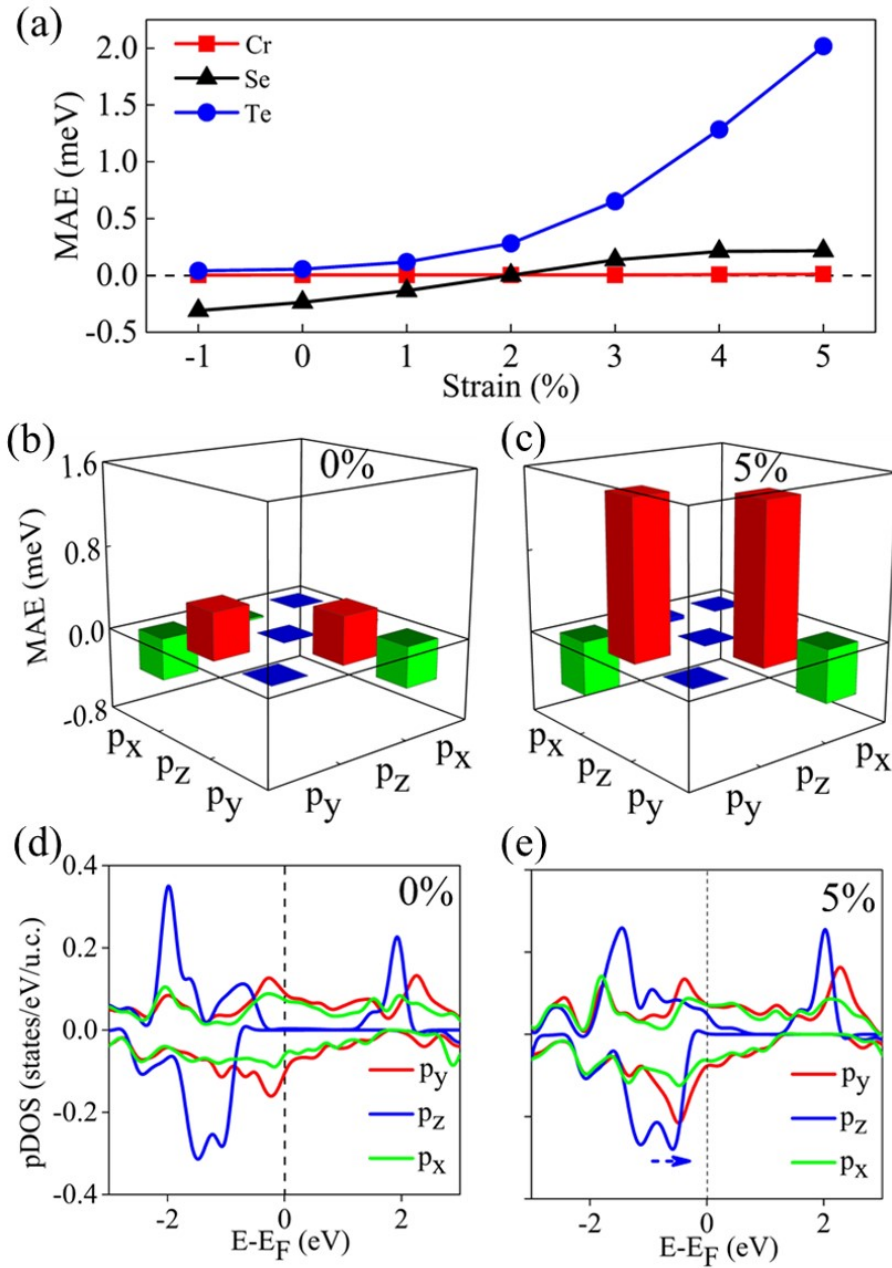


Fig. 5.6 Atom-resolved MAE of Janus CrSeTe monolayer as functions of strain. (b) and (c) MAE contributions from $5p$ orbitals hybridization, and (d) and (e) the projected density of states of Te in Janus CrSeTe monolayer under 0% and 5% tensile strain.

For investigating the exceptional DMI in Cr X Te monolayer, we calculate SOC energy difference ΔE_{soc} of the opposite chirality as shown in Fig. 5.7. One can see that the dominant contribution to the DMI stems from the adjacent X and Te atoms.

This behavior is similar to DMI in FM/HM heterostructures, where the SOC energy source comes from $5d$ transition metal in the interfacial layer. This is so called as the Fert-Levy type of DMI [46, 47]. In CrXTe monolayer, when polarized electrons transfer between Cr atoms through mediate X/Te atoms, the spin orientations of these electrons can be tilted due to the spin-orbit scattering. Under tensile strain, the Te contribution to DMI of CW chirality obviously decreases, which is responsible for the reduce of total DMI magnitude.

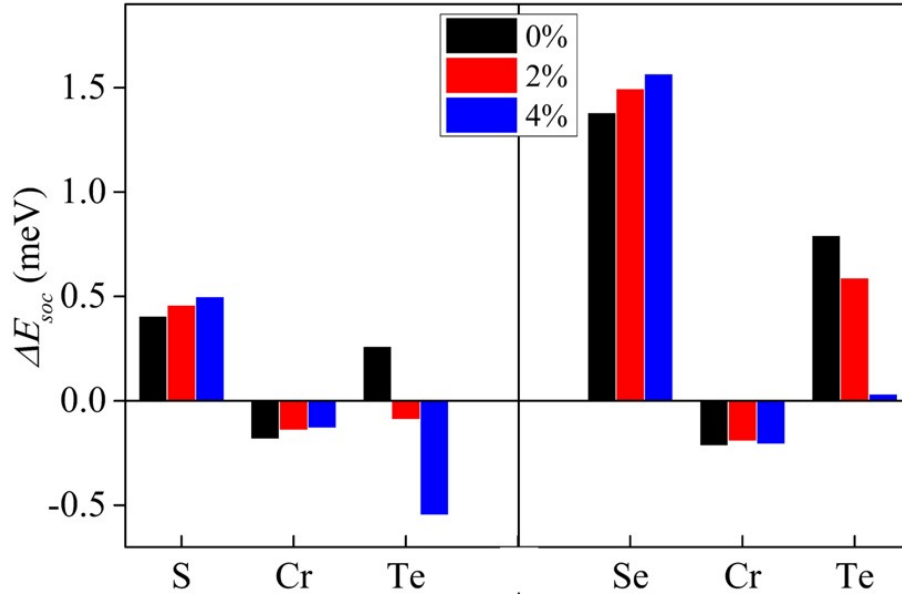


Fig. 5.7 Atom-resolved localization of the SOC energy difference ΔE_{soc} in Janus CrXTe monolayer. Black, red, blue bars represent ΔE_{soc} of CrXTe monolayers under 0%, 2%, and 4% tensile strain respectively.

5.3.3 Strain-tunable topological spin textures and Curie temperature

Once magnetic interaction parameters of spin Hamiltonian are determined by first principles calculation, we perform MC simulations to explore the spin textures and T_c of Janus CrXTe monolayers. We notice that the DMI/exchange coupling ratios $|d_{||}/J|$ of pristine CrSeTe monolayer is about 0.14 which is in the typical range of 0.10 - 0.20 for the skyrmions formation [34]. Therefore, it is possible to realize chiral spin textures in CrSeTe monolayer. Fig. 5.8(a) shows a phase diagram of spin textures of

CrSeTe monolayer in 10 K. For pristine CrSeTe, we obtain the worm-like domains separated by chiral Néel DW, the white part between the domains of up and down magnetization. Due to the in-plane magnetic anisotropy, the width of DW reaches to 2.7 nm. We find that the skyrmion states can be induced in pristine CrSeTe by an OOP magnetic field (B_z). One can see that the red domains shrink as the enhancement of B_z and isolated skyrmions begin to appear. When the B_z increases to 1.2 T, the worm domains disappear completely and the skyrmions tend to form an approximate hexagonal lattice. If keep increasing B_z , the density of skyrmions decreases and a uniform ferromagnetic state appears finally. The diameter of skyrmions decreases from 11.6 to 9.1 nm when B_z increases from 1.2 to 2.1 T.

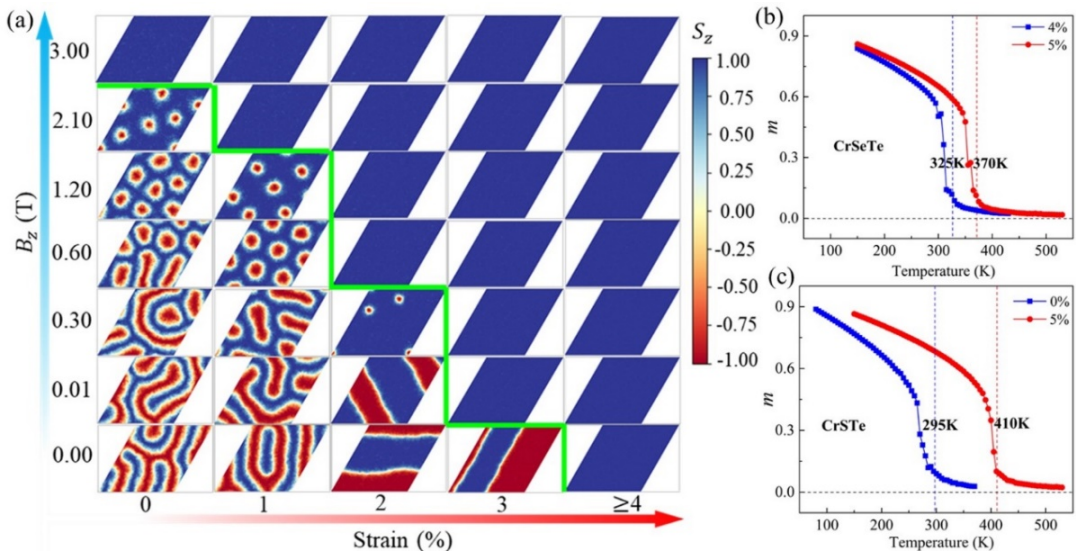


Fig. 5.8 Distinct spin textures for CrSeTe monolayer under increased tensile strains and external fields in 10K. The color map indicates the out-of-plane spin component of Cr atoms. The Curie temperatures (T_c) of (b) CrSeTe and (c) CrSTe monolayers under tensile strains.

As tensile strain increases, the size of domain in CrSeTe becomes much larger compared with pristine state, which is consistent with the smaller $|d_{||}/J|$, and the resulting larger DW energy. Meanwhile, the width of DW decreases obviously induced by transition of IMA to large PMA in CrSeTe. Due to the enhancement of

ferromagnetic exchange coupling and PMA, the critical external field that required for skyrmions formation, density and diameters of skyrmions all decrease. When tensile strain reaches up to 3%, the $|d_{\parallel}/J|$ decreases to 0.08, which is not in typical range for skyrmions formation. Therefore, the DW directly transform into uniform ferromagnetic state under a very small B_z , 0.01 T. If keep increasing tensile strain above 3%, the uniform ferromagnetic states appear. Moreover, these ferromagnetic states can retain over 325 K as shown in Fig. 5.8(b). Next, we explore the temperature influence on spin textures as shown in Fig. 5.9(a) and (b). One can see that the images of chiral domain wall, skyrmions and uniform ferromagnetic states all begin to be less well-defined and become more and more blurred as temperature increasing. When T increases to 150 K, this blurring starts to show the destabilization of chiral spin textures by thermal fluctuations, but the tendency of the evolution of chiral spin textures with external magnetic field or tensile strain is still clear and similar to the evolution at the low temperature. These results also indicate that chiral spin textures, including skyrmion particles, can sustain to at least 150 K in CrSeTe monolayer. For CrSTe monolayer, the magnetic ground state is ferromagnetic without chiral spin textures, which is consistent the very small $|d_{\parallel}/J|$ of 0.02. Notably, the T_c of pristine CrSTe reaches to 295 K (blue line in Fig. 5.8(c)) which is close to room temperature, and it can be further enhanced to 410 K when tensile strain increases to 5% (red line in Fig. 5.8(c)).

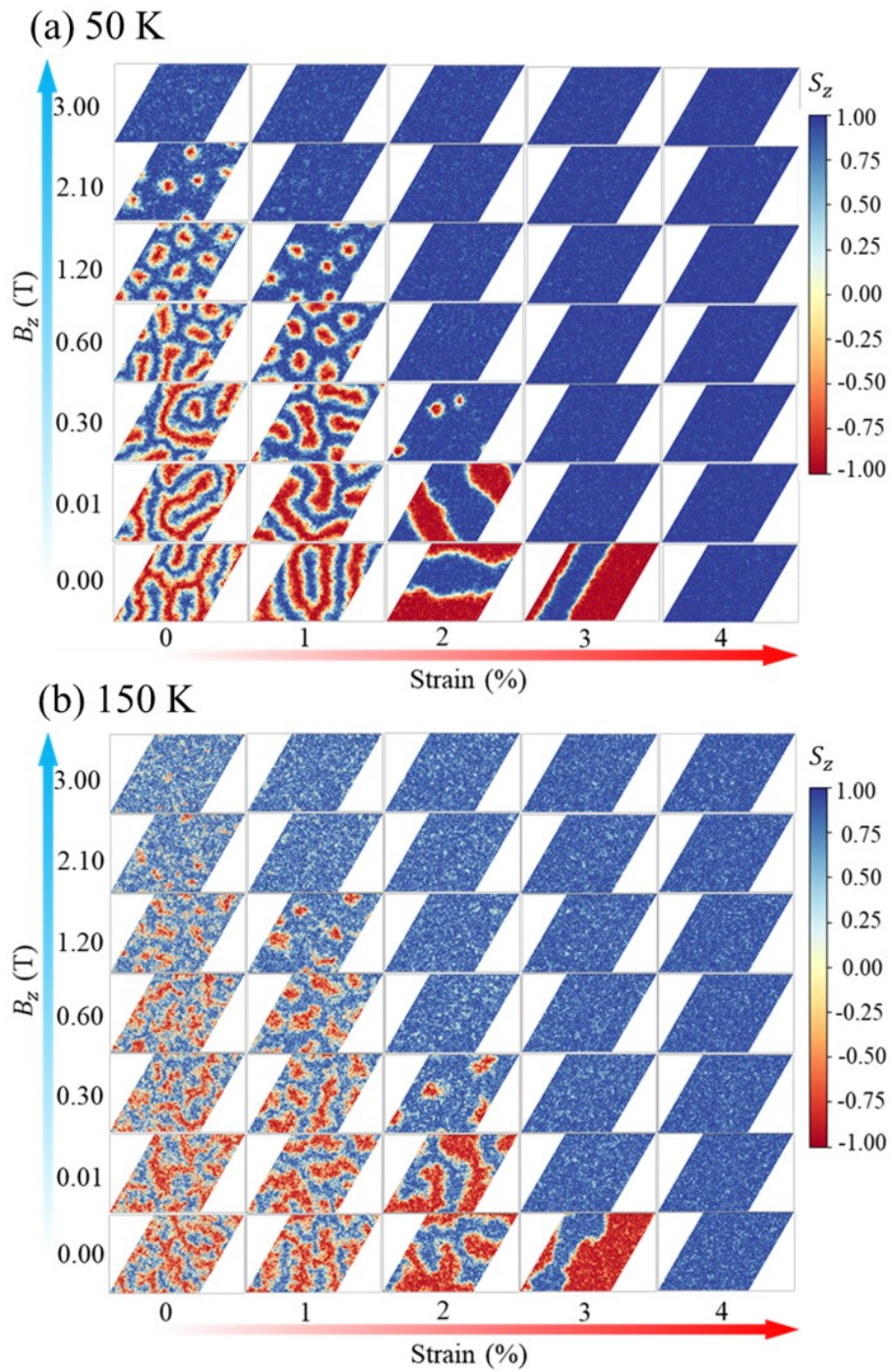


Fig. 5.9 Phase diagrams of spin textures of CrSeTe monolayer at (a) 50 K and (b) 150K.

5.4 Summary

In summary, using first principles calculation and MC simulations, we systematically investigate magnetic properties of Janus CrXTe monolayers. We find that the CrSTe monolayer has a high T_c of 295K and an out-of-plane magnetic anisotropy. The CrSeTe monolayer has large DMI, which favors the formation of chiral Néel DW. With an external magnetic field, the DW in CrSeTe can be tuned to skyrmion states. As tensile strain increasing, the FM exchange coupling and PMA of Janus CrXTe monolayers increase significantly, and the magnitude of DMI is reduced. Therefore, T_c of CrSTe is enhanced over 100 K under 5% tensile strain, and in CrSeTe, distinct spin textures from chiral Néel domain wall to uniform ferromagnetic states are induced. Moreover, the diameter and density of skyrmions in CrSeTe monolayer can be tuned by external magnetic field and strain. These 2D magnets can further replace complicated bulk magnets or FM/HM multilayers those are traditionally used to achieve chiral magnetism, which leads to simpler and more efficient spintronic devices. Our results thus provide a promising avenue and good candidates for experimental realization of topological spin textures and their manipulation in 2D magnets.

Chapter 6 Ferroelectrically controlled topological magnetism in Janus-magnet-based multiferroic heterostructure

6.1 Introduction

The magnetic skyrmion, as a topologically protected spin texture, is highly promising for non-volatile information carrier in next-generation spintronic devices with high-storage density and low-energy consumption because it has small size, stable configuration and can be driven by low threshold current [34-39, 223-225]. One key parameter for realizing skyrmion in materials is DMI which is originated from SOC and ISB [42-47]. In last decades, much efforts have been devoted to constructing ferromagnetic/heavy metal HSs with PMA and large DMI to realize skyrmion. Recently, through constructing Janus structures to introduce ISB, the large DMI can be realized in 2D magnetic materials leading to the formation of skyrmion [226, 227]. Compared with multilayers of ferromagnetic/heavy metal, a single 2D magnet has simpler structure, smaller size and is more beneficial for reducing defects. Besides skyrmion, the bimeron is another topologically nontrivial spin texture consisting of a vortex and an antivortex, which can be constructed by rotating the spin direction of skyrmion by an angle of 90° [228-230]. The bimeron can also be used as non-volatile information carrier for spintronic devices, based on materials with IMA [231, 232].

Another crucial task for practical application of topological spin textures, such as skyrmion and bimeron, is searching or developing method that can effectively control the mobility and morphology of these spin textures. Particularly, using electric field is considered as a more energy-dissipationless method compared with spin-polarized current, thermal excitation and external magnetic field (B_{ext}) [233-237]. However, since the electric field doesn't break time-reversal symmetry directly,

realizing the control of magnetism by electricity is difficult. Notably, previous works have demonstrated that the multiferroic system which combines ferroelectricity (FE), ferromagnetism and ISB provides an ideal platform for electric control of chirality, creation/annihilation, density and thermal stability of topological particles through switching the FE polarization [238-241]. In this chapter, using first-principles calculations and atomistic spin model simulations, we unveil that a novel type of FE-controlled topological magnetism can be realized in Janus magnet-based multiferroic heterostructure, MBST/In₂Se₃. The loops of vortices and antivortices can be transformed into skyrmions by switching the direction of ferroelectric polarization of In₂Se₃. Furthermore, in MBST/In₂Se₃ with up polarization, bimeron solitons can be obtained by applying IP magnetic field. Further analysis unravels that the variation of interlayer charge transfers induced by FE reversal gives rise the change of magnetic anisotropy, which is responsible for the topological magnetic phase transition in system.

6.2 Methodology

The first-principles calculations: The first-principles calculations are performed using the Vienna *ab Initio* Simulation Package (VASP), which is based on the density functional theory (DFT). The exchange-correlation interaction is described by the generalized gradient approximation (GGA) based on Perdew-Burke-Ernzerhof (PBE) function. The GGA+U method is applied ($U_{eff} = 3$ eV) to describe strongly correlated *3d* electrons of Mn [242, 243]. The projector-augmented wave (PAW) method is adopted [244], and the cutoff energy is set to 420 eV. The Brillouin zone is sampled using 24×24×1 Γ -center k -point grids. The vacuum space of at least 15 Å is used to avoid interactions between periodic replicas. The electronic convergence is performed with a tolerance of 10^{-7} eV. All structures are fully relaxed until Hellmann-Feynman force on each ion is less than 10^{-3} eV/Å. The interlayer van der Waals interaction is corrected by DFT-D3 method. Dipole corrections are included in calculations of multiferroic HS, and for obtaining the electric polarization of systems,

we directly integrate ρz over the supercell, where ρ represents the local charge density and z represents coordinates along the OOP direction [245].

Phonon calculations: In phonon calculations, the real-space force constants are computed with a $4 \times 4 \times 1$ supercell and $5 \times 5 \times 1$ k -point grids using the VASP code. The force constant matrices and phonon dispersions are calculated using the PHONOPY code. Fig. 6.1 shows the phonon band structure of the monolayer MBST. There is no imaginary frequency, which demonstrates the dynamic stability of MBST.

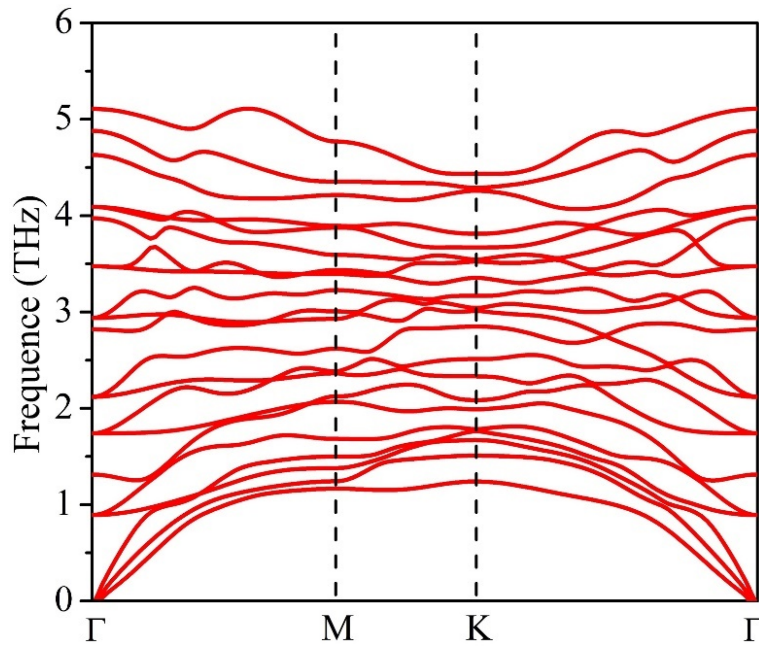


Fig. 6.1 Calculated phonon band structure for the $\text{MnBi}_2\text{Se}_2\text{Te}_2$ (MBST) monolayer.

Molecular dynamics: For verifying the thermal stability of MBST, we perform *ab initio* molecular dynamics (AIMD) implemented in VASP. The canonical NVT ensemble is used with Nosé thermostat [246]. A $4 \times 4 \times 1$ supercell with $1 \times 1 \times 1$ k -point grid is adopted. Each time step is set to 1fs, and simulations are performed for 10000 steps at 300K. The evolution of the total energy and temperature are shown in Fig. 6.2(a) and (b). The top and side views [see Fig. 6.2(c) and (d)] of MBST after simulations indicate that the structure is still maintained at initial phase.

Heterostructure configurations: Considering structural symmetries of In_2Se_3 and MBST, we propose twelve stacking configurations of MBST/ In_2Se_3 HS [see Fig. 6.3].

The total energies of optimized structures are shown in Fig. 6.4. Compared with the Se-terminated side, In_2Se_3 prefers to contact Te-terminated side of MBST. For both MBST/ $P\uparrow$ and $P\downarrow$, the configuration 6, where outmost Te and Bi atoms of MBST sitting at the hollow and top-In sites of In_2Se_3 , is most stable.

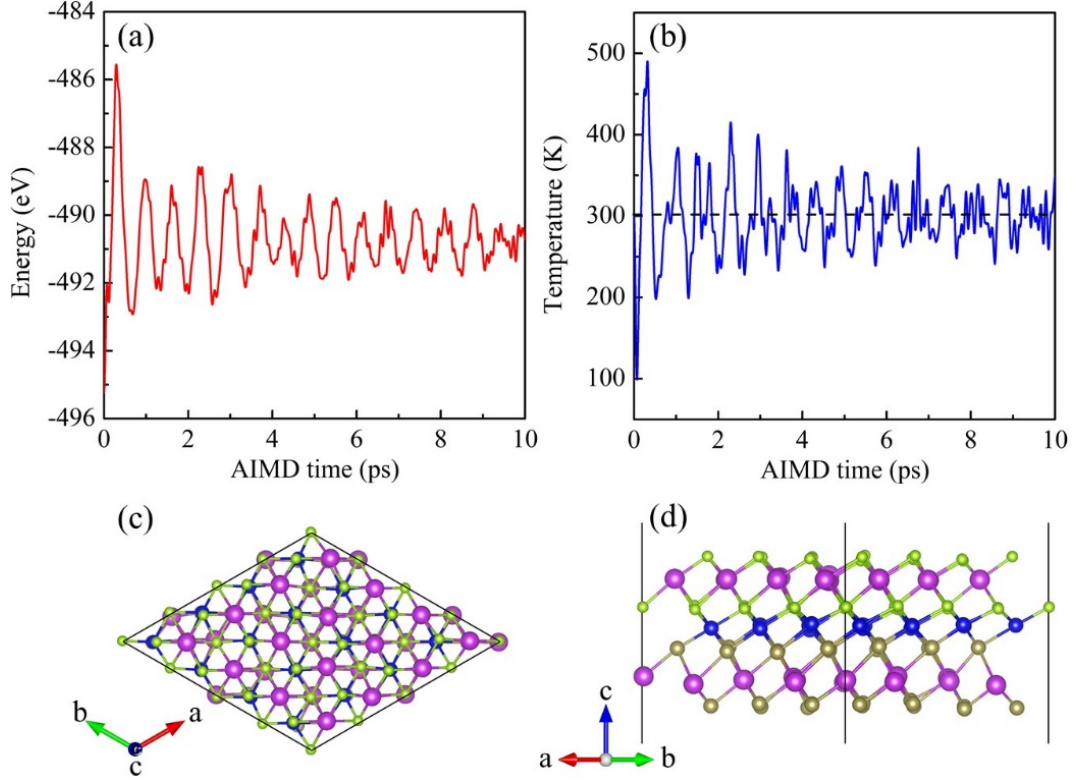


Fig. 6.2 (a) The evolution of total energy and (b) temperature during the *ab initio* simulations for MBST monolayer at 300K. The (c) top and (d) side views of MBST supercell after simulations of 10 ps. The green, purple, blue and brown balls represent Se, Bi, Mn, and Te elements, respectively.

Calculations of J , K , and d_{\parallel} : (i) For obtaining the nearest-neighboring (NN) exchange coupling J , we compare the energy difference of ferromagnetic and antiferromagnetic states of a $2\times 1\times 1$ supercell, i.e., $J = (E_{AFM} - E_{FM})/8$. The SOC effects are taken into account. Moreover, to determine the influence of next-nearest-neighboring (NNN) interactions, we expand the unit cell of MBST and calculate the DFT total energies of three different magnetic configurations [see Fig. 6.5]. The total energies of three magnetic configurations are given by:

$$E_{FM} = -12J_1 - 12J_2 + E_{other} \quad (6.1a)$$

$$E_{AFM1} = -4J_1 + E_{other} \quad (6.1b)$$

$$E_{AFM2} = -4J_1 + 4J_2 + E_{other} \quad (6.1c)$$

where J_1 and J_2 represents the NN and NNN exchange coupling, respectively. Here, SOC effects are also considered, and the magnetization is set to be along the positive direction of z axis. We find that $J_1 = 1.674$ meV, and $J_2 = 0.164$ meV. The magnitude of J_1 is much larger than that of J_2 , and is very close to the that directly obtained from 2×1 supercell ($J = 1.658$ meV). These results indicate that the NNN coupling is almost negligible in MBST systems. (ii) The magnetocrystalline anisotropy K_{MCA} is calculated as: $K_{MCA} = E_{M \rightarrow} - E_{M \uparrow}$, where $E_{M \rightarrow}$ and $E_{M \uparrow}$ represent the self-consistent total energy of system with magnetization along positive direction of x and z axes, respectively, when SOC effect is included. The magnetic shape anisotropy K_{MSA} is the sum of all magnetostatic dipole-dipole interactions up to infinity [247, 248] and calculated by: $K_{MSA} = E^{dip}/V_{u.c.} = -\frac{1}{2} \frac{\mu_0}{4\pi V_{u.c.}} \sum_{i \neq j}^N \frac{1}{r_{ij}^3} [\mathbf{M}_i \cdot \mathbf{M}_j - (\mathbf{M}_i \cdot \mathbf{r}_{ij})(\mathbf{M}_j \cdot \mathbf{r}_{ij}) \frac{3}{r_{ij}^2}]$, where \mathbf{M}_i and \mathbf{r}_{ij} represent local magnetic moments and vector connecting site i and j , respectively. A $250 \times 250 \times 1$ supercell is used in K_{MSA} calculation to ensure the reliability of results. Also, we would like to note that skyrmions and merons are small topological defects on the uniform magnetic background, which indicates that shape anisotropy can be considered as the contribution to effective magnetic anisotropy. (iii) The chirality-dependent total energy difference approach is applied to obtain the DMI strength [47]. Since the out-of-plane component cancels each other, we only provide the in-plane (IP) component of DMI, d_{\parallel} . In calculations of DMI, a $4 \times 1 \times 1$ supercell with $6 \times 24 \times 1$ k -point grids are adopted. To obtain d_{\parallel} , we calculate the energies of CW and ACW spin configurations as shown in the Fig. 6.7, and d_{\parallel} equals $(E_{ACW} - E_{CW})/12$. (iv) In facts, the spin Hamiltonian for describing spin interactions between Mn atoms can be written as $H = \mathbf{S}_i \cdot \vec{J} \cdot \mathbf{S}_j$, where the exchange matrix has components

$$\vec{J} = \begin{bmatrix} J_{xx} & \Gamma_{xy} + D_z & \Gamma_{xz} - D_y \\ \Gamma_{xy} - D_z & J_{yy} & \Gamma_{yz} + D_x \\ \Gamma_{xz} + D_y & \Gamma_{yz} - D_x & J_{zz} \end{bmatrix}. \quad (6.2)$$

Here, the J and D represents Heisenberg exchange coupling and DMI, respectively. The Γ_{xy} , Γ_{xz} , and Γ_{yz} are the additional, symmetric, off-diagonal contributions to the exchange tensor. For determining Γ of MBST, such as Γ_{xy} , we compare the energies of a $2 \times 1 \times 1$ supercell with spin configurations of Mn pairs as $\{(S\ 0\ 0), (0\ S\ 0)\}$ and $\{(-S\ 0\ 0), (0\ S\ 0)\}$. For $\{(S\ 0\ 0), (0\ S\ 0)\}$, $E_1 = J_{xx} + J_{yy} + 4\Gamma_{xy}$, and for $\{(-S\ 0\ 0), (0\ S\ 0)\}$, $E_2 = J_{xx} + J_{yy} - 4\Gamma_{xy}$. Accordingly, $\Gamma_{xy} = (E_1 - E_2)/8$. Γ_{xy} , Γ_{xz} , and Γ_{yz} of MBST are 0.0027, 0.0038, and 0.0018 meV, respectively. One can see that the magnitude of Γ is very limited and is much smaller compared with DMI components. These results indicate that Γ can be negligible for MBST systems.

Calculations of layer-resolved localization of the SOC energy difference ΔE_{soc} between opposite chiral spin configurations and layer-resolved MAE: The SOC is calculated for each atom layer in MBST and MBST/In₂Se₃ HSs. By comparing the atom-layer SOC energy between anticlockwise and clockwise configurations, and in-plane (100) and out-of-plane (001) magnetic orientations, one can obtain layer-resolved ΔE_{soc} and MAE, respectively.

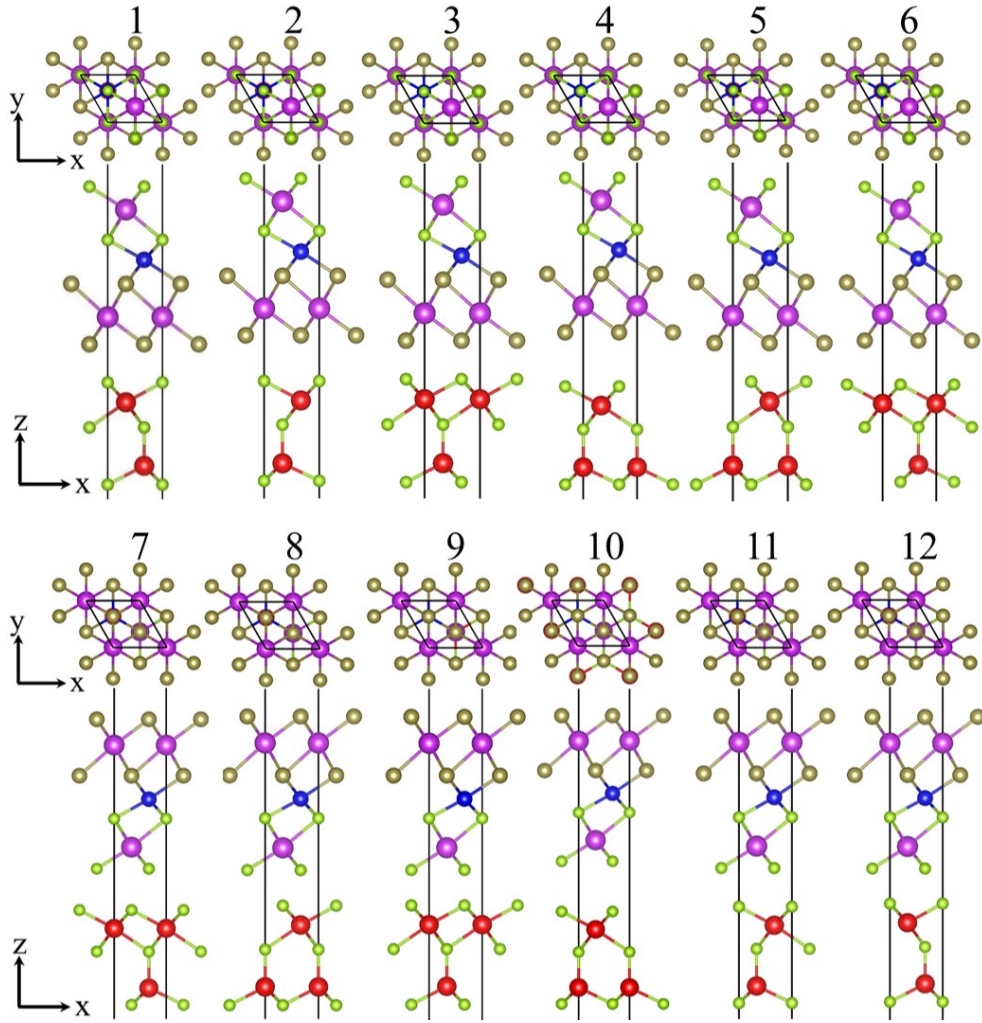


Fig. 6.3 Top and side views of twelve stacking configurations for MBST/In₂Se₃ heterostructure (HS). The green, purple, blue, brown, and red balls represent Se, Bi, Mn, Te, and In elements, respectively.

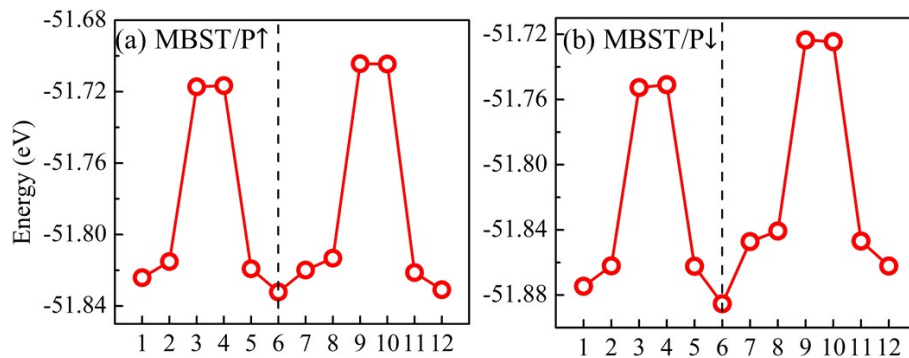


Fig. 6.4 Total energies of twelve stacking configurations for (a) MBST/P \uparrow and (b) MBST/P \downarrow HSs. The dashed line indicates the most stable stacking.

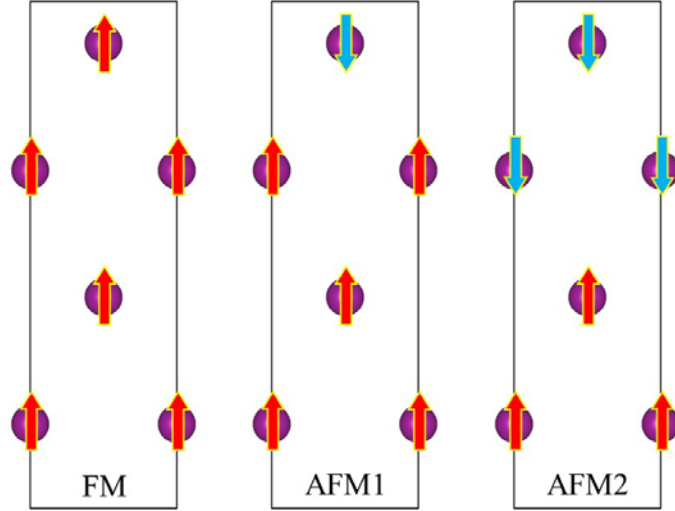


Fig. 6.5 Three different spin configurations applied to calculate the nearest-neighbor and next-nearest-neighbor exchange coupling parameters.

Atomic Spin Model Simulations: All atomic spin model simulations are performed using VAMPIRE package [249]. The hexagonal lattice of MBST is transformed into a lattice with an orthorhombic unit cell. Then, this unit cell is extended to a 60×60 nm square with the periodic boundaries.

The time evolution of atomic spin is described by the Landau-Lifshitz-Gilbert (LLG) equation. The LLG is given by: $\frac{\partial \mathbf{S}_i}{\partial t} = -\frac{\gamma}{(1+\lambda^2)} [\mathbf{S}_i \times \mathbf{B}_{eff}^i + \lambda \mathbf{S}_i \times (\mathbf{S}_i \times \mathbf{B}_{eff}^i)]$, where \mathbf{S}_i is the unit vector of the spin moment of site i , γ is gyromagnetic ratio and λ represents damping constant. \mathbf{B}_{eff}^i represents the effective magnetic field on each spin and can be expressed as: $\mathbf{B}_{eff}^i = -\frac{1}{\mu_s} \frac{\partial H}{\partial \mathbf{S}_i}$, where H is the spin Hamiltonian of MBST. We choose $\lambda = 0.2$ for MBST, considering magnetism originates from $3d$ electrons of Mn, and Bi and Te process strong SOC [250]. Moreover, we calculate spin textures of MBST with λ in range of 0.1 to 0.4 [see Fig. 6.6]. One can find that loops of vortices and antivortices emerges, which is robust to the value of λ .

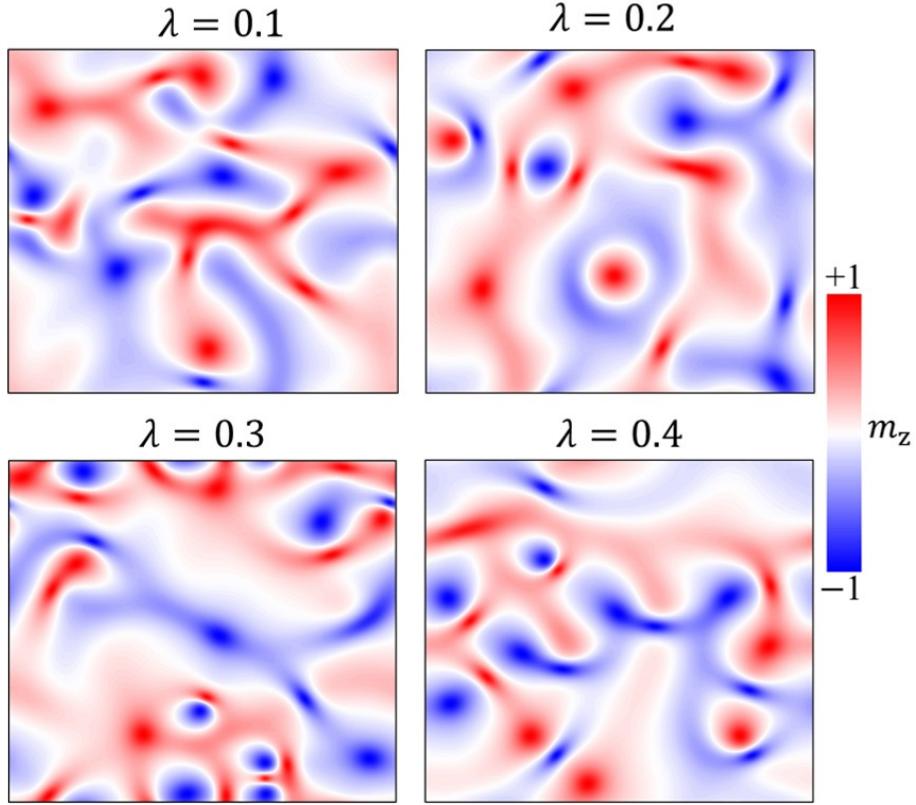


Fig. 6.6 The spin textures for MBST monolayer with λ in range of 0.1 to 0.4. The color map indicates the out-of-plane spin component of Mn atoms.

The κ for MBST monolayer: The dimensionless parameter κ is calculated by: $\kappa = \left(\frac{4}{\pi}\right)^2 \frac{AK}{D^2}$, where A is exchange stiffness, and K and D is the magnetic anisotropy and DMI parameter in micromagnetic format, respectively. Based on Heisenberg model, the exchange energy can be expressed as: $E_{ex} = J \sum_{i,\delta} (\boldsymbol{\delta}_i \cdot \nabla \mathbf{m}_i)^2$, where J is the magnitude of exchange coupling, $\boldsymbol{\delta}_i$ is the vector between neighboring local spin \mathbf{m}_i . In micromagnetic format, $E_{ex} = A \int dV [(\nabla m_x)^2 + (\nabla m_y)^2 + (\nabla m_z)^2]$, where A is the exchange stiffness. For MBST monolayer, one can obtain $A = \frac{\sqrt{3}J}{t_F}$, where t_F is the assumed thickness of magnetic film. The micromagnetic anisotropy is calculated as: $K = \frac{K_{eff}}{V} = \frac{2K_{eff}}{\sqrt{3}a^2 t_F}$, where a is the lattice constant. The micromagnetic DMI strength D is calculated as: $D = \frac{d_{\parallel} \sqrt{3}}{a t_F}$ [47], where d_{\parallel} is the IP component of DMI. Therefore, κ can be rewritten as $\kappa = \left(\frac{4}{\pi}\right)^2 \frac{2JK_{eff}}{3d_{\parallel}^2}$.

6.3 Results and discussion

6.3.1 The crystal structure of MBST/In₂Se₃ heterostructure

The crystal structure of Janus MBST monolayer is shown in Fig. 6.7. MBST consists of septuple Te-Bi-Te-Mn-Se-Bi-Se layers, with atoms in each layer forming a 2D triangular lattice. MBST can be constructed by replacing triple Te-Bi-Te layers of MnBi₂Te₄ (MBT) monolayer with a triple Se-Bi-Se layers [251], where MBT monolayer is a topologically trivial ferromagnetic semiconductor [252, 253]. The crystal symmetry of MBST is C_{3v} , and intrinsic ISB allows for DMI between Mn atoms. The calculated magnetic moment of MBST is $5\mu_B$ per unit cell, indicating that Mn atom has a high spin configuration. Furthermore, we demonstrate the dynamic and thermal stability of MBST by calculating the phonon dispersions [see Fig. 6.1], elucidating absence of imaginary frequency in Brillouin zone, and *ab initio* molecular dynamic simulations (AIMD) [see Fig. 6.2]. Notably, similar ferroelectric heterostructures, such as WS₂/In₂Se₃ and WSe₂/In₂Se₃, have been successfully fabricated in experiments by dry transfer methods [254, 255], and Janus monolayers of transition metal dichalcogenides, i.e., MoSSe and PtSSe, can be synthesized by controlling the reaction atmosphere [256, 257]. These results highlight the possibility of construction of MBST/In₂Se₃ HS in experiments.

In₂Se₃ monolayer is a 2D vdW material with room-temperature FE [258] and small lattice mismatch with MBST [259], and its crystal structure is shown in Fig. 6.7(b). One can see that the In₂Se₃ monolayer consists of five triangular atomic layers stacked in sequence of Se-In-Se-In-Se, and the asymmetric position of Se atoms in central layer gives rise to the IP and OOP polarizations simultaneously. When In₂Se₃ is used as substrate to construct HS with MBST, the reversal of OOP polarization in In₂Se₃ monolayer can induce distinct interfacial coupling, further resulting in the variation of magnetic properties of MBST. Next, we consider twelve possible stacking configurations of MBST/In₂Se₃ HS [see Fig. 6.3]. We find that the most stable configuration is the outmost Te and Bi atoms of MBST sitting at the hollow and top-In sites of In₂Se₃ respectively, for both polarized-up (P↑) and -down (P↓)

states, and their side views are shown in Fig. 6.7(c). The equilibrium interlayer distance of MBST/P \uparrow and P \downarrow are 2.93 and 2.74 Å, respectively. The total energy of MBST/P \uparrow is higher by 0.053 eV/u.c. than MBST/P \downarrow , due to the weaker interfacial coupling between MBST and In₂Se₃ with upward polarization. The electric polarization for MBST/P \uparrow and MBST/P \downarrow HS is 0.073 and -0.081 eÅ/u.c., respectively, and the magnitude of that of In₂Se₃ monolayer is 0.096 eÅ/u.c., which implies that the ferroelectricity of HS mainly comes from In₂Se₃. Based on the climbing-image nudged elastic band method (CI-NEB), we obtain that energy barrier of ferroelectric phase transitions of In₂Se₃ is 0.083 eV. Recent experiments have demonstrated that an OOP field around 1 V/nm can overcome a such barrier and flip the OOP polar order [260]. Therefore, it can be expected that a similar electric field is large enough for realizing the reversal of polar orientation of MBST/In₂Se₃ HS.

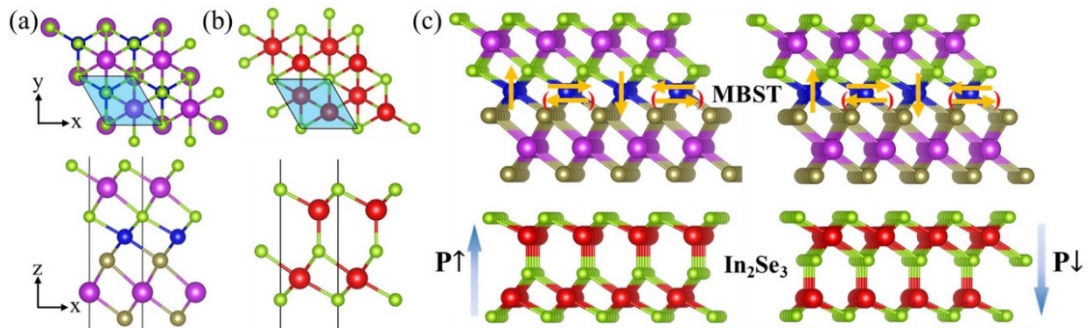


Fig. 6.7 Top and side views of the crystal structure of (a) MBST and (b) In₂Se₃. (c) Side views of MBST/P \uparrow and MBST/P \downarrow heterostructures (HSs). Green, purple, blue, brown, and red balls represent Se, Bi, Mn, Te, and In elements, respectively. The orange vectors in (c) indicate two spin configurations with opposite chirality used to extract the in-plane DMI strength.

6.3.2 Ferroelectric polarization controlled magnetic parameters

To investigate magnetic properties of systems, we adopt the following spin Hamiltonian:

$$H = -J \sum_{\langle i,j \rangle} \mathbf{S}_i \cdot \mathbf{S}_j - K \sum_i (S_i^z)^2 - \sum_{\langle i,j \rangle} \mathbf{D}_{ij} \cdot (\mathbf{S}_i \times \mathbf{S}_j) - \mu_{Cr} B \sum_i S_i^z, \quad (6.3)$$

where \mathbf{S}_i is a unit vector representing local spin of the i th Mn atom, and $\langle i, j \rangle$ represents summation of all nearest-neighboring (NN) Mn pairs. J , K , and \mathbf{D}_{ij} represent the Heisenberg exchange coupling, magnetic anisotropy and DMI, respectively. Their values of MBST and MBST/In₂Se₃ HS are shown in Table 6.1. We adopt the sign convention that $J > 0$ ($J < 0$) represents the FM (AFM) coupling, $K > 0$ ($K < 0$) indicates PMA (IMA), and $d_{\parallel} > 0$ ($d_{\parallel} < 0$) favors clockwise (anticlockwise) spin configuration. We first give the NN exchange coupling for magnetization along positive directions of x , y , and z axis, i.e., J_{xx} , J_{yy} , and J_{zz} . The SOC effects are taken into account. One can see that the exchange coupling of MBST is ferromagnetic, and J_{xx} , J_{yy} , and J_{zz} are almost identical, which indicates that the exchange coupling for MBST is nearly isotropic. Accordingly, we define an isotropic parameter J as the average of J_{xx} , J_{yy} , and J_{zz} , which represents the coefficient in normally used $-J \sum_{\langle i,j \rangle} \mathbf{S}_i \cdot \mathbf{S}_j$ term. We also notice that the magnitude of J of MBST is 1.658 meV, which is obviously larger than $J = 0.922$ meV when SOC is not considered. Therefore, the SOC effects can't be neglected in calculations of exchange coupling for MBST systems. The FE substrate does not change the type of exchange coupling of MBST, and J of MBST/P \uparrow (P \downarrow) is 1.315(1.638) meV. The effective anisotropy K_{eff} contains two parts: magnetocrystalline anisotropy K_{MCA} and magnetic shape anisotropy K_{MSA} , where the first part arises from SOC and second part is caused by magnetostatic dipole-dipole interaction; i.e., $K_{\text{eff}} = K_{\text{MCA}} + K_{\text{MSA}}$. One can see that MBST, MBST/P \uparrow and MBST/P \downarrow all have positive K_{MCA} . Interestingly, the K_{MCA} of HS is significantly enhanced from 0.006 to 0.287 meV when polarization direction of In₂Se₃ is tuned from up to down. Contrary to K_{MCA} , K_{MSA} favors the IP alignment of magnetization and basically not changes in three systems. For MBST and MBST/P \uparrow , K_{MSA} reaches to -0.205 and -0.204 meV, respectively, whose magnitude

are much larger than K_{MCA} . Therefore, K_{eff} are negative for both MBST and MBST/P \uparrow . However, due to the giant enhancement of K_{MCA} , K_{eff} in MBST/P \downarrow becomes positive. Therefore, the IMA-to-PMA transition is achieved in HS by FE modulation. The transition also indicates that it is very important to investigate K_{MSA} in calculations of magnetic anisotropy for magnetic thin films. We also test the influence of U_{eff} on magnetic anisotropy and find that IMA-to-PMA transition induced by FE reversal is robust to U_{eff} in the range of 2 to 5 eV [see Table. 5.2]. Moreover, we find that MBST, MBST/P \uparrow and MBST/P \downarrow all process sizable DMI reaching to 0.307, 0.323, and 0.217 meV, respectively. We further calculate the layer-resolved SOC energy difference ΔE_{soc} between the opposite chiral spin configurations [see Fig. 6.8]. For MBST/In₂Se₃ HS, the DMI still comes from MBST layer. The Mn layer basically does not contribute to the DMI strength, whereas the most adjacent Te and Bi layers provide dominant contribution, which means that the spin tilting is caused by spin-orbit scattering from heavy elements [47].

Table 6.1 Calculated nearest-neighboring (NN) exchange coupling J , magnetocrystalline anisotropy K_{MCA} , magnetic shape anisotropy K_{MSA} , effective anisotropy K_{eff} , and IP DMI component d_{\parallel} of MBST, MBST/P \uparrow and MBST/P \downarrow in units of meV.

	J_{xx}	J_{yy}	J_{zz}	J	K_{MCA}	K_{MSA}	K_{eff}	d_{\parallel}
MBST	1.657	1.650	1.668	1.658	0.045	-0.205	-0.160	0.307
MBST/P \uparrow	1.323	1.318	1.304	1.315	0.006	-0.204	-0.198	0.323
MBST/P \downarrow	1.626	1.627	1.662	1.638	0.287	-0.203	0.084	0.217

Table 6.2 K_{MCA} , K_{MSA} , and K_{eff} of HS with $U_{\text{eff}} = 2/4/5$ eV.

U_{eff}	MBST/P \uparrow			MBST/P \downarrow		
	K_{MCA}	K_{MSA}	K_{eff}	K_{MCA}	K_{MSA}	K_{eff}
2	0.008	-0.198	-0.190	0.340	-0.197	0.143
4	0.015	-0.209	-0.194	0.250	-0.209	0.041
5	0.024	-0.214	-0.190	0.230	-0.214	0.016

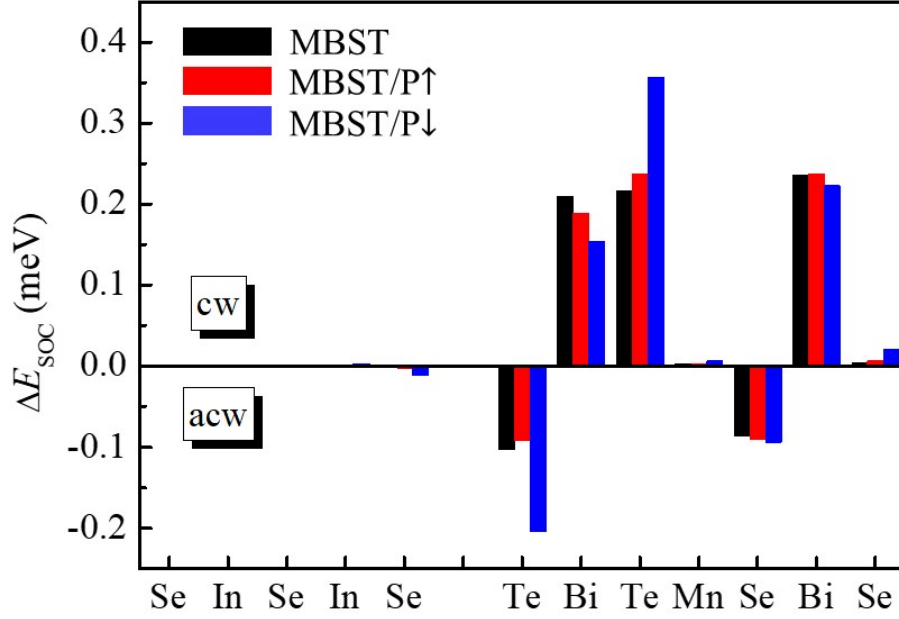


Fig. 6.8 Layer-resolved localization of the SOC energy difference ΔE_{soc} between opposite chiral spin configurations in MBST (black bar) monolayer, MBST/P \uparrow (red bar) and MBST/P \downarrow (blue bar) HSs.

6.3.3 Ferroelectric polarization controlled topological magnetism

Once magnetic parameters are obtained, we perform atomistic spin model simulations by using VAMPIRE in square geometry with a side length of 60 nm. In all simulations, the periodic boundary is used along x and y axes, and the initial magnetization state is set to random. The magnetic topology of spin textures can be defined by the topological charge: $Q = \frac{1}{4\pi} \int \mathbf{m} \cdot (\partial_x \mathbf{m} \times \partial_y \mathbf{m}) dx dy$, where \mathbf{m} is the normalized magnetization. Both skyrmion and bimeron can be attributed to $Q = \pm 1$, and the sign of Q determines the orientation of transverse motion of these topological quasiparticles in skyrmion Hall effect. Fig. 6.9 shows spin textures of MBST, MBST/P \uparrow , and MBST/P \downarrow . For pristine MBST, the loops of vortices and antivortices appear [see Fig. 6.6 and Fig. 6.9(a)], which arises from the competition between DMI and weak IMA [261]. By applying an IP magnetic field along positive direction of x axis ($B \rightarrow$), the vortex-antivortex pairs generate and become ordered along the direction of external field [see Fig. 6.10(a)]. Interestingly, the bimeron soliton with

diameter of around 9 nm emerge [see Fig. 6.9(b)] while $B \rightarrow$ increases to 60 mT. Compared with MBST, denser loops of vortices and antivortices emerge [see Fig. 6.9(c)] in MBST/P \uparrow , since the ferromagnetic exchange coupling is weaker. Moreover, loops in MBST/P \uparrow can also be transformed into bimeron solitons gradually via enhancing IP magnetic field [see Fig. 6.9(d) and 6.10(b)]. Due to the same outer magnetization, bimerons with opposite topological charges ($Q = \pm 1$) can coexist.

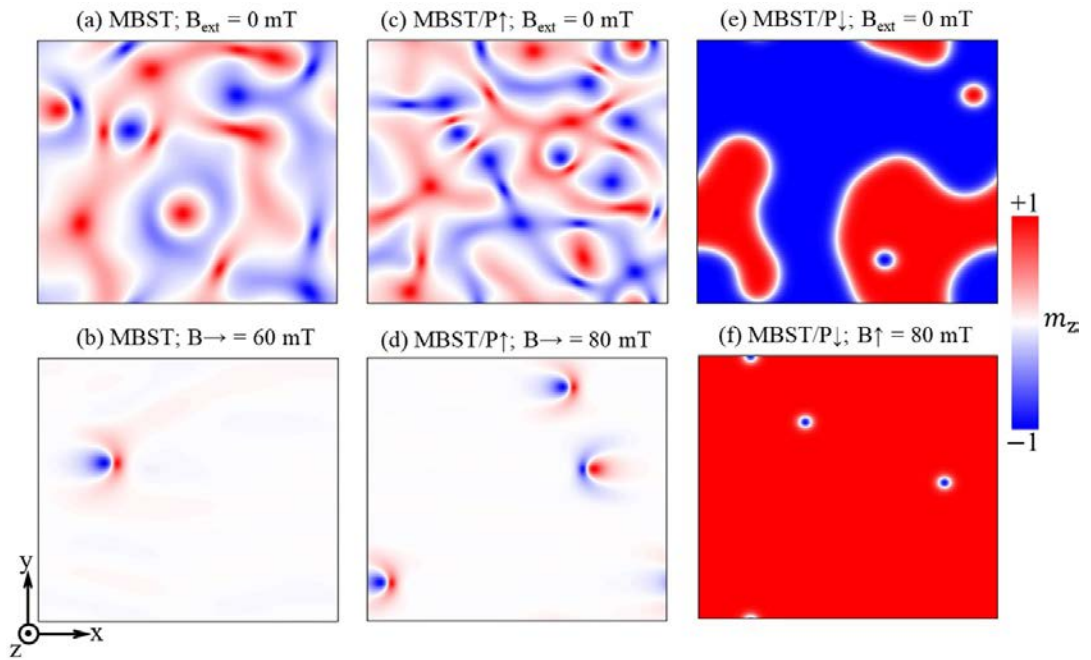


Fig. 6.9 The spin textures for MBST monolayer, MBST/P \uparrow and MBST/P \downarrow HSs in real space. Corresponding external fields are labeled above each panel. The color map indicates the out-of-plane (OOP) spin component of Mn atoms.

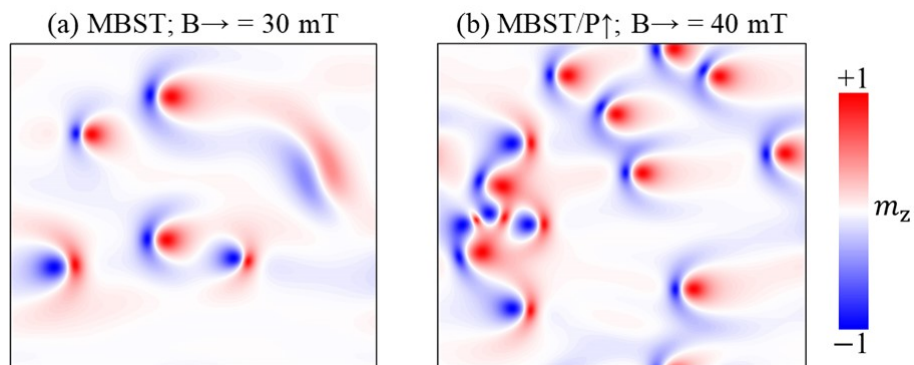


Fig. 6.10 Spin textures of (a) MBST monolayer under in-plane (IP) magnetic field of 30 mT and (b) MBST/P \uparrow HS under IP magnetic field of 40 mT.

The reversal of electric polarization in In₂Se₃ from up to down tunes magnetic anisotropy of HS from IP to OOP while the DMI slightly decreases, which indicates that there is obvious variation of topological magnetism. For 2D magnets processing hexagonal lattice, it is convenient to introduce the dimensionless parameter, $\kappa = \left(\frac{4}{\pi}\right)^2 \frac{2JK_{eff}}{3d_{\parallel}^2}$ [262-264]. Notably, κ is independent of the magnet thickness but only determined by the magnetic parameters, i.e., J , K_{eff} , and d_{\parallel} , which are directly obtained from first-principles calculations. When $0 < \kappa < 1$, the magnetic ground state of system exhibits spin spiral, whereas for $\kappa > 1$, the isolated skyrmion could be generated in the background of ferromagnetism. For MBST/P \downarrow , κ is 3.15 which is close to the critical value ($\kappa = 1$) of transition to the spiral state. Therefore, isolated skyrmions are hopefully be stabilized. Atomistic spin model simulations demonstrate that the multiple Néel-type skyrmions with diameter of around 4 nm appear in MBST/P \downarrow [see Fig. 6.9(e)] under zero magnetic field. We thus obtained the FE-controlled topological magnetic structures in MBST/In₂Se₃ HS. The distinct chiral spin textures in MBST/P \uparrow and MBST/P \downarrow are potentially used as “0” and “1” bit carriers for realizing the binary data encoding and storage. Strikingly, the size of skyrmion in MBST/P \downarrow is very small, which can largely enhance the integration level of corresponding devices. The skyrmions with opposite topological charges ($Q = \pm 1$) appear at distinct domains, and applying an 80 mT OOP magnetic field along positive direction of z axis ($B\uparrow$) to shrink the blue domain, the skyrmions with $Q = +1$ are annihilated [see Fig. 6.9(f)].

6.3.4 The mechanism of magnetic anisotropy variation

Since the FE-controlled magnetic phase transition is dominantly caused by large variation of MCA, we elucidate the physical mechanism of MAE of MBST/In₂Se₃ HS. From layer-resolved MAE [see Fig. 6.11(a)], one can find that the MAE of HS just comes from MBST, and the PMA of Te which is adjacent to Mn atom is enhanced significantly while polarization of In₂Se₃ reverses, which responds for K_{MCA} increasing. For further understanding MAE change of Te atom, we calculate the MAE from orbital hybridization as shown in Fig. 6.11(b) and (c). One can see that the hybridization between p_y and p_z provides IMA, while hybridization between p_y and p_x gives rise PMA. The PMA contribution arises from p_y and p_x is obviously increased when polarization direction of In₂Se₃ reverses from up to down. Moreover, we analyze the MAE change sourcing from $5p$ orbitals of Te based on second-order perturbation theory. MAE can be expressed as Eq. 2.1 where the difference of SOC elements is given in Table. 2.2. Fig. 6.11(d) and (e) show the projected density of states (pDOS) for Te. One can see that spin-up occupied $p_{x(y)}$ states ($p_{x(y)}^{o+}$) shift across the Fermi level (E_F) for HS with P↓, which is indicated by dashed black arrow in Fig. 6.11(e). The difference of SOC elements between $p_{x(y)}^{o+}$ and spin-up unoccupied $p_{y(x)}$ ($p_{y(x)}^{u+}$) is 1 [see Table. 2.2], which responds for PMA coming from p_x and p_y hybridization. The shift of $p_{x(y)}^{o+}$ means that the value of $(E_u^{\sigma'} - E_o^{\sigma})$ obviously decreases. Therefore, the positive MAE from p_x and p_y hybridization enhances. It is also found that peaks of spin-up and spin-down occupied p_z states (p_z^{o-} and p_z^{o+}) are close to each other. Since SOC elements difference of p_y^{u+} , p_z^{o-} and p_y^{u+} , p_z^{o+} have opposite signs and same amplitudes [see Table. 2.2], the MAE contribution from p_y and p_z barely changes. The fact that FE reversal-induced PMA enhancement is due to the shift of electronic states of Te inspires us to further investigate the interlayer charge transfers of HS. Bader analysis shows that the transferred charge from MBST to In₂Se₃ obviously increases from 0.019 to 0.049e

when FE polarization is reversed from up to down, resulting in occupied states of MBST shifting across E_F [see Fig. 6.11(e)]. Furthermore, the planar-average charge density difference [see Fig. 6.12] clearly shows that charge transfers are mainly restricted in the interface of MBST/P \uparrow but spreads over all In_2Se_3 layer for MBST/P \downarrow [265], which is consistent with charge transfer analysis.

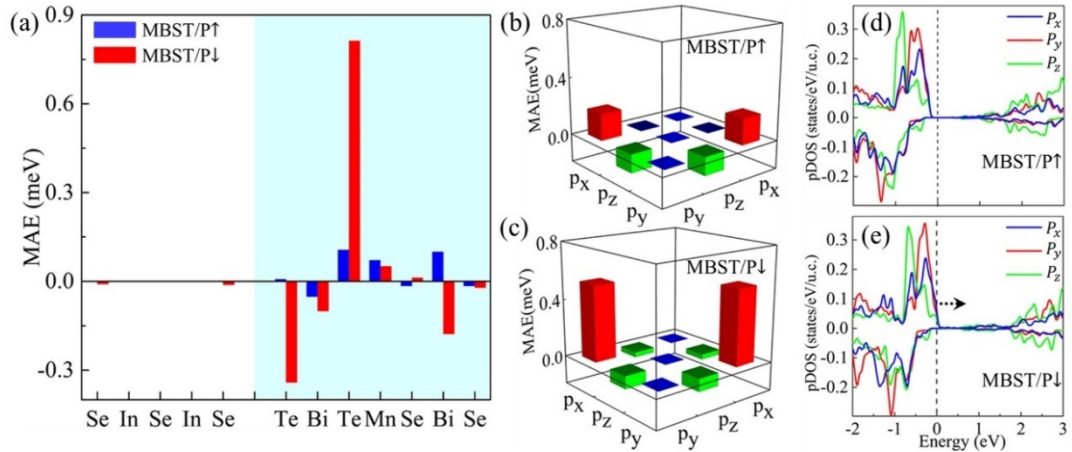


Fig. 6.11 (a) layer-resolved MAE of MBST/P \uparrow and MBST/P \downarrow HSs. (b), (c) MAE coming from 5p orbitals hybridization, and (d), (e) projected density of states of Te which is adjacent to Mn atom in MBST/ In_2Se_3 HS.

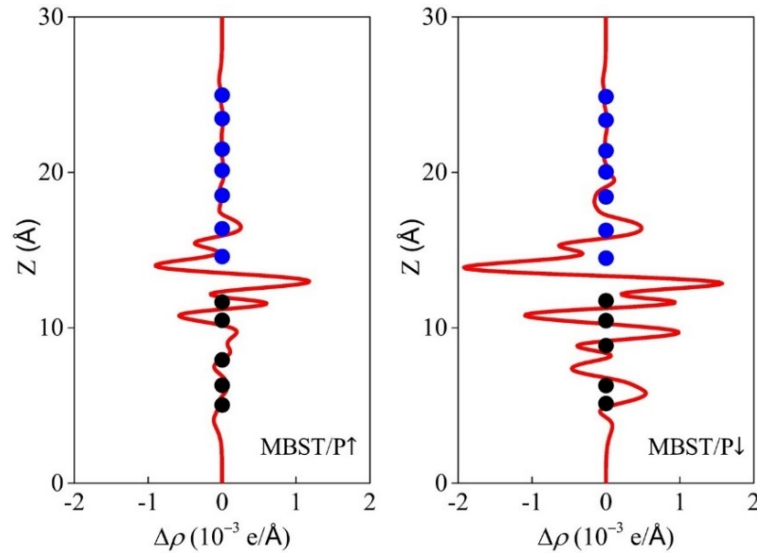


Fig. 6.12 Planar-average charge density difference of MBST/P \uparrow (left panel) and MBST/P \downarrow (right panel) HSs. The blue and black dots represent the positions of MBST and In_2Se_3 atoms, respectively.

6.3.5 Electronic band structures

The obvious charge redistribution in MBST/In₂Se₃ HS and strong SOC of MBST layer arising from Bi and Te elements inspire us to further investigate band structures of this HS under different polarization and spin directions. Here, we consider four configurations, namely, P↑M→, P↑M↑, P↓M→, and P↓M↑ [here, P↑(↓) represents ferroelectric polarization of In₂Se₃ directs up(down); M→(↑) represents magnetic moment of MBST along positive direction of *x*(*z*) axis]. For P↑M→ configuration, the HS is a semiconductor with an indirect bandgap of 0.197 eV [see Fig. 6.13(a)]. Strikingly, indirect-to-direct bandgap transition is induced when magnetization rotates from IP to OOP. Compared with P↑M→, the VBM of P↑M↑ is shifted to Γ point and the bandgap thus becomes direct [see Fig. 6.13(b)]. Also, the magnitude of bandgap is effectively tuned to 0.023 eV. Interestingly, the VBM and CBM of P↑M→ and P↑M↑ are only occupied by spin-up electrons, which indicates that the system can be turned to half metal by a slight hole or electron doping. When FE polarization of In₂Se₃ reverses, the band gap is closed in HS with P↓M→, and P↓M↑ [see Fig. 6.13(c) and (d)]. We thus obtained semiconductor-to-conductor transition induced by FE reversal.

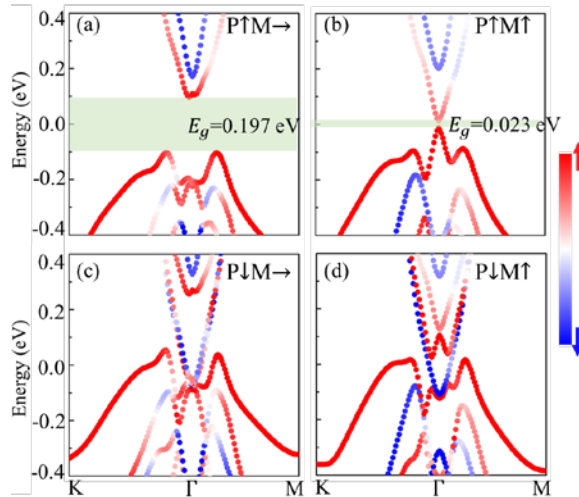


FIG. 6.13 Spin-resolved band structures for (a) P↑M→, (b) P↑M↑, (c) P↓M→, and (d) P↓M↑ configurations. Red and blue colors indicate the spin-up and -down states, respectively.

Notably, the HS is a two-dimensional system with atomic thickness, which indicates that electrons are confined in slab and nonconductive at OOP direction. Despite the HS with down-polarized state is metallic, the OOP ferroelectricity of HS can be switched by the vertical electric field. This is similar to the idea of electrical field-controlled ferroelectricity reversal in 2D hyperferroelectric metal [266] and thin film of the 3D polar metals [267, 268].

6.4 Summary

In summary, using first-principles calculations and atomistic spin model simulations, we demonstrate that by modulating FE polarization of MBST/In₂Se₃ HS, the IMA-to-PMA transition is achieved, resulting in that loops of vortices and antivortices are transformed into skyrmions with diameter of only 5 nm. Furthermore, the loops in MBST/P↑ can be turned to bimeron solitons via applying IP magnetic field. Detailed analysis elucidates that charge transfers between MBST and In₂Se₃ play a crucial role in determining magnetic anisotropy of HS. When the FE polarization is reversed from up to down, the $p_{x(y)}^{o+}$ states of Te which is adjacent to Mn shifts across the E_F due to the increase of interlayer transferred charge, resulting in large enhancement of PMA contribution from Te. The high tunability of topological magnetism is promising to be applied in nonvolatile information handling with low-power consumption. Since the effect is robust, more nontrivial phenomena of controlling of topological magnetism can be expected in HSs consisting of Janus magnets and ferroelectric/antiferroelectric substrate.

Chapter 7 Anisotropic Dzyaloshinskii-Moriya interaction and anti-topological magnetism in two-dimensional magnets

7.1 Introduction

In chapter 4 and 5, we show that FM skyrmion, bimeron and chiral DWs can be established by isotropic DMI at 2D polar magnets, such as Janus monolayers, and 2D magnets-based heterostructure. Notably, these systems all possess C_{nv} point group. However, the anisotropic DMI and AFM topological spin textures haven't been reported in pure 2D magnets so far. Anisotropic DMI favors the formation of anti-topological magnetism, such as antiskyrmion which is a distinct type of skyrmion besides Bloch and Néel type, whose Hall angle can be directly controlled by the orientation of drive current [269-274]. In AFM systems, magnetic moments of coupled sublattices cancel out, resulting in zero dipolar field and enhances the stability of topological magnetism, at the same time, the topological charge of coupled sublattices also cancel out, resulting in zero skyrmion Hall angle and high mobility [275, 276]. Notably, experiments have shown that X-ray photoemission electron microscopy and spin-polarized scanning tunneling microscopy can unveil AFM spin configurations [277, 278]. In a general perspective, Anti- and AFM topological spin textures are highly promising for applications in advanced spintronic devices.

In this chapter, we show missing blocks for topological magnetism in 2D magnets. We propose non-polar AX_2 monolayer with $P\bar{4}m2$ layer group for realizing crystal symmetry protected anisotropic DMI, where A is 3d transition metal, and X is VI-A or VII-A element. Using first-principles calculations, we demonstrate that anisotropic DMI can be obtained in this family of 2D magnets, and due to the increasing of occupied 3d electrons, FM phases are turned to be AFM phases when A varies from V to Ni. Moreover, using atomistic spin model, we reveal that various

chiral spin configurations, including FM chiral DWs/antiskyrmion and AFM chiral DWs/antiskyrmion/vortex-antivortex pair, can be achieved in those AX₂ systems.

7.2 Methodology

All our first-principles calculations are performed with the Vienna *Ab Initio* Simulation Package (VASP), based on the density functional theory (DFT). For describing the strongly correlated 3*d* electrons, the GGA+U method is applied, where U_{eff} is set to 3 eV, a typical value for 3*d* transition metal. Other U_{eff} values are also tested ($U_{eff} = 2, 4$ eV). We find that the anisotropic DMI in AX₂ monolayer is robust to U_{eff} values. The projector-augmented wave (PAW) method is adopted, and the cutoff energy for plane wave expansion is set to 420 eV. Γ -center k -point mesh is set to 24×24×1 for sampling the Brillouin zone. The convergence criteria of total energy is set to 10⁻⁷ eV. All structures are fully relaxed until Hellmann-Feynman force acting on each atom is less than 10⁻³ eV/Å. A vacuum space of at least 15 Å is adopted in periodical direction for avoiding the interactions between adjacent layers.

For obtaining the NN and NNN exchange coupling (J_1 and J_2), we compare DFT total energies difference of FM, G-type AFM and Stripe-type AFM states of a 2×2×1 supercell. The total energies of these three spin configurations are given by:

$$E_{FM} = -8J_1 - 8J_2 + E_{other}; \quad (7.1)$$

$$E_{G-AFM} = 8J_1 - 8J_2 + E_{other}; \quad (7.2)$$

$$E_{S-AFM} = 8J_2 + E_{other}. \quad (7.3)$$

Accordingly, J_1 and J_2 are written as:

$$J_1 = \frac{E_{G-AFM} - E_{FM}}{16}; \quad (7.4)$$

$$J_2 = \frac{2E_{S-AFM} - E_{G-AFM} - E_{FM}}{32}. \quad (7.5)$$

The chirality-dependent energy difference (CDED) approach and qSO method are used for calculations of DMI. Since CDED approach for determining DMI has been detailly discussed in above two chapter, we only introduce the qSO method in following discussion. In qSO method, 2D magnets are well described by atomic extended spin Hamiltonian:

$$H = -\sum_{\langle i,j \rangle} J_{ij} \mathbf{m}_i \cdot \mathbf{m}_j - K \sum_i (m_i^z)^2 - \sum_{\langle i,j \rangle} \mathbf{D}_{ij} \cdot (\mathbf{m}_i \times \mathbf{m}_j), \quad (7.6)$$

where \mathbf{m}_i and \mathbf{m}_j are the unit magnetization vector at position \mathbf{r}_i and \mathbf{r}_j respectively. To calculate the in-plane (IP) component of \mathbf{D}_{ij} , we study the DFT energy of a noncollinear homogenous spin spiral $\mathbf{m} = (\sin(\mathbf{q} \cdot \mathbf{r}), 0, \cos(\mathbf{q} \cdot \mathbf{r}))$, where \mathbf{q} represents spin spiral vector. Based on the atomic extended spin Hamiltonian, the system energy functional of \mathbf{q} is written as:

$$E(\mathbf{q}) = -\sum_{\langle i,j \rangle} J_{ij} \cos(\mathbf{q} \cdot (\mathbf{r}_j - \mathbf{r}_i)) - K \sum_i (\cos(\mathbf{q} \cdot \mathbf{r}_i))^2 + \sum_{\langle i,j \rangle} D_y \sin(\mathbf{q} \cdot (\mathbf{r}_j - \mathbf{r}_i)), \quad (7.7)$$

Therefore, the DMI related energy $\Delta E_{DM}[\mathbf{q}]$ can be expressed as:

$$\Delta E_{DM}[\mathbf{q}] = (E[\mathbf{q}] - E[-\mathbf{q}])/2 = \sum_{\langle i,j \rangle} D_y \sin(\mathbf{q} \cdot (\mathbf{r}_j - \mathbf{r}_i)), \quad (7.8)$$

where $D_y > 0$ ($D_y < 0$) favors ACW (CW) spin configurations. When \mathbf{q} is along $\Gamma - M$ or $\Gamma - M'$ of $\sqrt{2} \times \sqrt{2} \times 1$ supercell and its magnitude q is close to 0 or $\pm \frac{\sqrt{2}}{2}$, we have the relationship $\Delta E_{DM}[q] = (E[q] - E[-q])/2 \propto D_y q$. We note that spin spirals propagate along the NN magnetic atoms as displayed by inset of Fig. S1(a). The d_{\parallel} can be calculated as: $d_{\parallel} = \frac{D_y}{2r}$, where r represents the lattice constant of supercell. For calculating $E[\mathbf{q}]$, we employ the generalized Bloch theorem and treat SOC as the first-order perturbation. And in order to include SOC effects in a self-consistent way, the full SOC operator is replaced by its component along the rotation axis of spiral, which is H_{soc}^y in our calculations. We perform qSO method in conjunction with VASP package [279].

7.3 Results and discussion

7.3.1 Anisotropic DMI and exchange coupling

Fig. 7.1(a)-(c) show the crystal structure of AX_2 monolayer. Each A atom is tetrahedrally surrounded by four X ligands. The layer group of AX_2 is $P\bar{4}m2$ which lacks inversion symmetry. From side views of AX_2 in Fig. 7.1(b) and (c), one can see that an X atom bonding with two A atoms along x and y directions are in bottom and top layer, respectively.

To investigate magnetic properties of our systems, we adopt following spin Hamiltonian:

$$H = -J_1 \sum_{\langle i,j \rangle} \mathbf{S}_i \cdot \mathbf{S}_j - J_2 \sum_{\langle i',j' \rangle} \mathbf{S}_{i'} \cdot \mathbf{S}_{j'} - K \sum_i (S_i^z)^2 - \sum_{\langle i,j \rangle} \mathbf{D}_{ij} \cdot (\mathbf{S}_i \times \mathbf{S}_j), \quad (7.9)$$

where \mathbf{S}_i is unit vector indicating local spin of the i th A atom. $\langle i, j \rangle$ and $\langle i', j' \rangle$ represent summation of all the NN and NNN A pairs, and J_1 and J_2 represent the NN and NNN exchange coupling, respectively. K refers to the magnetic anisotropy. We first discuss DMI vector in AX_2 monolayer, \mathbf{D}_{ij} , which is the key parameter in this work. $P\bar{4}m2$ layer group contains two mirror symmetries M_x and M_y . According to Moriya symmetry (MS) rules [44, 45], due to the existence of mirror plane across the middle of NN A-A bonds, the \mathbf{D}_{ij} has the form as: $\mathbf{D}_{ij} = d_{\parallel}(\mathbf{u}_{ij} \times \mathbf{z}) + d_{ij,z}\mathbf{z}$, where \mathbf{u}_{ij} is the unit vector between sites i and j , and \mathbf{z} is the out-of-plane (OOP) unit vector. A-X-A triplet coordinates in one mirror plane of AX_2 , which results in that OOP component of DMI component $d_{ij,z}$ vanishes required by symmetry feature. Due to the rotoreflection S_{4z} in $P\bar{4}m2$, the sign of in-plane (IP) DMI components should be opposite for \mathbf{u}_{ij} along x and y direction ($\mathbf{u}_{ij,x}$ and $\mathbf{u}_{ij,y}$). Therefore, \mathbf{D}_{ij} between the NN A atoms in $x(y)$ direction can be expressed as: $\mathbf{D}_{ij,x(y)} = d_{\parallel}^{x(y)}(\mathbf{u}_{ij,x(y)} \times \mathbf{z})$, where $d_{\parallel}^x = -d_{\parallel}^y$, thanks to the crystal symmetry protection. The orange arrows in Fig. 1(a) illustrate one possible configuration of \mathbf{D}_{ij} of AX_2 monolayer. For both FM and AFM magnetic orders, this assumptive anisotropic DMI could favor ACW and CW spin spiral for an atomic chain along x and y direction, respectively. Another possible configuration of \mathbf{D}_{ij} is that all DMI vectors have opposite orientation compared with that shown in Fig. 7.1(a).

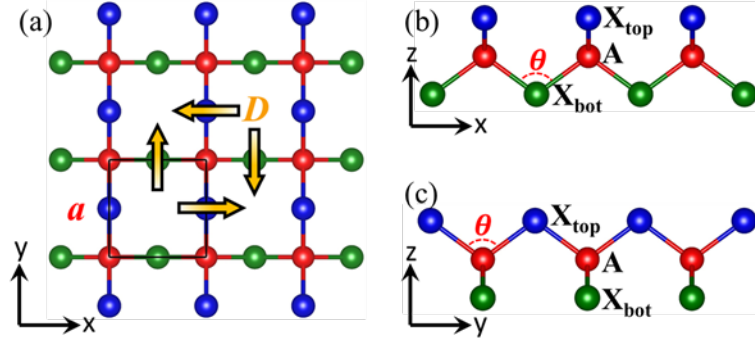


Fig. 7.1. (a) Top view and (b, c) side views of AX_2 monolayer. Red and blue/green balls represent magnetic and nonmagnetic elements respectively. The inset orange arrows of top view indicate the orientation of in-plane component of DMI between nearest-neighboring (NN) magnetic atoms. This DMI could favor the anticlockwise (ACW) and clockwise (CW) spin spiral along a chain of atoms in x and y direction, respectively.

The magnetism of most discovered 2D magnets, such as VSe_2 , CrI_3 , $CrGeTe_3$, $MnSe_2$ and Fe_3GeTe_2 , originates from partially occupied $3d$ orbitals. Accordingly, we choose A in AX_2 monolayer as magnetic elements V, Cr, Mn, Fe, Co, and Ni. Under tetrahedral crystal field, d orbitals split into d_{xy} , d_{xz} , d_{yz} orbitals (t_2) with high energy level and $d_{x^2-y^2}$, d_{z^2} orbitals (e) with low energy level. Among 366 candidates containing $3d$ transition metal (range from V to Ni) in the open Computational 2D Materials Database C2DB [280, 281], we screen out 23 2D magnets satisfying AX_2 formula and structural conditions to realize anisotropic DMI. We first give the DFT results about basic structure and magnetism properties of AX_2 family as shown in Table 7.1. We adopt the sign convention that $J > 0$ ($J < 0$) indicates the FM (AFM) coupling, and $K > 0$ ($K < 0$) indicates OOP (IP) magnetic anisotropy. In most AX_2 monolayers, the magnitudes of J_1 are much larger than that of J_2 . Interestingly, J_1 are always FM for V and Cr compounds while turn to be AFM for Mn, Fe, Co and Ni compounds (exception for MnS_2). In tetrahedral crystal, $t_2 \leftrightarrow p \leftrightarrow e$ superexchange allows FM coupling, however, the $t_2 \leftrightarrow t_2$ and $e \leftrightarrow e$ direct exchanges prefer AFM coupling, and the strength of $t_2 \leftrightarrow t_2$ is much larger than that

of $e \leftrightarrow e$ [282]. Therefore, when $3d$ orbitals are no less than half-filled, strong AFM exchange coupling emerges, which responds for the variation of J_1 of AX_2 monolayer. Similar transformation between FM and AFM phases is reported in zinc-blende binary transition metal compounds [282]. One can also see that Mn atoms in MnX_2 ($X = \text{Cl, Br, I}$) monolayers have the highest magnetic moment (close to $5 \mu_B$) which gradually decreases for chemical elements on both sides of Mn in $3d$ transition metal row of the periodic table. The magnetic moment indicates that Mn has a high spin configuration ($S = \frac{5}{2}$), and the magnetic moment decreases to about $1 \mu_B$ to $3 \mu_B$ in other $3d$ transition metals quantitatively follow the total spin number of $3d$ orbitals, which obeys the Hund's first rule. For AX_2 with a certain A, distinct $d \leftrightarrow p$ orbitals hybridization controlled by X induces the variation of specific value of magnetic moment. The result that Mn magnetic moment in MnS_2 is less than MnX_2 ($X = \text{Cl, Br, I}$) about $1 \mu_B$ implies that the $3d$ orbital is less than half-filled, responding for the FM exchange coupling.

Fig. 7.2 shows the calculated DMI of AX_2 family from CDED approach. We adopt sign convention that $d_{\parallel} > 0$ ($d_{\parallel} < 0$) favors ACW (CW) spin configuration. Notably, the anisotropic DMI ($d_{\parallel}^x = -d_{\parallel}^y$) is obtained in all AX_2 monolayers, which is consistent with previous analysis. Interestingly, the strength of DMI in some systems reach to several meV, e.g., VSe_2 (2.24 meV), FeS_2 (-2.85 meV) and NiI_2 (6.99 meV), which are comparable to many state-of-art ferromagnetic/heavy metal multilayers. Furthermore, to demonstrate the validity of results obtained from CDED approach, we perform qSO method where we consider SOC effects within first-order perturbation theory using self-consistent calculations to obtain $E(\mathbf{q})$. Here, $E(\mathbf{q})$ represents the energy functional of spin spiral in AX_2 monolayers where \mathbf{q} is spiral vector, and the DMI energy can be estimated by: $\Delta E_{DM}[\mathbf{q}] = (E[\mathbf{q}] - E[-\mathbf{q}])/2$ [see Methodology]. We choose VO_2 and $MnBr_2$ as examples for FM and AFM phase, respectively. The latter calculations demonstrate the emergence of anti-topological quasiparticle in these two systems. Fig. 7.3(a) shows asymmetric energy dispersion

$E[\mathbf{q}]$ of a $\sqrt{2} \times \sqrt{2} \times 1$ VO₂ supercell along $\Gamma - M$ and $\Gamma - M'$ directions in 2D BZ. These two high-symmetry directions in reciprocal space correspond for directions of the NN V pairs in real space [see inset of Fig. 7.3(a)]. For \mathbf{q} along $\Gamma - M$, ACW rotating spin spiral is favorable, while for \mathbf{q} along $\Gamma - M'$, CW rotating spin spiral becomes more favorable, demonstrating the anisotropic feature of DMI. Moreover, with calculated $\Delta E_{DM}[\mathbf{q}]$ showing good linear dependence on \mathbf{q} nearby the Γ point [see Fig. 7.3(b)], d_{\parallel}^x and d_{\parallel}^y can be determined to be 1.51 and -1.51 meV, respectively. The computational approaches of d_{\parallel} are given in Methods D. Different from VO₂, the lowest energy appears at M/M' point in MnBr₂ [see Fig. 7.3(c)] which corresponds for G-AFM phase. Interestingly, the chirality of preferred spin spiral keeps opposite in $\Gamma - M$ and $\Gamma - M'$ directions. From the linear fit of $\Delta E_{DM}[\mathbf{q}]$ nearby M point [see Fig. 7.3(d)], we obtain that d_{\parallel}^x and d_{\parallel}^y equal to -0.31 and 0.31 meV, respectively. These results indicate that the qSO method has good consistency with CDED approach about chirality and magnitude of DMI of AX₂ systems.

In order to further investigate the origin of DMI, we calculate the layer resolved SOC energy difference ΔE_{soc} between opposite chiral spin configurations. We find that ΔE_{soc} has opposite preferred chirality with spin rotating along x and y directions. Fig. 7.4 shows the ΔE_{soc} with spin rotating along x direction. For X atom with weak SOC, such as O, S and Cl, large part of contribution to DMI originates from A atom. When SOC strength of X enhances (X varies from Cl to I), the contribution to total DMI from X keeps increasing, and in most cases, X_{bot} gives more DMI contribution than X_{top}. This feature is consistent to Fert-levy model where A-X_{bot}-A can be considered as a noncentrosymmetric triplet. We also notice that for systems with small DMI, such as FeO₂ and NiBr₂, ΔE_{soc} from A layer and X layer has similar magnitude but opposite chirality, resulting in these contributions cancelling each other.

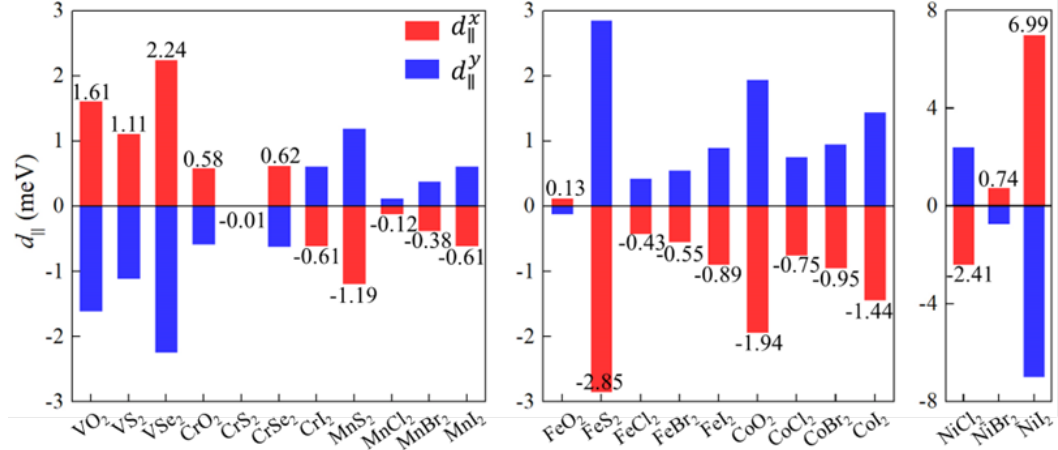


Fig. 7.2. The calculated in-plane component of DMI for 23 AX₂ monolayers. Red and blue bars represent the DMI between NN magnetic atoms at x and y directions respectively. Here $d_{||} > 0$ ($d_{||} < 0$) favors spin canting with ACW (CW) chirality. It is noted that $d_{||}^x = -d_{||}^y$ in all systems, which demonstrates the anisotropic feature of DMI in AX₂. We give specific values of $d_{||}^x$ as shown by numbers of red bars.

For AX₂ system, there are two two-fold rotation axes (C_2) passing through NNN A atoms and perpendicular to each other. Based on MS rules, DM vectors between the NNN magnetic atoms should be along directions connecting these atoms, which favor helicoid spin propagations with opposite chirality. However, the magnitude of NNN DMI (d_{NNN}) is very tiny compared with the NN DMI. For example, using four-state energy mapping method, we find that d_{NNN} of VO₂ is only 0.041 meV. Moreover, calculated spin textures (see latter discussions) show that despite the NNN DMI is neglected, the antiskyrmion with both helicoid and cycloid spin spiral appears in VO₂.

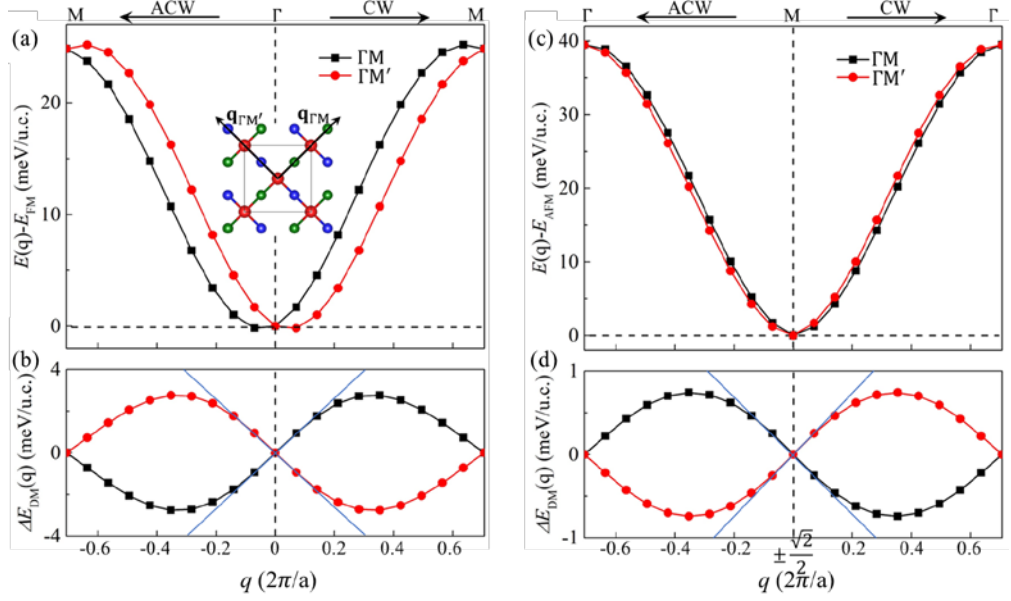


Fig. 7.3. Spin spiral energy $E(q)$ (upper panel) and DMI energy $\Delta E_{\text{DM}}(q)$ (lower panel) as functions of spiral vector length q for (a, b) VO_2 and (c, d) MnBr_2 . In VO_2 , $E(q)$ is given respect to the ferromagnetic state at $q = 0$ while in MnBr_2 , $E(q)$ is given respect to the antiferromagnetic state at $q = \pm\sqrt{2}/2$. Black and red points are calculated with q along $\Gamma - M$ and $\Gamma - M'$ respectively (see inset of a). Blue lines in (b) and (d) are linear fits of $\Delta E_{\text{DM}}(q)$, which is based on the atomistic extended spin Hamiltonian.

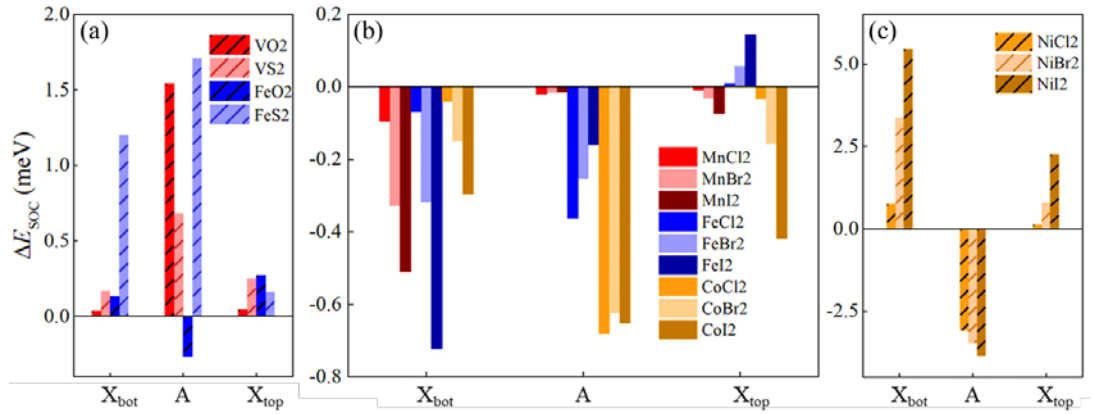


Fig. 7.4. Atomic-layer-resolved localization of SOC energy difference ΔE_{SOC} between opposite chiral spin configurations for (a) vanadium/iron dichalcogenides, (b) manganese/iron/cobalt dihalides and (c) nickel dihalides. Here we show ΔE_{SOC} with spin rotating along x direction.

7.3.2 Topological spin configurations

Once all magnetic parameters in spin Hamiltonian H are obtained, one can define the effective magnetic field $\mathbf{B}_{eff}^i = -\frac{1}{\mu_s} \frac{\partial H}{\partial \mathbf{S}_i}$ and perform time evolution of spin on each atomic site to investigate real-space spin configurations, using the Landau-Lifshitz-Gilbert (LLG) equation: $\frac{\partial \mathbf{S}_i}{\partial t} = -\frac{\gamma}{(1+\lambda^2)} [\mathbf{S}_i \times \mathbf{B}_{eff}^i + \lambda \mathbf{S}_i \times (\mathbf{S}_i \times \mathbf{B}_{eff}^i)]$, where γ indicates gyromagnetic ratio and is set to $1.76 \times 10^{11} \text{ T}^{-1} \text{ s}^{-1}$, and λ represents damping constant and is set to 0.2. In VO₂ monolayer, FM antiskyrmion with diameter of 10 nm [yellow dashed square in Fig. 7.5(a)] emerges. There are Néel walls appearing in x and y directions connecting with four Bloch lines; and IP magnetic moments are along radial direction of these Bloch lines [see Fig. 7.5(b)]. Using the formula $Q = \frac{1}{4\pi} \int \mathbf{S} \cdot (\partial_x \mathbf{S} \times \partial_y \mathbf{S}) dx dy$, the calculated magnetic topological charge Q is 1 for FM antiskyrmion in yellow dashed square. Due to the enhancement of FM exchange coupling and PMA, large size of domain separated by Néel DW appears in VS₂ and VSe₂ monolayers [see Fig. 7.6(a) and (b)].

In range from CrO₂ to MnCl₂ in Table 7.1, uniform FM and G-AFM phases are observed, which is a consequence of much stronger Heisenberg exchange coupling compared with DMI. Interestingly, an isolated AFM antiskyrmion emerges on the background of large-size domain in MnBr₂ [see Fig. 7.5(c)]. In the zoomed AFM antiskyrmion shown in Fig. 7.5(d), one can see that there are two opposite spin-dependent sublattices with AFM coupling and opposite Q (+1, -1). Despite Q for AFM antiskyrmion is zero, it is topologically protected since it cannot be destroyed or split into pieces. The diameter of this AFM antiskyrmion is only 6.8 nm, which can significantly enhance integration level of corresponding devices. There is an angle of 45° between orientations of Néel walls in FM and AFM antiskyrmion [see Fig. 7.5(b) and (d)]. This angle actually arises from the difference of chosen unit cell for FM systems ($1 \times 1 \times 1$) and AFM systems ($\sqrt{2} \times \sqrt{2} \times 1$) in atomistic spin model simulations. Compared with MnBr₂, the symmetric exchange coupling slightly

decreases while DMI largely increases in MnI_2 , which results in that AFM antiskyrmion is embedded in meandering domain [see Fig. 7.6(c)]. Notably, in CoI_2 , we observe the AFM vortex-antivortex pair [see Fig. 7.5(e) and (f)]. Similar to AFM antiskyrmion, the topological charge Q for both AFM vortex and antivortex is zero but topologically protected. For Ni-based systems, such as NiI_2 , high-density wormlike domains separated by chiral DWs are achieved due to significant DMI strength [see Fig. 7.6(g) and (h)]. Above scenarios clearly show that various FM/AFM anti-topological spin configurations are achieved in the family of AX_2 . Moreover, we demonstrate the dynamic stability of systems with chiral magnetism monolayer via phonon dispersions. Despite there is small acoustic imaginary mode nearby Γ point for VS_2 and CoBr_2 monolayers, this instability may not significantly affect the whole crystal structure and can be removed by ripples in structures. Experiments have shown that using molecular beam epitaxy (MBE), tetrahedral crystal in thin film form can be grown on the appropriate substrate [283, 284].

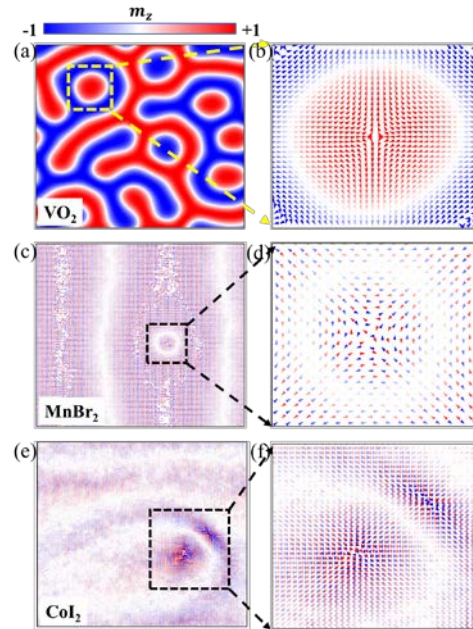


Fig. 7.5. Real-space spin configurations of a 60×60 nm square and zooms of anti-topological quasiparticle (indicated by the dashed square) of (a, b) VO_2 , (c, d) MnBr_2 and (e, f) CoI_2 monolayers. The color map indicates the out-of-plane spin component, and the arrows indicate the orientation of in-plane spin component.

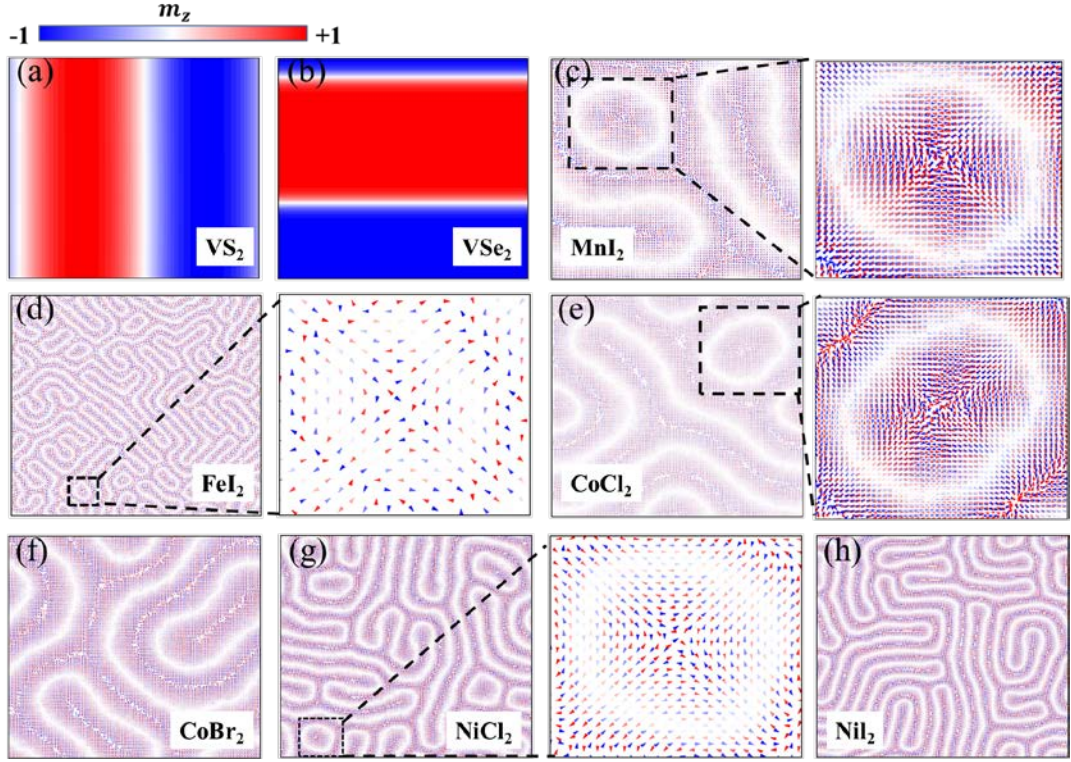


Fig. 7.6. Real-space spin configurations of 60×60 nm square and zooms of anti-topological quasi particle (dashed square) of (a) VS_2 , (b) VSe_2 , (c) MnI_2 , (d) FeI_2 , (e) CoCl_2 , (f) CoBr_2 , (g) NiCl_2 and (h) NiI_2 . Antiferromagnetic antiskyrmion embedded in meandering domain emerges in MnI_2 , FeI_2 , CoCl_2 and NiCl_2 , and only chiral domain walls are observed in VS_2 , VSe_2 , CoBr_2 and NiI_2 . The color map indicates the out-of-plane spin component, and the arrows indicate the orientation of in-plane spin component.

The DMI/NN exchange coupling ratios $|d_{\parallel}/J_1|$ of all AX_2 monolayers are calculated [see blue dots of Fig. 7.7]. One can see that $|d_{\parallel}/J_1|$ of VO_2 , FeI_2 and CoI_2 are 0.159, 0.192 and 0.118, respectively, which are in the typical range of 0.1-0.2 for the skyrmion formation. Since spin textures are determined by J , K and d_{\parallel} cooperatively, and K is neglected in $|d_{\parallel}/J_1|$, it is convenient to introduce another dimensionless parameter, $\kappa = |(\frac{4}{\pi})^2 \frac{2J_1K}{d_{\parallel}^2}|$, for systems with magnetic atom arranging in 2D square lattice. When $0 < \kappa < 1$, the magnetic ground state of system exhibits

spin spiral, whereas for $\kappa > 1$, the isolated skyrmion can be generated. The results for AX_2 are indicated by red dots in Fig. 7.7. Contrary to d_{\parallel} favoring spin spiral, strong J_1 and K make spins coupled linearly, resulting in uniform FM or G-AFM phases. Therefore, chiral spin textures are difficult to emerge in AX_2 combining small $|d_{\parallel}/J_1|$ ($\ll 0.1$) and large κ ($\gg 1$), such as CrX_2 ($X=O, S, Se, I$) and MnX_2 ($X=S, Cl$), but tend to appear in systems with large $|d_{\parallel}/J_1|$ and small κ , such as VO_2 , Al_2 ($A=Fe, Co$) and NiX_2 ($X=Cl, I$). Furthermore, we distinguish systems that hold chiral magnetism with light purple background, which are demonstrated by spin atomic model simulations. Despite only J_1 is included, the two parameters above can be considered as criteria for possible formation of spin textures since the magnitude of J_2 is very small in most cases.

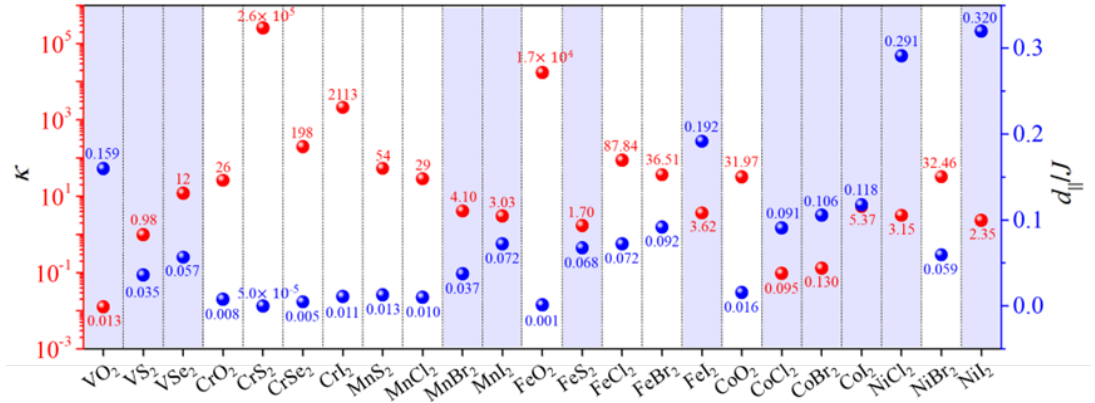


Fig. 7.7. Two criteria that could be used to predict spin textures based on magnetic interaction parameters. Red and blue dots indicate the dimensionless parameter κ and DMI/NN exchange coupling ratios $|d_{\parallel}/J_1|$ respectively. The inset numbers give specific values of κ and $|d_{\parallel}/J_1|$. Here we show these two criteria for 23 AX_2 monolayers. The column with light purple background means that the corresponding material can hold chiral spin configurations.

In summary, we propose and demonstrate the anisotropic DMI in non-polar AX_2 monolayer with $P\bar{4}m2$ crystal symmetry protection. We further unveil that various FM/AFM anti-topological quasiparticles can be stabilized without external field and provide two criteria that can predict possible spin configurations in these 2D magnets.

Moreover, the structure of AX_2 can be considered as a crucial framework to search more 2D magnets that possess anisotropic DMI and non-trivial spin configurations in other material databases. Such materials have many unique advantages, such as flexibility, gate tunability, and miniaturization, to replace the complex bulk magnets or ferromagnet/heavy metal multilayers traditionally used to achieve anti-topological magnetism and lead to development of spintronic devices with simpler structure and higher efficiency. Our work thus provides a robust route to construct crystal symmetry protected anisotropic DMI and anti-topological magnetism in 2D magnets, which will be highly promising for future spintronic applications.

Table 7.1 The optimized lattice constant (a), bonding angle of A-X-A (θ), magnetic moments of A (m), nearest-neighboring and next-nearest-neighboring exchange coupling (J_1 and J_2) and magnetic anisotropy (K). The unit of a is Å; the unit of θ is degree; the unit of m is μ_B ; the units of J_1 and J_2 are meV; and the unit of K is meV/atom. We adopt the sign convention that $J > 0$ ($J < 0$) indicates the FM (AFM) coupling, and $K > 0$ ($K < 0$) indicates OOP (IP) magnetic anisotropy.

	a	θ	m	J_1	J_2	K
VO ₂	3.111	117.108	1.155	10.072	-0.143	0.001
VS ₂	3.651	107.844	1.556	30.868	1.767	0.012
VSe ₂	3.819	105.381	1.883	39.444	-1.119	0.470
CrO ₂	3.079	117.167	2.341	72.939	8.294	0.037
CrS ₂	3.652	109.431	2.967	119.356	5.461	0.024
CrSe ₂	3.870	108.317	3.271	130.731	-1.202	-0.180
CrI ₂	4.213	100.646	4.022	55.222	-4.507	-4.379
MnS ₂	3.805	115.345	3.767	92.057	13.693	0.254
MnCl ₂	3.902	109.172	4.529	-12.351	-0.110	0.011
MnBr ₂	4.062	105.977	4.526	-10.208	-0.097	0.018
MnI ₂	4.356	104.745	4.509	-8.448	-0.068	-0.041
FeO ₂	3.158	125.455	3.079	-91.897	4.183	0.912
FeS ₂	3.300	95.458	3.415	-42.118	-4.664	-0.101
FeCl ₂	3.880	112.412	3.617	-5.909	-0.596	-0.832
FeBr ₂	4.048	109.357	3.602	-5.985	-0.223	-0.567
FeI ₂	4.324	107.790	3.562	-4.654	-1.634	-0.191
CoO ₂	2.993	116.199	2.743	-122.514	15.887	-0.302
CoCl ₂	3.707	107.961	2.600	-8.269	-0.287	0.002
CoBr ₂	3.900	106.074	2.571	-8.980	-0.240	0.004
CoI ₂	4.191	105.767	2.503	-12.226	-0.266	-0.281
NiCl ₂	3.482	100.244	1.535	-8.270	-0.171	-0.682
NiBr ₂	3.683	99.615	1.469	-12.381	-0.180	0.438
NiI ₂	3.966	100.230	1.321	-21.825	-0.705	-1.619

Chapter 8 Summary

8.1 Summary

In this thesis, by using first-principles calculations, tight-binding model and atomic spin model simulations, we propose approaches and realistic material candidates for solving crucial challenges [see detailed discussion in chapter 1 and 2] in the field of 2D magnets which impedes their applications in practical devices. We show that (i) tuning vdW interlayer distance can enhance PMA; (ii) PMA in 2D magnets further gives rise some non-trivial electronic states resulting in QAHE and AVHE; (iii) critical magnetism temperature in some 2D Janus magnets is even over room temperature; (iv) inversion symmetry breaking in 2D Janus magnets allows the existence of DMI, which results in the emergence of various chiral spin configurations; (v) ferroelectric polarization could be used to manipulate topological magnetism and (vi) 2D magnets with $P\bar{4}m2$ symmetry hold symmetry-protected anisotropic DMI, and lots of novel FM/AFM topological magnetism appear in this family due this unique type of DMI.

Next, we systematically summarize the main research results in thesis:

In chapter 3, we demonstrate that the PMA of 2D FM semiconductor, NiI₂ monolayer, can be effectively enhanced by decreasing interlayer distance of Gr/NiI₂ heterostructure. Furthermore, by analyzing atomic-resolved MAE, orbital-hybridization-resolved MAE and DOS, we clarify that the magnetic anisotropy enhancement originates from the electronic states of interfacial I atoms. At the same time, the NiI₂ substrate induces proximity effects on graphene. Specifically, the magnetic exchange field and Rashba SOC are introduced to graphene, which leads to the QAHE. These results demonstrate the enhancement of PMA via tuning interlayer distance of vdW heterostructure and provides a possible vdW system for realizing QAHE.

In chapter 4, we demonstrate that VSi₂N₄ monolayer is a 2D ferromagnetic semiconductor with valley-contrasting physics. By tuning the magnetization

orientation from IP to OOP, a relatively large valley polarization of 63.11 meV (93.51 meV based on HSE06+SOC) is generated, which results in the AVHE in VSi_2N_4 . Importantly, we obtain a formula of valley polarization and adopt a tight-binding model for VSi_2N_4 , which unveils the physical mechanism of spin-valley coupling. More interestingly, under small tensile strain, VSi_2N_4 is tuned to a “ferrovalley” material with a spontaneous valley polarization. These results highlight the VSi_2N_4 monolayer as a good candidate for both spintronic and valleytronic nanodevices.

In chapter 5, we systematically investigate the magnetic properties of 2D Janus chromium dichalcogenides CrXTe ($X=\text{S}, \text{Se}$) under strain. We find that the CrSTe monolayer has high T_c of 295K and an OOP magnetic anisotropy. In CrSeTe monolayer, the DMI is comparable to that in state-of-the-art FM/HM heterostructures, which can favor the formation of chiral Néel DW and skyrmions. As tensile strain increasing, the FM exchange coupling and PMA of Janus CrXTe monolayers both increase significantly, and the magnitude of DMI is reduced. Therefore, the ferromagnetism of Janus CrXTe monolayers is obviously enhanced, specially, distinct chiral spin textures are induced in CrSeTe monolayer. We not only give good candidates for achieving topological spin textures but also show that chiral magnetism in 2D magnets can be effectively tuned by strain.

In chapter 6, we realized the FE-controlled topological magnetic phases in Janus magnet-based multiferroic vdW HS, $\text{MBST}/\text{In}_2\text{Se}_3$. We find that when the ferroelectric polarization of In_2Se_3 reverses from up to down, the loops of vortices and antivortices are transformed into skyrmions with diameter of only 5 nm. The distinct magnetic phases are potentially used as “0” and “1” bit carriers for realizing the binary data encoding and storage. In $\text{MBST}/\text{In}_2\text{Se}_3$ HS with up polarization, the loops can be further tuned to bimeron solitons by applying IP magnetic field. Moreover, the analysis unravels that the emergence of skyrmions arises from large variation of magnetocrystalline anisotropy, which is caused by interlayer charge transfer depending on FE polarization. These reveals the potential of control of magnetic skyrmions in atom-thick vdW heterostructure by FE polarization without

assistance of external magnetic field, which will benefit for the fields of spintronics. The understood mechanism can guide searches for significant ME coupling in other Janus magnet-based multiferroic HSs, which possibly brings more nontrivial physical properties.

In chapter 6 and 7, we propose a type of artificial materials, 2D Janus magnets, for achieving topological magnetism. Notably, 2D Janus materials without magnetism, such as MoSSe and PtSSe monolayers, have been synthesized in experiments by adjusting the reaction atmosphere [256, 257]. Therefore, it is expected that the experimental realization of 2D Janus magnets in future.

In chapter 7, we propose and demonstrate that crystal symmetry protected anisotropic DMI can be realized in a family of non-polar AX_2 monolayer with $P\bar{4}m2$ space group. We show that many novel anti-topological spin textures including FM antiskyrmion and AFM antiskyrmion/antiskyrmionium/vortex-antivortex pair can be stabilized in these 2D materials without external field. Our work reveals the potential to generate anisotropic DMI and topological quasiparticles in a family of pure 2D magnets by using group symmetry protection. Moreover, AX_2 monolayer can be considered as a crucial framework to screen out more 2D magnets with anisotropic DMI and non-trivial spin textures.

8.2 Future works

One of the biggest challenges in today's world for human is realizing the tremendous information storage, processing, handling and reading with ultra-high speed and ultra-low-energy consumption. Magnetic skyrmion, a type of swirling spin textures, have many advantages including small size, high stability, high speed and low-threshold driving current, which is very hopefully used as the information carrier in next-generation spintronic devices and brings revolution to information industry. More interestingly, magnetic skyrmion in 2D magnets could inherit unique physical properties of 2D materials such as flexibility, gate turnability and intrinsic atomic thickness, which makes skyrmion is closer to practical applications. Despite some

approaches and material systems have been proposed in this thesis to solve crucial problems in this field, there are important questions needed to be answered in future.

(i) Exact dynamic properties of topological magnetism in 2D magnets. It is well known that the ISB-induced DMI could arise topological magnetism. However, the dynamic properties, such as motion speed and trajectory under spin-polarized current, of topological magnetism in 2D magnets are still unclear. If topological magnetism is considered as information carrier in future electronic devices, the current-driving behavior have to be clarified. Due to intrinsic atomic thickness and smooth edge, it is expected that the situation is quite different from bulk system. Moreover, various vdW HSs can be constructed by 2D magnets and other 2D materials such as graphene and TMDCs. large SOT could arise from the Rashba-Edelstein effects in interfaces of HSs. Therefore, SOT-driven topological magnetism also deserves to be investigated in these systems.

(ii) Specific structures of spintronic devices. After Figuring out the 2D material candidates and corresponding dynamic behavior of topological magnetism, we need design to some prototypes of spintronic devices that can make full use of advantages of topological magnetism in 2D materials and judge its performance by comparing with traditional and commercially used devices such as STT-MTJ, which thus provides direct guidance for experimental and industrial research.

Reference

- [1] M. N. Baibich, J. M. Broto, A. Fert, F. Nguyen Van Dau, F. Petroff, P. Etienne, G. Creuzet, A. Friederich, and J. Chazelas, Giant Magnetoresistance of (001)Fe/(001)Cr Magnetic Superlattices. *Phys. Rev. Lett.* 61, 2472 (1988).
- [2] G. Binasch, P. Grünberg, F. Saurenbach, and W. Zinn, Enhanced magnetoresistance in layered magnetic structures with antiferromagnetic interlayer exchange. *Phys. Rev. B* 39, 4828(R) (1989).
- [3] W. H. Butler, X.-G. Zhang, T. C. Schulthess, and J. M. MacLaren, Spin-dependent tunneling conductance of Fe|MgO|Fe sandwiches. *Phys. Rev. B* 63, 054416 (2001).
- [4] S. Yuasa, T. Nagahama, A. Fukushima et al., Giant room-temperature magnetoresistance in single-crystal Fe|MgO|Fe magnetic tunnel junctions. *Nat. Mater.* 3, 868–871 (2004).
- [5] S. Parkin, C. Kaiser, A. Panchula et al., Giant tunnelling magnetoresistance at room temperature with MgO(100) tunnel barriers. *Nat. Mater.* 3, 862–867 (2004).
- [6] X.-G. Zhang and W. H. Butler, Large magnetoresistance in bcc Co/MgO/Co and FeCo/MgO/FeCo tunnel junctions. *Phys. Rev. B* 70, 172407 (2004).
- [7] S. Ikeda, K. Miura, H. Yamamoto et al., A perpendicular-anisotropy CoFeB-MgO magnetic tunnel junction. *Nat. Mater.* 9, 721–724 (2010).
- [8] Y. M. Lee, Effect of electrode composition on the tunnel magnetoresistance of pseudo-spin-valve magnetic tunnel junction with a MgO tunnel barrier. *Appl. Phys. Lett.* 90, 212507 (2007).
- [9] X. Han, S. S. Ali, and S. Liang, MgO(001) barrier based magnetic tunnel junctions and their device applications. *Sci. China Phys. Mech. Astron.* 56, 29–60 (2013).
- [10] S. Yuasa and D. D. Djayaprawira, Giant tunnel magnetoresistance in magnetic tunnel junctions with a crystalline MgO(001) barrier. *J Phys D: Appl Phys.* 40, R337 (2007).
- [11] J. M. D. Coey, *Magnetism and Magnetic Materials.* (2010).
- [12] J. C. Slonczewski, Current-driven excitation of magnetic multilayers. *J. Magn. Magn Mater.* 159, L1 (1996).
- [13] L. Berger, Emission of spin waves by a magnetic multilayer traversed by a current. *Phys Rev B* 54, 9353 (1996).
- [14] A. Fert and F. N. Van Dau, Spintronics, from giant magnetoresistance to magnetic skyrmions and topological insulators. *C. R. Phys.* 20, 817 (2019).
- [15] A. Soumyanarayanan, N. Reyren, A. Fert, and C. Panagopoulos, Emergent phenomena induced by spin–orbit coupling at surfaces and interfaces. *Nature* 539, 509–517 (2016).
- [16] A. Manchon, H. Koo, J. Nitta, S. M. Frolov, and R. A. Duine, New perspectives for Rashba spin–orbit coupling. *Nat. Mater.* 14, 871–882 (2015).
- [17] Y. K. Kato, R. C. Myers, A. C. Gossard, and D. D. Awschalom, Observation of

- the Spin Hall Effect in Semiconductors. *Science* 306, 1910–1913 (2004).
- [18] A. Hoffmann, Spin Hall effects in metals. *IEEE Trans. Magn.* 49, 5172 (2013).
- [19] J.-C. Rojas-Sánchez et al., Spin pumping and inverse spin Hall effect in platinum: the essential role of spin-memory loss at metallic interfaces. *Phys. Rev. Lett.* 112, 106602 (2014).
- [20] C.-F. Pai, L. Liu, Y. Li, H. W. Tseng, D. C. Ralph, and R. A. Buhrman, Spin transfer torque devices utilizing the giant spin Hall effect of tungsten. *Appl. Phys. Lett.* 101, 122404 (2012).
- [21] L. Liu, C.-F. Pai, Y. Li, H.W. Tseng, D. C. Ralph, and R. A. Buhrman, Spin-torque switching with the giant spin Hall effect of tantalum. *Science* 336, 555–558 (2012).
- [22] C. Hahn, G. de Loubens, O. Klein, M. Viret, V. V. Naletov, and J. Ben Youssef, Comparative measurements of inverse spin Hall effects and magnetoresistance in YIG/Pt and YIG/Ta. *Phys. Rev. B* 87, 174417 (2013).
- [23] J. Sinova, S. O. Valenzuela, J. Wunderlich, C. H. Back, and T. Jungwirth, Spin Hall effects. *Rev. Mod. Phys.* 87, 1213 (2015).
- [24] C. L. Kane and E. J. Mele, Quantum Spin Hall Effect in Graphene. *Phys. Rev. Lett.* 95, 226801 (2005).
- [25] B. A. Bernevig, T. L. Hughes, and S.-C. Zhang, Quantum Spin Hall Effect and Topological Phase Transition in HgTe Quantum Wells. *Science* 314, 1757-1761 (2006).
- [26] M. König, S. Wiedmann, C. Brüne, A. Roth, H. Buhmann, L. W. Molenkamp, X.-L. Qi and S.-C. Zhang, Quantum Spin Hall Insulator State in HgTe Quantum Wells. *Science* 318, 766-770 (2007).
- [27] X.-L. Qi and S.-C. Zhang, Topological insulators and superconductors. *Rev. Mod. Phys.* 83, 1057 (2011).
- [28] H. Zhang, C.-X. Liu, X.-L. Qi et al., Topological insulators in Bi₂Se₃, Bi₂Te₃ and Sb₂Te₃ with a single Dirac cone on the surface. *Nat. phys.* 5, 438-442 (2009).
- [29] R. Yu, W. Zhang, H.-J. Zhang, S.-C. Zhang, X. Dai, and Z. Fang, Quantized anomalous Hall effect in magnetic topological insulators. *Science* 329, 61-64 (2010).
- [30] C.-Z. Chang, J. Zhang, X. Feng et al., Experimental observation of the quantum anomalous Hall effect in a magnetic topological insulator. *Science* 340, 167-170 (2013).
- [31] Z. Yue, B. Cai, L. Wang, X. Wang, and M. Gu, Intrinsically core-shell plasmonic dielectric nanostructures with ultrahigh refractive index. *Sci. Adv.* 2, e1501536 (2016).
- [32] Z. Yue, G. Xue, J. Liu, Y. Wang, and M. Gu, Nanometric holograms based on a topological insulator material. *Nat. Commun.* 8, 15354 (2017).
- [33] Y. Tokura, K. Yasuda, and A. Tsukazaki, Magnetic topological insulators. *Nat. Rev. Phys.* 1, 126–143 (2019).
- [34] A. Fert, V. Cros, and J. Sampaio, Skyrmions on the track. *Nat. Nanotechnol.* 8, 152–156 (2013).
- [35] S. S. P. Parkin and S.-H. Yang, Memory on the racetrack. *Nat. Nanotechnol.* 10,

- 195–198 (2015).
- [36] S. Luo, M. Song, X. Li, Y. Zhang, J. Hong, X. Yang, X. Zou, N. Xu, and L. You, Reconfigurable Skyrmion Logic Gates. *Nano Lett.* 18, 1180–1184 (2018).
- [37] K. M. Song, J. S. Jeong, B. Pan, X. Zhang, J. Xia, S. Cha, T. E. Park, K. Kim, S. Finizio, J. Raabe, J. Chang, Y. Zhou, W. Zhao, W. Kang, H. Ju, and S. Woo, Skyrmion-based artificial synapses for neuromorphic computing. *Nat. Electron.* 3, 148–155 (2020).
- [38] C. Psaroudaki and C. Panagopoulos, Skyrmion Qubits: A New Class of Quantum Logic Elements Based on Nanoscale Magnetization. *Phys. Rev. Lett.* 127, 067201 (2021).
- [39] A. Fert, A. Reyren and V. Cros, Magnetic skyrmions: advances in physics and potential applications. *Nat. Rev. Mater.* 2, 1-15 (2017).
- [40] T. Smith, The magnetic properties of hematite. *Phys. Rev.* 8, 721 (1916).
- [41] A. S. Borovik-Romanov and M. P. Orlova, Magnetic Properties of Cobalt and Manganese Carbonates. *Sov. Phys. JETP* 4, 531 (1956).
- [42] I. E. Dzyaloshinskii, Thermodynamic Theory of “Weak” Ferromagnetism in Antiferromagnetic Substances. *Sov. Phys. JETP* 5, 1259 (1957).
- [43] I. E. Dzyaloshinskii, A thermodynamic theory of “weak” ferromagnetism of antiferromagnetics. *J. Phys. Chem. Solids* 4, 241 (1958).
- [44] T. Moriya, New Mechanism of Anisotropic Superexchange Interaction. *Phys. Rev. Lett.* 4, 228 (1960).
- [45] T. Moriya, Anisotropic Superexchange Interaction and Weak Ferromagnetism. *Phys. Rev.* 120, 91 (1960).
- [46] A. Fert and P. M. Levy, Role of anisotropic exchange interactions in determining the properties of spin-glasses. *Phys. Rev. Lett.* 44, 1538 (1980).
- [47] H. Yang, A. Thiaville, S. Rohart, A. Fert, and M. Chshiev, Anatomy of Dzyaloshinskii-Moriya interaction at Co/Pt interfaces. *Phys. Rev. Lett.* 115, 267210 (2015).
- [48] H. Yang, G. Chen, A. A. C. Cotta et al., Significant Dzyaloshinskii–Moriya interaction at graphene–ferromagnet interfaces due to the Rashba effect. *Nat. Mater.* 17, 605–609 (2018).
- [49] K. S. Novoselov, A. K. Geim, S. V. Morozov, D. Jiang, Y. Zhang, S. V. Dubonos, I. V. Grigorieva, and A. A. Firsov, Electric Field Effect in Atomically Thin Carbon Films. *Science* 306, 666-669 (2004).
- [50] F. Schedin, A. K. Geim, S. V. Morozov, E. W. Hill, P. Blake, M. I. Katsnelson, and K. S. Novoselov, Detection of individual gas molecules adsorbed on graphene. *Nat. Mater.* 6, 652-655 (2007).
- [51] A. A. Balandin, S. Ghosh, W. Bao, I. Calizo, D. Teweldebrhan, F. Miao, and C. N. Lau, Superior Thermal Conductivity of Single-Layer Graphene. *Nano Lett.* 8, 902-907 (2008).
- [52] R. R. Nair, P. Blake, A. N. Grigorenko, K. S. Novoselov, T. J. Booth, T. Stauber, N. M. R. Peres, and A. K. Geim, Fine Structure Constant Defines Visual Transparency of Graphene. *Science* 320, 1308-1308 (2008).
- [53] J. Meyer, A. Geim, M. Katsnelson et al., The structure of suspended graphene

- sheets. *Nature* 446, 60-63 (2007).
- [54] L. Peng, Z. Xu, Z. Liu, Y. Guo, P. Li, and C. Gao, Ultrahigh Thermal Conductive yet Superflexible Graphene Films. *Adv. Mater.* 29, 1700589 (2017).
- [55] K. S. Novoselov, A. K. Geim, S. V. Morozov, D. Jiang, M. I. Katsnelson, I. V. Grigorieva, S. V. Dubonos, and A. A. Firsov, Two-dimensional gas of massless Dirac fermions in graphene. *Nature* 438, 197-200 (2005).
- [56] A. H. Castro Neto, F. Guinea, N. M. R. Peres, K. S. Novoselov, and A. K. Geim, The electronic properties of graphene. *Rev. Mod. Phys.* 81, 109 (2009).
- [57] Y. Zhang, Y.-W. Tan, H. L. Stormer, and P. Kim, Experimental observation of the quantum Hall effect and Berry's phase in graphene. *Nature* 438, 201-204 (2005).
- [58] Z. Qiao, S. A. Yang, W. Feng et al., Quantum anomalous Hall effect in graphene from Rashba and exchange effects. *Phys. Rev. B* 82, 161414(R) (2010).
- [59] K. F. Mak, C. Lee, J. Hone, J. Shan, and T. F. Heinz, Atomically Thin MoS₂: A New Direct-Gap Semiconductor. *Phys. Rev. Lett.* 105, 136805 (2010).
- [60] A. Kuc, N. Zibouche, and T. Heine, Influence of quantum confinement on the electronic structure of the transition metal sulfide *TS*₂. *Phys. Rev. B* 83, 245213 (2011).
- [61] W. S. Yun, S. W. Han, S. C. Hong, I. G. Kim, and J. D. Lee, Thickness and strain effects on electronic structures of transition metal dichalcogenides: 2H-*MX*₂ semiconductors (*M*=Mo, W; *X*=S, Se, Te). *Phys. Rev. B* 85, 033305 (2012).
- [62] M. Chhowalla, H. Shin, G. Eda et al., The chemistry of two-dimensional layered transition metal dichalcogenide nanosheets. *Nat. Chem.* 5, 263–275 (2013).
- [63] X. Duan, C. Wang, A. Pan, R. Yu, and X. Duan, Two-dimensional transition metal dichalcogenides as atomically thin semiconductors: opportunities and challenges. *Chem. Soc. Rev.* 44, 8859–8876 (2015).
- [64] Y. Liu, X. Duan, H. J. Shin, S. Park, Y. Huang, and X. Duan, Promises and prospects of two-dimensional transistors. *Nature* 591, 43-53 (2021).
- [65] D. Xiao, W. Yao, and Q. Niu, Valley-contrasting physics in graphene: magnetic moment and topological transport. *Phys. Rev. Lett.* 99, 236809 (2007).
- [66] W. Yao, D. Xiao, and Q. Niu, Valley-dependent optoelectronics from inversion symmetry breaking. *Phys. Rev. B* 77, 235406 (2008).
- [67] D. Xiao, G. Liu, W. Feng, X. Xu, and W. Yao, Coupled Spin and Valley Physics in Monolayers of MoS₂ and other group-VI dichalcogenides. *Phys. Rev. Lett.* 108, 196802 (2012).
- [68] T. Cao, G. Wang, W. Han, H. Ye, C. Zhu, J. Shi, Q. Niu, P. Tan, E. Wang, B. Liu, and J. Feng, Valley-selective circular dichroism of monolayer molybdenum disulphide. *Nat. Commun.* 3, 887 (2012).
- [69] X. Li, T. Cao, Q. Niu, J. Shi and J. Feng, Coupling the valley degree of freedom to antiferromagnetic order. *Proc. Natl. Acad. Sci. U. S. A.* 110, 3738 (2013).
- [70] J. R. Schaibley, H. Yu, G. Clark, P. Rivera, J. S. Ross, K. L. Seyler, W. Yao and X. Xu, Valleytronics in 2D materials. *Nat. Rev. Mater.* 1, 1 (2016).
- [71] K. F. Mak, K. L. McGill, J. Park, and P. L. McEuen, The valley Hall effect in MoS₂ transistors, *Science* 344, 1489 (2014).
- [72] J. Lee, K. F. Mak, and J. Shan, Electrical control of the valley Hall effect in

- bilayer MoS₂ transistors. *Nat. Nanotechnol.* 11, 421 (2016).
- [73] H. Zeng, J. Dai, W. Yao, D. Xiao, and X. Cui, Valley polarization in MoS₂ monolayers by optical pumping. *Nat. Nanotechnol.* 7, 490 (2012).
- [74] N. D. Mermin and H. Wagner, Absence of ferromagnetism or antiferromagnetism in one-or two-dimensional isotropic Heisenberg models. *Phys. Rev. Lett.* 17, 1133 (1966).
- [75] B. Huang, G. Clark, E. Navarro-Moratalla, D. R. Klein, R. Cheng, K. L. Seyler, D. Zhong, E. Schmidgall, M. A. McGuire, D. H. Cobden, W. Yao, D. Xiao, P. Jarillo-Herrero, and X. Xu, Layer-dependent ferromagnetism in a van der Waals crystal down to the monolayer limit. *Nature* 546, 270 (2017).
- [76] C. Gong, L. Li, Z. Li, H. Ji, A. Stern, Y. Xia, T. Cao, W. Bao, C. Wang, Y. Wang, Z. Q. Qiu, R. J. Cava, S. G. Louie, J. Xia, and X. Zhang, Discovery of intrinsic ferromagnetism in two-dimensional van der Waals crystals. *Nature* 546, 265 (2017).
- [77] D. J. O'Hara, T. Zhu, A. H. Trout, A. S. Ahmed, Y. K. Luo, C. H. Lee, M. R. Brenner, S. Rajan, J. A. Gupta, D. W. McComb, and R. K. Kawakami, Room temperature intrinsic ferromagnetism in epitaxial manganese selenide films in the monolayer limit. *Nano Lett.* 18, 3125 (2018).
- [78] M. Bonilla, S. Kolekar, Y. Ma, H. C. Diaz, V. Kalappattil, R. Das, T. Eggers, H. R. Gutierrez, M.-H. Phan, and M. Batzill, Strong room-temperature ferromagnetism in VSe₂ monolayers on van der Waals substrates. *Nat. Nanotechnol.* 13, 289 (2018).
- [79] Z. Fei, B. Huang, P. Malinowski, et al. Two-dimensional itinerant ferromagnetism in atomically thin Fe₃GeTe₂. *Nat. Mater.* 17 (9), 778-782 (2018).
- [80] Y. Deng, Y. Yu, Y. Song, J. Zhang, N. Z. Wang, Z. Sun, Y. Yi, Y. Z. Wu, S. Wu, J. Zhu, J. Wang, X. H. Chen, and Y. Zhang, Gate-tunable room-temperature ferromagnetism in two-dimensional Fe₃GeTe₂. *Nature* 563, 94 (2018).
- [81] A. Bedoya-Pinto, J. R. Ji, A. K. Pandeya, et al. Intrinsic 2D-XY ferromagnetism in a van der Waals monolayer. *Science* 374 (6567), 616-620 (2021).
- [82] T. Song, X. Cai, M. W. Y. Tu, et al. Giant tunneling magnetoresistance in spin-filter van der Waals heterostructures. *Science* 360, 1214-1218 (2018).
- [83] C. Cardoso, D. Soriano, N. A. García-Martínez, et al. Van der Waals spin valves. *Phys. Rev. Lett.* 121, 067701 (2018).
- [84] X. Wang, J. Tang, X. Xia, C. He, J. Zhang, Y. Liu, C. Wan, C. Fang, C. Guo, W. Yang, Y. Guang, X. Zhang, H. Xu, J. Wei, M. Liao, X. Lu, J. Feng, X. Li, Y. Peng, H. Wei1, R. Yang, D. Shi, X. Zhang, Z. Han, Z. Zhang, G. Zhang, G. Yu, and X. Han, Current-driven magnetization switching in a van der Waals ferromagnet Fe₃GeTe₂. *Sci. Adv.* 5, eaaw8904 (2019).
- [85] H. Sato, M. Yamanouchi, K. Miura, S. Ikeda, R. Koizumi, F. Matsukura, H. Ohno, CoFeB Thickness Dependence of Thermal Stability Factor in CoFeB/MgO Perpendicular Magnetic Tunnel Junctions. *IEEE Magn. Lett.* 3, 3000204 (2012).
- [86] C. Gong and X. Zhang, Two-dimensional magnetic crystals and emergent heterostructure devices. *Science* 363, eaav4450 (2019).
- [87] B. Yang, X. Zhang, H. Yang, X. Han and Y. Yan, Strain controlling transport

- properties of heterostructure composed of monolayer CrI₃. *Appl. Phys. Lett.* 114, 192405 (2019).
- [88] C. Tang, L. Zhang and A. Du, Tunable magnetic anisotropy in 2D magnets via molecular adsorption. *J. Mater. Chem. C* 8, 14948 (2020).
- [89] F. Xue, Y. Hou, Z. Wang and R. Wu, Two-dimensional ferromagnetic van der Waals CrCl₃ monolayer with enhanced anisotropy and Curie temperature. *Phys. Rev. B* 100, 224429 (2019).
- [90] E. Ising, Beitrag zur Theorie des Ferromagnetismus. *Z. Phys.* 31, 253–258 (1925).
- [91] L. Onsager, Crystal Statistics. I. A Two-Dimensional Model with an Order-Disorder Transition. *Phys. Rev.* 65, 117–149 (1944).
- [92] P. C. Hohenberg, Existence of Long-Range Order in 1 and 2 Dimensions. *Phys. Rev.* 158, 383–386 (1967).
- [93] Q. Wang, A. B.-Pinto, M. Blei et al., The Magnetic Genome of Two-Dimensional van der Waals Materials. *ACS Nano* 16, 6960–7079 (2022).
- [94] N. Nagaosa, J. Sinova, S. Onoda, A. H. MacDonald, and N. P. Ong, Anomalous Hall effect. *Rev. Mod. Phys.* 82, 1539 (2010).
- [95] D. MacNeill, C. Heikes, K. F. Mak, Z. Anderson, A. Kormanyos, V. Zolyomi, J. Park, and D. C. Ralph, Breaking of valley degeneracy by magnetic field in monolayer MoSe₂. *Phys. Rev. Lett.* 114, 037401 (2015).
- [96] P. Back, M. Sidler, O. Cotlet, A. Srivastava, N. Takemura, M. Kroner, and A. Imamoğlu, Giant paramagnetism-induced valley polarization of electrons in charge-tunable monolayer MoSe₂. *Phys. Rev. Lett.* 118, 237404 (2017).
- [97] R. Peng, Y. Ma, S. Zhang, B. Huang, and Y. Dai, Valley polarization in Janus single-layer MoSSe via magnetic doping. *J. Phys. Chem. Lett.* 9, 3612 (2018).
- [98] J. Li, L. Gu, and R. Wu, Possible realization and protection of valley-polarized quantum Hall effect in Mn/WS₂. *Phys. Rev. B* 101, 024412 (2020).
- [99] C. Zhao, T. Norden, P. Zhang, P. Zhao, Y. Cheng, F. Sun, J. P. Parry, P. Taheri, J. Wang, Y. Yang, T. Scrace, K. Kang, S. Yang, G. Miao, R. Sabirianov, G. Kioseoglou, W. Huang, A. Petrou, and H. Zeng, Enhanced valley splitting in monolayer WSe₂ due to magnetic exchange field. *Nat. Nanotechnol.* 17, 757 (2017).
- [100] T. Norden, C. Zhao, P. Zhang, R. Sabirianov, A. Petrou, and H. Zeng, Giant valley splitting in monolayer WS₂ by magnetic proximity effect. *Nat. Commun.* 10, 4163 (2019).
- [101] P. Jiang, L. Li, Z. Liao, Y. Zhao, Z. Zhong, Spin Direction-Controlled Electronic Band Structure in Two-Dimensional Ferromagnetic CrI₃. *Nano letters* 18, 3844 (2018).
- [102] A. Junkaew, C. Rungnim, M. Kunaseth, R. Arróyave, V. Promarak, N. Kungwand, and S. Namuangruk, Metal cluster-deposited graphene as an adsorptive material for m-xylene. *New J. Chem.* 39, 9650 (2015).
- [103] W. Tong, S. Gong, X. Wan, and C. Duan, Concepts of ferrovalley material and anomalous valley Hall effect. *Nat. Commun.* 7, 13612 (2016).
- [104] S. Mühlbauer, B. Binz, F. Jonietz, C. Pfleiderer, A. Rosch, A. Neubauer, R.

- Georgii, P. Böni, Skyrmion Lattice in a Chiral Magnet. 330, 1648 (2010).
- [105] W. Münzer, A. Neubauer, T. Adams, S. Mühlbauer, C. Franz, F. Jonietz, R. Georgii, P. Böni, B. Pedersen, M. Schmidt, A. Rosch, and C. Pfleiderer, Skyrmion lattice in the doped semiconductor $\text{Fe}_{1-x}\text{Co}_x\text{Si}$. *Phys. Rev. B* 81, 041203 (2010).
- [106] X. Z. Yu, N. Kanazawa, Y. Onose, K. Kimoto, W. Z. Zhang, S. Ishiwata, Y. Matsui, and Y. Tokura, Near room-temperature formation of a skyrmion crystal in thin-films of the helimagnet FeGe. *Nat. Mater.* 10, 106 (2011).
- [107] A. Soumyanarayanan, M. Raju, A. G. Oyarce, A. K. Tan, M. Y. Im, A. P. Petrović, P. Ho, K. H. Khoo, M. Tran, C. K. Gan, F. Ernult, and C. Panagopoulos, Tunable room-temperature magnetic skyrmions in Ir/Fe/Co/Pt multilayers. *Nat. Mater.* 16, 898-904 (2017).
- [108] H. Yang, O. Boulle, V. Cros, A. Fert, and M. Chshiev, Controlling Dzyaloshinskii-Moriya interaction via chirality dependent atomic-layer stacking, insulator capping and electric field. *Sci. Rep.* 8, 1-7 (2018).
- [109] M. Raju, A. Yagil, A. Soumyanarayanan, A. K. Tan, A. Almoalem, F. Ma, O. M. Auslaender, and C. Panagopoulos, The evolution of skyrmions in Ir/Fe/Co/Pt multilayers and their topological Hall signature. *Nat. Commun.* 10, 1-7 (2019)
- [110] B. Cui, D. Yu, Z. Shao et al., Néel-Type elliptical skyrmions in a laterally asymmetric magnetic multilayer. *Adv. Mater.* 2006924 (2021).
- [111] K. Chen, and F. Shu, Spin Pumping in the Presence of Spin-Orbit Coupling. *Phys. Rev. Lett.* 114, 126602 (2015).
- [112] N.-H. Kim, J. Jung, and J. Cho, Interfacial Dzyaloshinskii-Moriya interaction, surface anisotropy energy, and spin pumping at spin orbit coupled Ir/Co interface. *Appl. Phys. Lett.* 108, 142406 (2016).
- [113] M. Born, and R. Oppenheimer, Zur quantentheorie der molekeln. *Ann. Phys.* 389, 457-484 (1927).
- [114] M. Born, K. Huang, and M. Lax, Dynamical theory of crystal lattices. *Am. J. Phys.* 23, 474 (1955).
- [115] P. Hohenberg, and W. Kohn, Inhomogeneous electron gas. *Phys. Rev.* 136, 864 (1964).
- [116] W. Kohn, and L. J. Sham, Self-consistent equations including exchange and correlation effects. *Phys. Rev.* 140, 1133 (1965).
- [117] M. Slamet and V. Sahni, The gradient expansion approximation for exchange: A physical prespective. *Int. J. Quantum Chem.* 44, 333-345 (1992).
- [118] J. P. Perdew, K. Burke, and M. Ernzerhof, Generalized gradient approximation made simple. *Phys. Rev. Lett.* 77(18), 3865 (1996).
- [119] J. C. Slater, and G. F. Koster, Simplified LCAO method for the Periodic Potential Problem. *Phys. Rev.* 94, 1498 (1954).
- [120] J. Singleton, *Band Theory and Electronic Properties of Solids*. Oxford (2001).
- [121] A. Vansteenkiste, J. Leliaert, M. Dvornik et al., The design and verification of MuMax3. *AIP Adv.* 4, 107133 (2014).
- [122] K. S. Burch, D. Mandrus, and J. G. Park, Magnetism in two-dimensional van

- der Waals materials. *Nature* 563, 47 (2018).
- [123] X. Li and J. Yang, Realizing Two-Dimensional Magnetic Semiconductors with Enhanced Curie Temperature by Antiaromatic Ring Based Organometallic Frameworks. *J. Am. Chem. Soc.* 141, 109 (2019).
- [124] C. Huang, J. Feng, F. Wu, D. Ahmed, B. Huang, H. Xiang, and E. Kan, Toward Intrinsic Room-Temperature Ferromagnetism in Two-Dimensional Semiconductors. *J. Am. Chem. Soc.* 140, 11519 (2018).
- [125] M. Gibertini, M. Koperski, A. F. Morpurgo, and K. S. Novoselov, Magnetic 2D materials and heterostructures. *Nat. Nanotechnol.* 14, 408 (2019).
- [126] X. Zhao, T. Wang, C. Xia, X. Dai, S. Wei, and L. Yang, Magnetic doping in two-dimensional transition-metal dichalcogenide zirconium diselenide. *J. Alloys Compd.* 698, 611 (2017).
- [127] V. Kochat, A. Apte, J. A. Hachtel et al., Re Doping in 2D Transition Metal Dichalcogenides as a New Route to Tailor Structural Phases and Induced Magnetism. *Adv. Mater.* 29, 1703754 (2017).
- [128] H. González-Herrero, J. M. Gómez-Rodríguez, P. Mallet, M. Moaied, J. J. Palacios, C. Salgado and I. Brihuega, Atomic-scale control of graphene magnetism by using hydrogen atoms. *Science* 352, 437 (2016).
- [129] J. Ding, Z. H. Qiao, W. X. Feng, Y. G. Yao, and Q. Niu, Quantum anomalous Hall effect in graphene from Rashba and exchange effects. *Phys. Rev. B* 84, 195444 (2011).
- [130] H. X. Yang, M. Chshiev, D. W. Boukhvalov, X. Waintal, and S. Roche, Inducing and optimizing magnetism in graphene nanomeshes. *Phys. Rev. B* 84, 214404 (2011).
- [131] L. Kou, C. Tang, Y. Zhang, T. Heine, C. Chen, and T. Frauenheim, Tuning Magnetism and Electronic Phase Transitions by Strain and Electric Field in Zigzag MoS₂ Nanoribbons. *J. Phys. Chem. Lett.* 3, 2934 (2012).
- [132] W. Han, R. K. Kawakami, M. Gmitra, and J. Fabian, Graphene spintronics. *Nat. Nanotechnol.* 9, 794 (2014).
- [133] S. Wang, L. Talirz, C. A. Pignedoli, X. Feng, K. Müllen, R. Fasel, and P. Ruffieux, Giant edge state splitting at atomically precise graphene zigzag edges. *Nat. Commun.* 7, 11507 (2016).
- [134] Z. Zhang, J. Shang, C. Jiang, A. Rasmita, W. Gao and T. Yu, Direct Photoluminescence Probing of Ferromagnetism in Monolayer Two-Dimensional CrBr₃. *Nano Lett.* 19, 3138 (2019).
- [135] J. L. Lado, and J. Fernández-Rossier, On the origin of magnetic anisotropy in two dimensional CrI₃. *2D Mater.* 4, 035002 (2017).
- [136] L. Webster, and J. A. Yan, Strain-tunable magnetic anisotropy in monolayer CrCl₃, CrBr₃, and CrI₃. *Phys. Rev. B* 98, 144411 (2018).
- [137] B. Dieny, and M. Chshiev, Perpendicular magnetic anisotropy at transition metal/oxide interfaces and applications. *Rev. Mod. Phys.* 89, 025008 (2017).
- [138] L. Berger, Emission of spin waves by a magnetic multilayer traversed by a current. *Phys. Rev. B* 54, 9353 (1996).
- [139] A. D. Kent, Perpendicular all the way. *Nat. Mater.* 9, 699-700 (2010).

- [140] H. Yang, A. D. Vu, A. Hallal, N. Rougemaille, J. Coraux, G. Chen, A. K. Schmid and M. Chshiev, Anatomy and Giant Enhancement of the Perpendicular Magnetic Anisotropy of Cobalt–Graphene Heterostructures. *Nano. Lett.* 16, 145 (2016).
- [141] C. Gong, E. M. Kim, Y. Wang, G. Lee, and X. Zhang, Multiferroicity in atomic van der Waals heterostructures. *Nat. Commun.* 10, 2657 (2019).
- [142] P. Ci, Y. Chen, J. Kang, R. Suzuki, H. S. Choe, J. Suh, and S. Tongay, Quantifying van der Waals Interactions in Layered Transition Metal Dichalcogenides from Pressure-Enhanced Valence Band Splitting. *Nano Lett.* 17, 4982 (2017).
- [143] T. Song, Z. Fei, M. Yankowitz et al., Switching 2D magnetic states via pressure tuning of layer stacking. *Nat. Mater.* 18, 1298-1302 (2019).
- [144] T. Li, S. Jiang, N. Sivadas et al., Pressure-controlled interlayer magnetism in atomically thin CrI₃. *Nat. Mater.* 18, 1303-1308 (2019).
- [145] M. Yankowitz, S. Chen, H. Polshyn, Y. Zhang, K. Watanabe, T. Taniguchi, and C. R. Dean, Tuning superconductivity in twisted bilayer graphene. *Science* 363, 1059 (2019).
- [146] W. Yao, E. Wang, C. Bao, Y. Zhang, K. Zhang, K. Bao, C. K. Chan, C. Chen, J. Avila, M. C. Asensio, J. Zhu and S. Zhou, Quasicrystalline 30° twisted bilayer graphene as an incommensurate superlattice with strong interlayer coupling. *PNAS* 115, 6928 (2018).
- [147] W. Chen, Z. Sun, Z. Wang, L. Gu, X. Xu, S. Wu, and C. Gao, Direct observation of van der Waals stacking–dependent interlayer magnetism. *Science* 366, 983 (2019).
- [148] K. Lai, H. Li, Y. Xu, W. Zhang and J. Dai, Achieving a direct band gap and high power conversion efficiency in an SbI₃/BiI₃ type-II vdW heterostructure via interlayer compression and electric field application. *Phys. Chem. Chem. Phys.* 21, 2619 (2019).
- [149] H. X. Yang, A. Hallal, D. Terrade, X. Waintal, S. Roche, and M. Chshiev, Proximity Effects Induced in Graphene by Magnetic Insulators: First-Principles Calculations on Spin Filtering and Exchange-Splitting Gaps. *Phys. Rev. Lett.* 110, 046603 (2013).
- [150] A. G. Swartz, P. M. Odenthal, Y. Hao, R. S. Ruoff, and R. K. Kawakami, Integration of the Ferromagnetic Insulator EuO onto Graphene. *ACS Nano* 6, 10063 (2012).
- [151] Z. Wang, C. Tang, R. Sachs, Y. Barlas and J. Shi, Proximity-Induced Ferromagnetism in Graphene Revealed by the Anomalous Hall Effect. *Phys. Rev. Lett.* 114, 016603 (2015).
- [152] P. Wei, S. Lee, F. Lemaitre, L. Pinel, D. Cutaia, W. Cha, F. Katmis, Y. Zhu, D. Heiman, J. Hone, J. S. Moodera and C. T. Chen, Strong interfacial exchange field in the graphene/EuS heterostructure. *Nat. Mater.* 15, 711-716 (2016).
- [153] A. Hallal, F. Ibrahim, H. Yang, S. Roche, and M. Chshiev, Tailoring magnetic insulator proximity effects in graphene: first-principles calculations. *2D Mater.* 4, 025074 (2017).

- [154] J. Zhang, B. Zhao, Y. Yao, and Z. Yang, Robust quantum anomalous Hall effect in graphene-based van der Waals heterostructures. *Phys. Rev. B* 92, 165418 (2015)
- [155] J. Zhang, B. Zhao, T. Zhou, Y. Xue, C. Ma, and Z. Yang, Strong magnetization and Chern insulators in compressed graphene/CrI₃ van der Waals heterostructures. *Phys. Rev. B* 97, 085401 (2018).
- [156] H. Zhang, Y. Ning, W. Yang, J. Zhang, R. Zhang, and X. Xu, Possible realization of the high-temperature and multichannel quantum anomalous Hall effect in graphene/CrBr₃ heterostructures under pressure. *Phys. Chem. Chem. Phys.* 21, 17087 (2019).
- [157] M. P. Pasternak, R. D. Taylor, A. Chen, C. Meade, L. M. Falicov, A. Gieseckus, J. Raymond, and Y. Y. Peter, Pressure-induced metallization and the collapse of the magnetic state in the antiferromagnetic insulator NiI₂. *Phys. Rev. Lett.* 65, 790 (1990).
- [158] V. V. Kulish, and W. Huang, Single-layer metal halides MX₂ (X = Cl, Br, I): stability and tunable magnetism from first principles and Monte Carlo simulations. *J. Mater. Chem. C* 5, 8734 (2017).
- [159] A. S. Botana, and M. R. Norman, Electronic structure and magnetism of transition metal dihalides: Bulk to monolayer. *Phys. Rev. Mater.* 3, 044001 (2019).
- [160] M. Lu, Q. Yao, C. Xiao, C. Huang, and E. Kan, Mechanical, Electronic, and Magnetic Properties of NiX₂ (X = Cl, Br, I) Layers. *ACS Omega* 4, 5714 (2019).
- [161] G. Kresse, J. Furthmüller, Efficient iterative schemes for ab initio total-energy calculations using a plane-wave basis set. *Phys. Rev. B* 54, 11169 (1996).
- [162] G. Kresse, J. Furthmüller, Efficiency of ab-initio total energy calculations for metals and semiconductors using a plane-wave basis set. *Comput. Mater. Sci.* 6, 15 (1996).
- [163] G. Kresse and J. Hafner, Ab initio molecular dynamics for liquid metals. *Phys. Rev. B* 47, 558 (1993).
- [164] A. I. Liechtenstein, V. I. Anisimov, and J. Zaanen, Density-functional theory and strong interactions: Orbital ordering in Mott-Hubbard insulators. *Phys. Rev. B* 52, R5467(R) (1995).
- [165] S. Grimme, J. Antony, S. Ehrlich, and S. Krieg, A consistent and accurate ab initio parametrization of density functional dispersion correction (DFT-D) for the 94 elements H-Pu. *J. Chem. Phys.* 132, 154104 (2010).
- [166] R. F. W. Bader, *Atoms in Molecules - A Quantum Theory*, Oxford University Press, Oxford, 1990.
- [167] W. Tang, E. Sanville, and G. Henkelman, A grid-based Bader analysis algorithm without lattice bias. *J. Phys.: Condens. Matter* 21, 084204 (2009).
- [168] E. Sanville, S. D. Kenny, R. Smith, and G. Henkelman, Improved grid-based algorithm for Bader charge allocation. *J. Comp. Chem.* 28, 899-908 (2007).
- [169] G. Henkelman, A. Arnaldsson, and H. Jónsson, A fast and robust algorithm for Bader decomposition of charge density. *Comput. Mater. Sci.* 36, 354-360 (2006).

- [170] M. Yu and D. R. Trinkle, Accurate and efficient algorithm for Bader charge integration. *J. Chem. Phys.* 134, 064111 (2011).
- [171] M. G. Brik, N. M. Avram, and C. N. Avram, Comparative crystal field study of Ni²⁺ energy levels in NiCl₂, NiBr₂, and NiI₂ crystals. *Physica B* 371, 43 (2006).
- [172] D. -S. Wang, R. Wu and A. J. Freeman, First-principles theory of surface magnetocrystalline anisotropy and the diatomic-pair model. *Phys. Rev. B* 47, 14932 (1993).
- [173] B. S. Yang, J. Zhang, L. N. Jiang, W. Z. Chen, P. Tang, X.-G. Zhang, Y. Yan and X. F. Han, Strain induced enhancement of perpendicular magnetic anisotropy in Co/graphene and Co/BN heterostructures. *Phys. Rev. B* 95, 174424 (2017).
- [174] Z. Qiao, W. Ren, H. Chen, L. Bellaiche, Z. Zhang, A. H. MacDonald, and Q. Niu, Quantum anomalous Hall effect in graphene proximity coupled to an antiferromagnetic insulator. *Phys. Rev. Lett.* 112, 116404 (2014).
- [175] Y. G. Yao, L. Kleinman, A. H. MacDonald, J. Sinova, T. Jungwirth, D.-S. Wang, E. Wang, and Q. Niu, First principles calculation of anomalous Hall conductivity in ferromagnetic bcc Fe. *Phys. Rev. Lett.* 92, 037204 (2004).
- [176] S. Liu, A. G. d. Águila, X. Liu, Y. Zhu, Y. Han, A. Chaturvedi, P. Gong, H. Yu, H. Zhang, W. Yao, and Q. Xiong, Room-temperature valley polarization in atomically thin semiconductors via chalcogenide alloying. *ACS nano* 14, 9873 (2020).
- [177] G. Aivazian, Z. Gong, A. M. Jones, R. Chu, J. Yan, D. G. Mandrus, C. Zhang, D. Cobden, W. Yao, and X. Xu, Magnetic control of valley pseudospin in monolayer WSe₂. *Nat. Phys.* 11, 148 (2015).
- [178] A. Srivastava, M. Sidler, A. V. Allain, D. S. Lembke, A. Kis, and A. Imamoglu, Valley Zeeman effect in elementary optical excitations of monolayer WSe₂. *Nat. Phys.* 11, 141 (2015).
- [179] Z. Ye, D. Sun, and T. F. Heinz, Optical manipulation of valley pseudospin. *Nat. Phys.* 13, 26 (2017).
- [180] Y. Hong, Z. Liu, L. Wang, T. Zhou, W. Ma, C. Xu, S. Feng, L. Chen, M. Chen, D. Sun, X. Chen, H. Cheng, W. Ren, Chemical vapor deposition of layered two-dimensional MoSi₂N₄ materials. *Science* 369, 670 (2020).
- [181] H. L. Zhuang, and R. G. Hennig, Stability and magnetism of strongly correlated single-layer VS₂. *Phys. Rev. B* 93, 054429 (2016).
- [182] A. V. Krugau, O. A. Vydrov, A. F. Izmaylov, and G. E. Scuseria, Influence of the exchange screening parameter on the performance of screened hybrid functionals. *J. Chem. Phys.* 125, 224106 (2006).
- [183] A. Togo, and I. Tanaka, First principles phonon calculations in materials science. *Scr. Mater.* 108, 1 (2015).
- [184] N. Marzari, A. A. Mostofi, J. R. Yates, I. Souza, and D. Vanderbilt, Maximally localized Wannier functions: theory and applications. *Rev. Mod. Phys.* 84, 1419 (2012).
- [185] Y. Gogotsi, and B. Anasori, The rise of MXenes. *ACS Nano* 13, 8491 (2019).

- [186] B. Anasori, M. R. Lukatskaya, and Y. Gogotsi, 2D metal carbides and nitrides (MXenes) for energy storage. *Nat. Rev. Mater.* 2, 16098 (2017).
- [187] B. Goodenough, Theory of the role of covalence in the Perovskite-type Manganites [La, $M(\text{II})$] MnO_3 . *Phys. Rev.* 100, 564 (1955).
- [188] J. Kanamori, Superexchange interaction and symmetry properties of electron orbitals. *J. Phys. Chem. Solids* 10, 87 (1959).
- [189] P. W. Anderson, New approach to the theory of superexchange interactions. *Phys. Rev.* 115, 2 (1959).
- [190] J. M. Kosterlitz, and D. J. Thouless, Ordering, metastability and phase transitions in two-dimensional systems. *J. Phys. C: Solid State Phys.* 6, 1181 (1973).
- [191] J. F. Fernández, M. F. Ferreira, and J. Stankiewicz, Critical behavior of the two-dimensional XY model: a Monte Carlo simulation. *Phys. Rev. B* 34, 292 (1986).
- [192] M. Ashton, D. Gluhovic, S. B. Sinnott, Jing Guo, D. A. Stewart, and R. G. Hennig, Two-dimensional intrinsic half-metals with large spin gaps. *Nano Lett.* 17, 5251 (2017).
- [193] S. Li, Q. Wang, C. Zhang, P. Guo, and S. A. Yang, Correlation-driven topological and valley states in monolayer VSi_2P_4 . *Phys. Rev. B* 104, 085149 (2021).
- [194] D. Dai, H. J. Xiang, and M.-H. Whangbo, Effects of spin-orbit coupling on magnetic properties of discrete and extended magnetic systems. *J. Comput. Chem.* 29, 2187 (2008).
- [195] R. Peng, Y. Ma, X. Xu, Z. He, B. Huang, and Y. Dai, Intrinsic anomalous valley Hall effect in single-layer Nb_3I_8 . *Phys. Rev. B* 102, 035412 (2020).
- [196] Q. Cui, J. Liang, B. Yang, Z. Wang, P. Li, P. Cui, and H. Yang, Giant enhancement of perpendicular magnetic anisotropy and induced quantum anomalous Hall effect in graphene/ NiI_2 heterostructures via tuning the van der Waals interlayer distance. *Phys. Rev. B* 101, 214439 (2020).
- [197] Q. Cui, J. Liang, Z. Shao, P. Cui, and H. Yang, Strain-tunable ferromagnetism and chiral spin textures in two-dimensional Janus chromium dichalcogenides. *Phys. Rev. B* 102, 094425 (2020).
- [198] X. Zhou, R.-W. Zhang, Z. Zhang et al., Sign-reversible valley-dependent Berry phase effects in 2D valley-half-semiconductors. *npj Comput. Mater.* 7, 160 (2021).
- [199] M. Slota, A. Keerthi, W. K. Myers et al., Magnetic edge states and coherent manipulation of graphene nanoribbons. *Nature* 557, 691–695 (2018).
- [200] W. Xing, L. Qiu, X. Wang, Y. Yao, Y. Ma, R. Cai, S. Jia, X. C. Xie, and W. Han, Magnon Transport in Quasi-Two-Dimensional van der Waals Antiferromagnets. *Phys. Rev. X* 9, 011026 (2019).
- [201] F. Katmis, V. Lauter, F. S. Nogueira et al., A high-temperature ferromagnetic topological insulating phase by proximity coupling. *Nature* 533, 513-516 (2016).
- [202] J.-X. Yu, and J. Zang, Giant perpendicular magnetic anisotropy in Fe/III-V nitride thin films. *Sci. Adv.* 4, eaar7814 (2018).

- [203] C. Xu, J. Feng, S. Prokhorenko, Y. Nahas, H. Xiang, and L. Bellaiche, Topological spin texture in Janus monolayers of the chromium trihalides Cr(I, X)₃. *Phys. Rev. B* 101, 060404 (2020).
- [204] J. Liang, W. Wang, H. Du, A. Hallal, K. Garcia, M. Chshiev, A. Fert, and H. Yang, Very large Dzyaloshinskii-Moriya interaction in two-dimensional Janus manganese dichalcogenides and its application to realize skyrmion states. *Phys. Rev. B* 101, 184401 (2020).
- [205] W. Legrand, D. Maccariello, F. Ajejas, S. Collin, A. Vecchiola, K. Bouzehouane, N. Reyren, V. Cros and A. Fert, Room-temperature stabilization of antiferromagnetic skyrmions in synthetic antiferromagnets. *Nat. Mater.* 19, 34-42 (2019).
- [206] R. Wiesendanger, Nanoscale magnetic skyrmions in metallic films and multilayers: a new twist for spintronics. *Nat. Rev. Mater.* 1, 16044 (2016).
- [207] N. Nagaosa, and Y. Tokura, Topological properties and dynamics of magnetic skyrmions. *Nat. Nanotechnol.* 8, 899-911 (2013).
- [208] J. Sampaio, V. Cros, S. Rohart, A. Thiaville, and A. Fert, Nucleation, stability and current-induced motion of isolated magnetic skyrmions in nanostructures. *Nat. Nanotechnol.* 8, 839 (2013).
- [209] S. Yang, R. Peng, T. Jiang, Y. Liu, L. Feng, J. Wang, L. Chen, X. Li, and C. Nan, Non-Volatile 180° Magnetization Reversal by an Electric Field in Multiferroic Heterostructures. *Adv. Mater.* 26, 7091 (2014).
- [210] H. S. Kum, H. Lee, S. Kim et al., Heterogeneous integration of single-crystalline complex-oxide membranes. *Nature* 578, 75-81 (2020).
- [211] L. Caretta, E. Rosenberg, F. Büttner et al., Electric-field-driven non-volatile multi-state switching of individual skyrmions in a multiferroic heterostructure. *Nat. Commun.* 11, 1 (2020).
- [212] R. O. Cherifi, V. Ivanovskaya, L. C. Phillips et al, Electric-field control of magnetic order above room temperature. *Nat. Mater.* 13, 345-351 (2013).
- [213] H. L. Zhuang, P. R. C. Kent, and R. G. Hennig, Strong anisotropy and magnetostriction in the two-dimensional Stoner ferromagnet Fe₃GeTe₂. *Phys. Rev. B* 93, 134407 (2016).
- [214] J. Son, K. Kim, Y. H. Ahn, H. Lee, and J. Lee, Strain Engineering of the Berry Curvature Dipole and Valley Magnetization in Monolayer MoS₂. *Phys. Rev. Lett.* 123, 036806 (2019).
- [215] D. C. Freitas, R. Weht, A. Sulpice, G. Remenyi, P. Strobel, F. Gay, J. Marcus, and M. N.-Regueiro, Ferromagnetism in layered metastable 1T-CrTe₂. *J. Phys.: Condens. Matter* 27, 176002 (2015).
- [216] X. Sun, W. Li, X. Wang et al., Room temperature ferromagnetism in ultra-thin van der Waals crystals of 1T-CrTe₂. *Nano Res.* 13, 3358–3363 (2020).
- [217] B. Yang, X. Zhang, H. Yang, X. Han, and Y. Yan, Strain controlling transport properties of heterostructure composed of monolayer CrI₃. *Appl. Phys. Lett.* 114, 192405 (2019).

- [218] X. Sui, T. Hu, J. Wang, B. Gu, W. Duan, and M. Miao, Voltage-Controllable Colossal Magnetocrystalline Anisotropy in Single Layer Transition Metal Dichalcogenides. *Phys. Rev. B* 96, 041410 (2017).
- [219] <https://github.com/ww1g11/JuMag.jl>
- [220] O. Boulle, J. Vogel, H. Yang et al., Room-temperature chiral magnetic skyrmions in ultrathin magnetic nanostructures. *Nat. Nanotechnol.* 11, 449 (2016).
- [221] B. Dupe, M. Hoffmann, C. Paillard, and S. Heinze, Tailoring magnetic skyrmions in ultra-thin transition metal films. *Nat. Commun.* 5, 4030 (2014).
- [222] H. Y. Lv, W. J. Lu, D. F. Shao, Y. Liu, and Y. P. Sun, Strain-controlled switch between ferromagnetism and antiferromagnetism in $1T\text{-CrX}_2$ ($X=\text{Se, Te}$) monolayers. *Phys. Rev. B* 92, 214419 (2015).
- [223] W. Jiang, X. Zhang, G. Yu, W. Zhang, X. Wang, M. B. Jungfleisch, J. E. Pearson, X. Cheng, O. Heinonen, K. L. Wang, and Y. Zhou, Direct observation of the skyrmion Hall effect. *Nat. Phys.* 13, 162-169 (2017).
- [224] J. Jena, B. Göbel, V. Kumar, I. Mertig, S. Felser, and S. Parkin, Evolution and competition between chiral spin textures in nanostripes with D_{2d} symmetry. *Sci. Adv.* 6, eabc0723 (2020).
- [225] X. Zhang, Y. Zhou, K. M. Song, T. E. Park, J. Xia, M. Ezawa, X. Liu, W. Zhao, G. Zhao, and S. Woo, Skyrmion-electronics: writing, deleting, reading and processing magnetic skyrmions toward spintronic applications. *J. Phys. Condens. Matter.* 32, 143001 (2020).
- [226] Y. Zhang, C. Xu, P. Chen, Y. Nahas, S. Prokhorenko, and L. Bellaiche, Emergence of skyrmionium in a two-dimensional $\text{CrGe}(\text{Se,Te})_3$ Janus monolayer. *Phys. Rev. B* 102, 241107 (2020).
- [227] J. Jiang, X. Liu, R. Li, and W. Mi, Topological spin textures in a two-dimensional $\text{MnBi}_2(\text{Se, Te})_4$ Janus material. *Appl. Phys. Lett.* 119, 072401 (2021).
- [228] N. Gao, S. G. Je, M. Y. Im et al., Creation and annihilation of topological meron pairs in in-plane magnetized films. *Nat. Commun.* 10, 1-9 (2019).
- [229] K. W. Moon, J. Yoon, C. Kim, and C. Hwang, Existence of in-plane magnetic skyrmion and its motion under current flow. *Phys. Rev. Appl.* 12, 064054 (2019).
- [230] B. Göbel, A. Mook, J. Henk, I. Mertig, and O. A. Tretiakov, Magnetic bimerons as skyrmion analogues in in-plane magnets. *Phys. Rev. B* 99, 060407 (2019).
- [231] L. Shen, J. Xia, X. Zhang, M. Ezawa, O. A. Tretiakov, X. Liu, G. Zhao, and Y. Zhou, Current-induced dynamics and chaos of antiferromagnetic bimerons. *Phys. Rev. Lett.* 124, 037202 (2020).
- [232] X. Li, L. Shen, Y. Bai et al., Bimeron clusters in chiral antiferromagnets. *npj Comput. Mater.* 6, 1-9 (2020).
- [233] F. Matsukura, Y. Tokura, and H. Ohno, Control of magnetism by electric fields. *Nat. Nanotechnol.* 10, 209-220 (2015).

- [234] P. J. Hsu, A. Kubetzka, A. Finco, N. Romming, K. von Bergmann, and R. Wiesendanger, Electric-field-driven switching of individual magnetic skyrmions. *Nat. Nanotechnol.* 12, 123-126 (2017).
- [235] M. Schott, A. Bernand-Mantel, L. Ranno, S. Pizzini, J. Vogel, H. Béa, C. Baraduc, S. Auffret, G. Gaudin, and D. Givord, The skyrmion switch: turning magnetic skyrmion bubbles on and off with an electric field. *Nano Lett.* 17, 3006-3012 (2017).
- [236] P. Huang, M. Cantoni, A. Kruchkov, J. Rajeswari, A. Magrez, F. Carbone, and H. M. Rønnow, In situ electric field skyrmion creation in magnetoelectric Cu_2OSeO_3 . *Nano Lett.* 18, 5167-5171 (2018).
- [237] C. Ma, X. Zhang, J. Xia, M. Ezawa, W. Jiang, T. Ono, S. N. Piramanayagam, A. Morisako, Y. Zhou, and X. Liu, Electric field-induced creation and directional motion of domain walls and skyrmion bubbles. *Nano Lett.* 19, 353-361 (2018).
- [238] J. Liang, Q. Cui, and H. Yang, Electrically switchable Rashba-type Dzyaloshinskii-Moriya interaction and skyrmion in two-dimensional magnetoelectric multiferroics. *Phys. Rev. B* 102, 220409 (2020).
- [239] C. Xu, P. Chen, H. Tan, Y. Yang, H. Xiang, and L. Bellaiche, Electric-field Switching of magnetic topological charge in type-I multiferroics. *Phys. Rev. Lett.* 125, 037203 (2020).
- [240] W. Sun, W. Wang, H. Li, G. Zhang, D. Chen, J. Wang, and Z. Cheng, Controlling bimerons as skyrmion analogues by ferroelectric polarization in 2D van der Waals multiferroic heterostructures. *Nat. Commun.* 11, 1-7 (2020).
- [241] L. Wang, Q. Feng, Y. Kim et al., Ferroelectrically tunable magnetic skyrmions in ultrathin oxide heterostructures. *Nat. Mater.* 17, 1087-1094 (2018).
- [242] J. Li, J. Y. Ni, X. Y. Li, H. -J. Koo, M. -H. Whangbo, J. S. Feng, and H. J. Xiang, Intralayer ferromagnetism between $S=5/2$ ions in MnBi_2Te_4 : Role of empty Bi p states. *Phys. Rev. B* 101, 201408 (2020).
- [243] Y. Li, Z. Jiang, J. Li, S. Xu, and W. Duan, Magnetic anisotropy of the two-dimensional ferromagnetic insulator MnBi_2Te_4 . *Phys. Rev. B.* 100, 134438 (2019).
- [244] P. E. Blöchl, Projector augmented-wave method, *Phys. Rev. B* 50, 17953 (1994).
- [245] W. Ding, J. Zhu, Z. Wang, Y. Gao, D. Xiao, Y. Gu, Z. Zhang and W. Zhu, Prediction of intrinsic two-dimensional ferroelectrics in In_2Se_3 and other $\text{III}_2\text{-VI}_3$ van der Waals materials. *Nat. Commun.* 8, 14956 (2017).
- [246] S. Nosé, A unified formulation of the constant temperature molecular dynamics methods. *J. Chem. Phys.* 81, 511-519 (1984).
- [247] G. H. O. Daalderop, P. J. Kelly, and M. F. H. Schuurmans, First-principles calculation of the magnetocrystalline anisotropy energy of iron, cobalt, and nickel. *Phys. Rev. B* 41, 11919 (1990).
- [248] A. Hallal, H. Yang, B. Dieny, and M. Chshiev, Anatomy of perpendicular magnetic anisotropy in Fe/MgO magnetic tunnel junctions: First-principles insight. *Phys. Rev. B* 88, 184423 (2013).

- [249] R. F. L. Evans, W. J. Fan, P. Chureemart, T. A. Ostler, M. O. A. Ellis and R. W. Chantrell, Atomistic spin model simulations of magnetic nanomaterials. *J. Phys.: Condens. Matter* 26, 103202 (2014).
- [250] Y. S. Hou, and R. Q. Wu, Strongly Enhanced Gilbert Damping in 3d Transition-Metal Ferromagnet Monolayers in Contact with the Topological Insulator Bi₂Se₃. *Phys. Rev. Appl.* 11, 054032 (2019).
- [251] J. Y. You, X. J. Dong, B. Gu, and G. Su, Electric field induced topological phase transition and large enhancements of spin-orbit coupling and Curie temperature in two-dimensional ferromagnetic semiconductors. *Phys. Rev. B* 103, 104403 (2021).
- [252] J. Li, Y. Li, S. Du, Z. Wang, B. L. Gu, S. C. Zhang, K. He, W. Duan, and Y. Xu, Intrinsic magnetic topological insulators in van der Waals layered MnBi₂Te₄-family materials. *Sci. Adv.* 5, eaaw5685 (2019).
- [253] M. M. Otrokov, I. P. Rusinov, M. Blanco-Rey et al., Unique thickness-dependent properties of the van der Waals interlayer antiferromagnet MnBi₂Te₄ films, *Phys. Rev. Lett.* 122, 107202 (2019).
- [254] S. Yuan, W. F. Io, J. Mao, Y. Chen, X. Luo, and J. Hao, Enhanced Piezoelectric Response of Layered In₂Se₃/MoS₂ Nanosheet-Based van der Waals Heterostructures. *ACS Appl. Nano Mater.* 3, 11979-11986 (2020).
- [255] H. Yang, M. Xiao, Y. Cui, L. Pan, K. Zhao, and Z. Wei, Nonvolatile memristor based on heterostructure of 2D room-temperature ferroelectric α -In₂Se₃ and WSe₂. *Sci. China Inf. Sci.* 62, 220404 (2019).
- [256] AY. Lu, H. Zhu, J. Xiao et al, Janus monolayers of transition metal dichalcogenides. *Nat. Nanotechnol.* 12, 744–749 (2017).
- [257] R. Sant, M. Gay, A. Marty et al, Synthesis of epitaxial monolayer Janus SPtSe. *NPJ 2D Mater. Appl.* 4, 41 (2020).
- [258] Y. Zhou, D. Wu, Y. Zhu, Y. Cho, Q. He, X. Yang, K. Herrera, Z. Chu, Y. Han, M. C. Downer, H. Peng, and K. Lai, Out-of-plane piezoelectricity and ferroelectricity in layered α -In₂Se₃ nanoflakes. *Nano. Lett.* 17, 5508-5513 (2017).
- [259] The optimized in-plane lattice constants of MBST and In₂Se₃ monolayers are 4.233 and 4.108 Å, respectively. Here, 1×1 In₂Se₃ monolayer is strained by 3.04% to match 1×1 MBST monolayer.
- [260] J. Xiao, H. Zhu, Y. Wang, W. Feng, Y. Hu, A. Dasgupta, Y. Han, Y. Wang, D. A. Muller, L. W. Martin, P. Hu, and X. Zhang, Intrinsic Two-Dimensional Ferroelectricity with Dipole Locking. *Phys. Rev. Lett.* 120, 227601 (2020).
- [261] S. Z. Lin, A. Saxena, and C. D. Batista, Skyrmion fractionalization and merons in chiral magnets with easy-plane anisotropy. *Phys. Rev. B* 91, 224407 (2015).
- [262] S. Rohart and A. Thiaville, Skyrmion confinement in ultrathin film nanostructures in the presence of Dzyaloshinskii-Moriya interaction. *Phys. Rev. B* 88, 184422 (2013).
- [263] A. O. Leonov, T. I. Monchesky, N. Romming, A. Kubetzka, A. N. Boganov, and R. Wiesendanger, The properties of isolated chiral skyrmions in thin magnetic films. *New J. Phys.* 18, 065003 (2016).

- [264] H. Jia, B. Zimmermann, and S. Blügel, First-principles investigation of chiral magnetic properties in multilayers: Rh/Co/Pt and Pd/Co/Pt. *Phys. Rev. B* 98, 144427 (2018).
- [265] F. Xue, Z. Wang, Y. Hou, L. Gu, and R. Wu, Control of magnetic properties of MnBi_2Te_4 using a van der Waals ferroelectric III2-VI3 film and biaxial strain. *Phys. Rev. B* 101, 184426 (2020).
- [266] W. Luo, K. Xu, and H. Xiang, Two-dimensional hyperferroelectric metals: A different route to ferromagnetic-ferroelectric multiferroics. *Phys. Rev. B* 96, 235415 (2017).
- [267] H. Xiang, Origin of polar distortion in LiNbO_3 -type “ferroelectric” metals: Role of A-site instability and short-range interactions. *Phys. Rev. B* 90, 094108 (2014).
- [268] A. Filippetti, V. Fiorentini, F. Ricci et al., Prediction of a native ferroelectric metal. *Nat Commun* 7, 11211 (2016).
- [269] A. K. N., V. Kumar, T. Ma, P. Werner, E. Pippel, R. Sahoo, F. Damay, U. K. Röbler, C. Felser, S. S. P. Parkin, Magnetic antiskyrmions above room temperature in tetragonal Heusler materials. *Nature* 548, 561–566 (2017).
- [270] S. Huang, C. Zhou, G. Chen, H. Shen, A. K. Schmid, K. Liu, and Y. Wu, Stabilization and current-induced motion of antiskyrmion in the presence of anisotropic Dzyaloshinskii-Moriya interaction. *Phys. Rev. B* 96, 144412 (2017).
- [271] W. Koshibae and N. Nagaosa, Theory of antiskyrmions in magnets. *Nat. Commun.* 7, 10542 (2016).
- [272] M. Hoffmann, B. Zimmermann, G. P. Müller, D. Schürhoff, N. S. Kiselev, C. Melcher, and S. Blügel, Antiskyrmions stabilized at interfaces by anisotropic Dzyaloshinskii-Moriya interactions. *Nat. Commun.* 8, 308 (2017).
- [273] L. Peng, R. Takagi, W. Koshibae, K. Shibata, K. Nakajima, T. Arima, N. Nagaosa, S. Seki, X. Yu, and Y. Tokura, Controlled transformation of skyrmions and antiskyrmions in a non-centrosymmetric magnet. *Nat. Nanotechnol.* 15, 181–186 (2020).
- [274] K. Karube, L. Peng, J. Masell, X. Yu, F. Kawaga, Y. Tokura, and Y. Taguchi, Room-temperature antiskyrmions and sawtooth surface textures in a non-centrosymmetric magnet with S_4 symmetry. *Nat. Mater.* 20, 335–340 (2021).
- [275] X. Zhang, Y. Zhou and M. Ezawa, Antiferromagnetic Skyrmion: Stability, Creation and Manipulation. *Sci. Rep.* 6, 24795 (2016).
- [276] J. Barker and O. A. Tretiakov, Static and Dynamical Properties of Antiferromagnetic Skyrmions in the Presence of Applied Current and Temperature. *Phys. Rev. Lett.* 116, 147203 (2016).
- [277] H. Jani, J. C. Lin, J. Chen, J. Harrison, F. Maccherozzi, J. Schad, S. Prakash, C. B. Eom, A. Ariando, T. Venkatesan, and P. G. Radaelli, Antiferromagnetic half-skyrmions and bimerons at room temperature. *Nature* 590, 74–79 (2021).
- [278] J. Spethmann, M. Grünebohm, R. Wiesendanger, K. von Bergmann, and A. Kubetzka, Discovery and characterization of a new type of domain wall in a row-wise antiferromagnet. *Nat. Commun.* 12, 3488 (2021).
- [279] L. M. Sandratskii, Insight into the Dzyaloshinskii-Moriya interaction

- through first-principles study of chiral magnetic structures. *Phys. Rev. B* 96, 024450 (2017).
- [280] S. Haastrup, M. Strange, M. Pandey, T. Deilmann, P. S Schmidt, N. F Hinsche, M. N Gjerding, D. Torelli, P. M Larsen, A. C Riis-Jensen, J. Gath, K. W Jacobsen, J. J. Mortensen, T. Olsen, and K. S Thygesen, The Computational 2D Materials Database: High-Throughput Modeling and Discovery of Atomically Thin Crystals. *2D Mater.* 5, 042002 (2018).
- [281] M. N. Gjerding, A. Taghizadeh, A. Rasmussen, S. Ali, F. Bertoldo, T. Deilmann, U. P. Holguin, N. R. Knøsgaard, M. Kruse, S. Manti, T. G. Pedersen, T. Skovhus, M. K. Svendsen, J. J. Mortensen, T. Olsen, and K. S. Thygesen, Recent Progress of the Computational 2D Materials Database (C2DB). *2D Mater.* 8, 044002 (2021).
- [282] C. Huang, J. Feng, J. Zhou, H. Xiang, K. Deng, and E. Kan, Ultra-High-Temperature Ferromagnetism in Intrinsic Tetrahedral Semiconductors. *J. Am. Chem. Soc.* 141, 12413-1241 (2019).
- [283] V. H. Etgens, P. C. de Camargo, M. Eddrief, R. Mattana, J. M. George, and Y. Garreau, Structure of Ferromagnetic CrAs Epilayers Grown on GaAs(001). *Phys. Rev. Lett.* 92, 167205 (2004).
- [284] V. F. Agekyan, P. O. Holz, G. Karczewski, V. N. Katz, E. S. Moskalenko, A. Yu. Serov, and N. G. Filosofov, Magnetoluminescence of CdTe/MnTe/CdMgTe heterostructures with ultrathin MnTe layers. *Semiconductors* 45, 1301 (2011).

Publication List

1. Giant enhancement of perpendicular magnetic anisotropy and induced quantum anomalous Hall effect in graphene/NiI₂ heterostructures via tuning the van der Waals interlayer distance.
Q. Cui, J. Liang, B. Yang, Z. Wang, P. Li, P. Cui, and H. Yang.
Phys. Rev. B 101, 214439 (2020). (Chapter 3)
2. Spin-valley coupling in a two-dimensional VSi₂N₄ monolayer
Q. Cui, Y. Zhu, J. Liang, P. Cui, and H. Yang.
Phys. Rev. B 103, 085421 (2021). (Chapter 4)
3. Strain-tunable ferromagnetism and chiral spin textures in two-dimensional Janus chromium dichalcogenides.
Q. Cui, J. Liang, Z. Shao, P. Cui, and H. Yang.
Phys. Rev. B 102, 094425 (2020). (Chapter 5)
4. Ferroelectrically controlled topological magnetic phase in a Janus-magnet-based multiferroic heterostructure.
Q. Cui, Y. Zhu, J. Jiang, J. Liang, D. Yu, P. Cui, and H. Yang.
Phys. Rev. Research 3, 043011 (2021). (Chapter 6)
5. Anisotropic Dzyaloshinskii–Moriya Interaction and Topological Magnetism in Two-Dimensional Magnets Protected by P $\bar{4}m2$ Crystal Symmetry.
Q. Cui, Y. Zhu, Y. Ga, J. Liang, P. Li, D. Yu, P. Cui, and H. Yang.
Nano Lett. 22, 2334-2341 (2022). (Chapter 7)
6. Robust and High Photoluminescence in WS₂ Monolayer through In Situ Defect Engineering.
Q. Cui[#], Z. Luo[#], Q. Cui[#], W. Zhu, H. Shou, C. Wu, Z. Liu, Y. Lin, P. Zhang, S. Wei, H. Yang, S. Chen, A. Pan, and L. Song.
Adv. Funct. Mater. 2105339 (2021).
7. Controllable Generation of Antiferromagnetic Skyrmions in Synthetic Antiferromagnets with Thermal Effect.
R. Chen[#], Q. Cui[#], L. Han, X. Xue, J. Liang, H. Bai, Y. Zhou, F. Pan, H. Yang, and C. Song. **Adv. Funct. Mater.** 2111906 (2022).
8. Electrically switchable Rashba-type Dzyaloshinskii-Moriya interaction and skyrmion in two-dimensional magnetoelectric multiferroics.
J. Liang, Q. Cui, and H. Yang.
Phys. Rev. B 102, 220409(R) (2020).
9. Reversible control of Dzyaloshinskii-Moriya interaction at the graphene/Co interface via hydrogen absorption.
B. Yang, Q. Cui, J. Liang, M. Chshiev, and H. Yang.
Phys. Rev. B 101, 014406 (2020).
10. Magnetic Exchange Field Modulation of Quantum Hall Ferromagnetism in 2D van der Waals CrCl₃/Graphene Heterostructures.
Y. Wu, Q. Cui, M. Zhu, X. Liu, Y. Wang, J. Zhang, X. Zheng, J. Shen, P. Cui, H. Yang, and S. Wang.

- ACS Appl. Mater. Inter.** 13, 10656 (2021).
11. Reducing Dzyaloshinskii-Moriya interaction and field-free spin-orbit torque switching in synthetic antiferromagnets.
R. Chen, Q. Cui, L. Liao, Y. Zhu, R. Zhang, H. Bai, Y. Zhou, G. Xing, F. Pan, H. Yang, and C. Song.
Nat. Commun. 12, 3113 (2021).
 12. Electrically Controllable Van Der Waals Antiferromagnetic Spin Valve.
X. Zhai, Z. Xu, Q. Cui, Y. Zhu, H. Yang, and Y.M. Blanter.
Phys. Rev. Appl. 16, 014032 (2021).